

National Technical University of Ukraine  
“Igor Sikorsky Kyiv Polytechnic Institute”  
Ministry of Education and Science of Ukraine

National Technical University of Ukraine  
“Igor Sikorsky Kyiv Polytechnic Institute”  
Ministry of Education and Science of Ukraine

Qualifying scientific  
work as a manuscript

**LI CHE**

UDC: 544.722.132

**THESIS**

**Organo-mineral textured coatings with enhanced water repellency**

161 Chemical Technologies and Engineering

16 Chemical and Bioengineering

Submitted for the attainment of the Doctor of Philosophy degree

The dissertation contains the results of personal research. The use of ideas, results, and texts from other authors are accompanied by references to the respective sources.

Li Che Li Che

Scientific Supervisor: Oleksiy Myronyuk, Dr. Tech. Sc., As. Professor.

Kyiv - 2025

## ABSTRACT

*Li Che.* Organo-mineral textured coatings with enhanced water repellency. - Qualified scientific work on the rights of the manuscript.

Dissertation for the degree of Doctor of Philosophy in the specialty 161 - Chemical Technologies and Engineering and Knowledge branch 16 – Chemical Engineering and bioengineering - National Technical University of Ukraine "Igor Sikorsky Kyiv Polytechnic Institute", Kyiv, 2025.

This study is aimed at establishing the possibility of using scalable organo-mineral surfaces to achieve tunable water wettability. To this end, systems comprising a mineral filler with particles of controlled shape and a polymer binder, as well as a thin organic layer with an extractive texture on the surface, are considered. The study demonstrates the relationship between the size, shape, and hierarchy of the texture-forming elements and the surfaces' water-repellent properties, as well as their durability under ultraviolet radiation exposure.

This study also contributes to addressing the major challenge of scaling up superhydrophobic surfaces. Since the systems investigated here are based on polymer binders combined with dispersed mineral fillers, this approach can be readily scaled to produce such coatings over large areas using existing manufacturing technologies.

The purpose of this study is to establish the connection between the structure and water repellency of organo-mineral surfaces.

The object of research is textured surfaces with tuned water repellency on the base of organic interface layer and mineral texture forming elements.

The subject of research is the formation of water repellency of textures consisting of mineral structure formers and organic binding and interface layers.

It has been shown that in organo-mineral systems based on dispersed particles - using red mud as an example - the water-repellent properties are governed by a combination of key factors: the ability of the particles to form a textured coating

surface, which in turn depends on the ratio between the particles and the polymer matrix; the surface inertness of the filler particles, with higher inertness leading to more stable water-repellent surfaces; and the particle size, as smaller particles contribute to higher contact angles and thus improved water-repellent performance.

Using an integrated approach based on hydrothermal synthesis, Zn-O-based particles with tunable morphology were obtained. By adjusting parameters such as temperature, catalyst type, reaction medium acidity, and the presence of doping agents (e.g., titanium dioxide and silicon dioxide), it is possible to control the particle size within a range of several tens to hundreds of nanometers, introduce hierarchical surface structures, and tailor the shape of the primary crystals, including plate-like, elongated, or irregular particles with complex architectures.

It has been shown that the use of hierarchical zinc oxide-based particles, particularly those doped with titanium dioxide, leads to a significant enhancement in water-repellent performance compared to undoped or structurally simple particles. The observed increase in contact angle is approximately  $20^\circ$ , enabling the creation of truly superhydrophobic surfaces based on these hierarchical structures.

It has also been demonstrated that superhydrophobic surfaces can be achieved over a broader range of nanoparticle concentrations (20-60 wt. %) when the particles possess a hierarchical surface structure. Unlike those lacking a distinct dual-level hierarchy, such particles enable stable water repellency even as the filler concentration varies.

The studied materials with high specific surface area have shown strong potential for use in atmospheric water harvesting from fog. It was found that hydrophobic surfaces enable condensation of up to 7 grams of water per minute. In contrast, hydrophilic surfaces—achieved either by using unmodified mineral particles or by annealing—can collect up to 8.5 grams of atmospheric moisture per minute.

The scientific novelty of the study is as follows: For the first time, it has been demonstrated - using red mud as an example - that surface inactivation of its particles,

achieved by reducing their polarity through thermal treatment at 950 °C and modification with organosilicon compounds, enables the effective use of such waste as texture-forming components in the production of coatings with pronounced water-repellent properties. In particular, contact angles of approximately 143° were achieved on the treated surfaces.

This study advances the theoretical understanding of the formation of water-repellent surfaces composed of dispersed micro- and nanoparticles embedded in organic polymer matrices. It was shown that particle surface topography and their chemical inertness play a critical role in generating effective surface texture. Additionally, fine-tuning the ratio between the polymer and the film-forming agent allows precise control over the coating structure, enabling the achievement of maximum contact angles. In this work, contact angles as high as 154° were obtained. This study further develops the understanding of the synthesis of zinc oxide (ZnO)-based particles with tunable morphology. It has been demonstrated that the particle shape is governed by a combination of factors, including the type of catalyst used, the synthesis temperature, the presence of dopants such as TiO<sub>2</sub> and SiO<sub>2</sub>, and the ZnO-to-dopant ratio. By adjusting these parameters, it is possible to control the particle morphology, ranging from plate-like structures typical of pure ZnO to complex hierarchical architectures characteristic of doped forms.

It has been shown that doped forms of zinc oxide (ZnO) crystals exhibit pronounced photoactivity. This effect is significantly enhanced when titanium dioxide (TiO<sub>2</sub>) is used as a dopant. Specifically, photoluminescence analysis revealed that at a ZnO:TiO<sub>2</sub> ratio of 2:1, the photoactivity increases by approximately 6.5 times compared to undoped ZnO.

For the first time, it has been demonstrated that the use of titanium-dioxide-doped zinc oxide particles with a highly developed surface structure leads to a significant enhancement in water-repellent properties compared to conventional nanoscale ZnO particles. At high filler loadings, the contact angle increases from 135° to 154°, classifying such coatings as superhydrophobic.

It has been demonstrated for the first time that the developed hierarchical micro/nanostructure of doped zinc oxide particles enables the formation of highly water-repellent surfaces across a broad range of mass ratios between the polymer matrix and the mineral texture-forming particles. Specifically, when the content of doped ZnO/CO<sub>2</sub> particles ranges from 20% to 60%, contact angles remain above 140°. In contrast, the use of individual TiO<sub>2</sub>, CO<sub>2</sub>, or ZnO particles results in such high water-repellent performance only within much narrower concentration ranges.

It has been shown that coatings containing texturing elements based on modified ZnO particles doped with TiO<sub>2</sub> and SiO<sub>2</sub> exhibit high resistance to UV-induced hydrophilization. These coatings transition from the Cassie–Baxter state to the Wenzel state only after 170 hours of UV exposure, while maintaining a contact angle of approximately 120°. Complete hydrophilization occurs only after 250–280 hours of continuous irradiation.

It has been shown that textured surfaces, particularly those with hierarchical micro/nanostructures, are effective for fog water collection. The efficiency of water harvesting significantly increases upon hydrophilization of the surface, with an observed improvement of approximately 30–45% compared to hydrophobic surfaces.

The practical significance of the obtained results is as follows: In the course of this work, a novel synthesis method was developed for doped hierarchical ZnO–SiO<sub>2</sub> and ZnO–TiO<sub>2</sub> particles. These materials can serve as a basis for water-repellent textured coatings and are also considered promising hydrophilic materials for atmospheric moisture harvesting. Additionally, both types of particles exhibit pronounced photoactive properties, expanding their potential for use in multifunctional surface applications. The developed organo-mineral coating formulations based on composite hierarchical ZnO particles doped with titanium dioxide and silicon dioxide exhibit stability under ultraviolet irradiation for over 170 hours. These coatings retain their hydrophobic properties under prolonged UV exposure, making them promising candidates for use as UV-resistant water-repellent surfaces.

**Keywords:** *red mud, nanoparticles, composite, titanium dioxide, polymer, silica, modification, styrene acrylate, hydrothermal treatment, zinc oxide*

*The list of applicants publication as follows:*

*Scientific papers:*

1. Wang, M.; Li, C.; Liu, B.; Qin, W.; Xie, Y. Influence of calcination temperature on photocatalyst performances of floral Bi<sub>2</sub>O<sub>3</sub>/TiO<sub>2</sub> composite. Catalysts 2022, 12 (12), 1635. 10.3390/catal12121635. ISSN 2073-4344 Scopus indexed journal. *Contributions of the author: analysis of literature, experiments performing, data processing, paper drafting.*
2. Wang, M.; Li, C.; Liu, B.; Qin, W.; Xie, Y. Facile synthesis of Nano-Flower Bi<sub>2</sub>O<sub>3</sub>/TiO<sub>2</sub> heterojunction as photocatalyst for degradation RHB. Molecules 2023, 28 (2), 882. 10.3390/molecules28020882. ISSN 1420-3049 Scopus indexed journal. *Contributions of the author: analysis of literature, experiments performing, data processing, paper drafting.*
3. Myronyuk, O.; **Li, C.** Use of textured surfaces for condensation of water vapour and mist. Water And Water Purification Technologies Scientific And Technical News 2024, 37 (3), 50–56. 10.20535/2218-930032023301987. ISSN 2521-151X The journal is in the list of scientific speciality journals of Ukraine. *Contributions of the author: analysis of literature, experiments performing, data processing, paper drafting.*
4. Миронюк, О. В.; Баклан, Д. В.; **Лі, Ч.** Водовідштовхувальні тонкоплівкові полімерні композити з частинками червоного шламу як структуроутворювачами. Technologies and Engineering 2023, No. 3, 56–66. 10.30857/2786-5371.2023.3.6. ISSN 2786-5371, 2786-538X The journal is in the list of scientific speciality journals of Ukraine. *Contributions of the author: experiments performing, data processing, paper drafting, submission.*
5. **Li, C.**; Myronyuk, O.; Bilousova, A. Establishing the type of texture forming particles on hydrophobic properties of coatings. Herald of Khmelnytskyi National

University Technical Sciences 2024, 333 (2), 155–161. 10.31891/2307-5732-2024-333-2-25. **ISSN** 2307-5732 The journal is in the list of scientific speciality journals of Ukraine. *Contributions of the author: literature analysis, experiments performing, paper drafting, submission.*

6. **Li, C.**; Myronyuk, O.; Bilousova, A.; Pitak, Y. Synthesis and characterization of Zn-based ceramic particles with controlled morphology. Scientific Research on Refractories and Technical Ceramics 2024, No. 124, 104–110. 10.35857/2663-3566.124.11. **ISSN** 2663-3566 The journal is in the list of scientific speciality journals of Ukraine. *Contributions of the author: literature analysis, experiments performing, paper drafting.*

*Conference proceedings:*

7. Myronyuk, Oleksiy, **Li Che**, Bilousova, Anna, Pitak, Yaroslav (2024) Zinc Oxide Based Particles With Hierarchical Structure For Surface Wetting Modification 2024 IEEE 5th KhPI Week on Advanced Technology, KhPIWeek 2024, 351-354, Ukraine, [https://doi.org/ 10.1109/KHPIWEEK61434.2024.10878067](https://doi.org/10.1109/KHPIWEEK61434.2024.10878067) *Contributions of the author: literature analysis, experiments performing, paper drafting.*

8. O. Myronyuk, D. Baklan, **C. Li** (2023) Thin film polymer composites incorporating red mud particles as agents for forming textured surfaces with water repellent properties XII international scientific-practical web-conference “Composition Materials” 64-67, Ukraine, <https://ela.kpi.ua/handle/123456789/62024> *Contributions of the author: literature analysis, experiments performing, data analysis and processing*

9. Bilousova A., **Li Che**. (2024) Study of the influence of nanoparticles on the hydrophobic properties of coatings XIII international scientific-practical web-conference “Composition Materials” 57-64, Ukraine, [10.20535/iwccmm2024](https://doi.org/10.20535/iwccmm2024) *Contributions of the author: literature analysis, experiments performing, paper drafting.*

## АНОТАЦІЯ

**Лі Че.** Органо-мінеральні текстуровані покриття з підвищеним водовідштовхуванням. – Кваліфікаційна наукова праця на правах рукопису.

Дисертація на здобуття наукового ступеня доктора філософії за спеціальністю 161 – Хімічні технології та інженерія, галузь знань 16 – Хімічна та біоінженерія – Національний технічний університет України «Київський політехнічний інститут імені Ігоря Сікорського», Київ, 2025.

Дослідження спрямоване на встановлення можливості використання масштабованих органо-мінеральних поверхонь для досягнення керованої змочуваності водою. З цією метою розглянуто системи, що складаються з мінерального наповнювача з частинками контрольованої форми та полімерного зв'язуючого, а також тонкого органічного шару з екстрактивною текстурою на поверхні. Показано взаємозв'язок між розміром, формою та ієрархією елементів текстури та водовідштовхувальними властивостями поверхонь, а також їхньою стійкістю до впливу ультрафіолетового випромінювання.

Дослідження робить внесок у вирішення актуальної проблеми масштабування супергідорфобних поверхонь. Оскільки досліджувані системи базуються на полімерних зв'язуючих у комбінації з дисперсними мінеральними наповнювачами, такий підхід легко масштабувати для отримання подібних покриттів на великих площах із використанням існуючих виробничих технологій.

Мета роботи – встановити взаємозв'язок між структурою та водовідштовхувальними властивостями органо-мінеральних поверхонь.

Об'єкт дослідження – текстуровані поверхні з регульованою змочуваністю, створені на основі органічного інтерфейсного шару та мінеральних елементів, що формують текстуру.

Предмет дослідження – формування водовідштовхувальних властивостей текстур, що складаються з мінеральних структуроутворювачів і органічних зв'язуючих та інтерфейсних шарів.

Показано, що в орґано-мінеральних системах на основі дисперсних частинок – на прикладі червоного шламу – водовідштовхувальні властивості визначаються сукупністю ключових факторів: здатністю частинок формувати текстуровану поверхню покриття (що, своєю чергою, залежить від співвідношення частинок і полімерної матриці), хімічною інертністю поверхні наповнювача (вища інертність забезпечує більш стабільні гідрофобні властивості) та розміром частинок (менший розмір сприяє збільшенню кутів змочування і, відповідно, покращенню водовідштовхування).

З використанням комплексного підходу на основі гідротермального синтезу отримано частинки на основі Zn–O із керованою морфологією. Регулювання таких параметрів, як температура, тип каталізатора, кислотність реакційного середовища та наявність легувальних домішок ( $\text{TiO}_2$ ,  $\text{SiO}_2$ ), дозволяє змінювати розміри частинок у діапазоні від кількох десятків до сотень нанометрів, формувати ієрархічні структури поверхні та контролювати форму первинних кристалів (пластинчасту, видовжену чи нерегулярну зі складною архітектурою).

Показано, що використання ієрархічних частинок на основі оксиду цинку, зокрема легованих  $\text{TiO}_2$ , призводить до суттєвого покращення водовідштовхувальних властивостей порівняно з нелегованими або структурно простими частинками. Збільшення кута змочування становить близько  $20^\circ$ , що дає змогу формувати справжні супергідрофобні поверхні на основі таких ієрархічних структур.

Також продемонстровано, що супергідрофобні поверхні можуть бути отримані в ширшому діапазоні концентрацій наночастинок (20–60 % мас.), якщо вони мають ієрархічну поверхневу структуру. На відміну від частинок без вираженої дворівневої ієрархії, такі наповнювачі забезпечують стабільне водовідштовхування навіть за зміни концентрації.

Досліджувані матеріали з великою питомою поверхнею показали високий потенціал для використання в системах атмосферного збору води з туману. Встановлено, що гідрофобні поверхні забезпечують конденсацію до 7 г води за хвилину, тоді як гідрофільні (отримані шляхом використання немодифікованих мінеральних частинок або відпалу) – до 8,5 г/хв.

Наукова новизна полягає в тому, що вперше – на прикладі червоного шламу – показано: дезактивація поверхні його частинок, досягнута шляхом зниження їх полярності термічною обробкою при 950 °C і модифікацією органосилікатними сполуками, дає змогу ефективно використовувати такі відходи як елементи текстури при створенні покриттів із вираженими водовідштовхувальними властивостями. Зокрема, на оброблених поверхнях досягнуто кутів змочування близько 143°.

Робота розвиває теоретичні уявлення про формування гідрофобних поверхонь, що складаються з дисперсних мікро- та наночастинок, вбудованих в органічну полімерну матрицю. Показано, що топографія поверхні частинок та їх хімічна інертність відіграють ключову роль у створенні ефективної поверхневої текстури. Крім того, тонке налаштування співвідношення полімер/плівкоутворювач дозволяє точно контролювати структуру покриття та досягати максимальних кутів змочування. У цій роботі отримано значення до 154°.

Розвинуто уявлення про синтез частинок ZnO з керованою морфологією. Встановлено, що форма частинок визначається поєднанням факторів, серед яких тип каталізатора, температура синтезу, наявність домішок TiO<sub>2</sub> та SiO<sub>2</sub> і співвідношення ZnO/домішка. Керування цими параметрами дозволяє змінювати морфологію – від пластинчастих структур, характерних для чистого ZnO, до складних ієрархічних архітектур, притаманних легованим формам.

Показано, що леговані форми кристалів ZnO характеризуються вираженою фотоактивністю, яка значно зростає при легуванні TiO<sub>2</sub>. Зокрема, фотолюмінесцентний аналіз показав, що при співвідношенні ZnO:TiO<sub>2</sub> = 2:1 фотоактивність збільшується приблизно у 6,5 раза порівняно з нелегованим ZnO.

Вперше доведено, що використання частинок ZnO з розвиненою поверхневою структурою, легованих TiO<sub>2</sub>, забезпечує значне підвищення гідрофобних властивостей порівняно зі звичайними наночастинками ZnO. При високих концентраціях наповнювача кут змочування збільшується з 135° до 154°, що відповідає класу супергідорфобних покриттів.

Вперше показано, що ієрархічна мікро-/наноструктура легованих частинок ZnO забезпечує формування високогідрофобних поверхонь у широкому діапазоні співвідношень полімерної матриці до мінеральних елементів. При вмісті легованих ZnO/CO<sub>2</sub> частинок у межах 20–60 % кути змочування залишаються понад 140°. Для окремих частинок TiO<sub>2</sub>, CO<sub>2</sub> чи ZnO такі властивості досягаються лише у вузькому діапазоні концентрацій.

Показано, що покриття з текстуроутворювальними елементами на основі модифікованих частинок ZnO, легованих TiO<sub>2</sub> та SiO<sub>2</sub>, мають високу стійкість до УФ-індукованої гідрофілізації. Перехід із стану Кассі–Бакстера в стан Венцеля відбувається лише після 170 год опромінення, при збереженні кута змочування близько 120°. Повна гідрофілізація спостерігається лише після 250–280 год безперервного УФ-випромінювання.

Доведено, що текстуровані поверхні, особливо з ієрархічною мікро-/наноструктурою, ефективні для збору води з туману. Ефективність збору суттєво зростає після гідрофілізації поверхні – на 30–45 % у порівнянні з гідрофобними.

Практичне значення отриманих результатів полягає в тому, що в ході роботи розроблено новий метод синтезу легованих ієрархічних частинок ZnO–SiO<sub>2</sub> та ZnO–TiO<sub>2</sub>. Ці матеріали можуть слугувати основою як для створення водовідштовхувальних текстурованих покриттів, так і перспективними гідрофільними матеріалами для збору атмосферної вологи. Обидва типи частинок виявляють виражену фотоактивність, що розширює їхній потенціал у багатофункціональних покриттях. Розроблені органо-мінеральні покриття на основі композитних ієрархічних частинок ZnO, легованих TiO<sub>2</sub> та SiO<sub>2</sub>, зберігають гідрофобні властивості протягом понад 170 год УФ-опромінення, що

робить їх перспективними для використання як УФ-стійкі водовідштовхувальні поверхні.

**Ключові слова:** червоний шлам, наночастинки, композит, діоксид титану, полімер, діоксид кремнію, модифікування, стирол-акрилат, гідротермальна обробка, оксид цинку

## CONTENTS

|   |            |
|---|------------|
| <b>LIST OF ABBREVIATIONS.....</b>   | <b>15</b>  |
| <b>INTRODUCTION .....</b>   | <b>16</b>  |
| <b>CHAPTER 1. Formation of water repellent properties of composite coatings with mineral fillers and polymer matrix .....</b> | <b>22</b>  |
| 1.1. Research and application of superhydrophobic materials .....   | 22         |
| 1.2. Fundamentals of surface wetting .....  | 23         |
| 1.3. Methods of superhydrophobic surfaces obtaining .....   | 29         |
| 1.4. Use of ZnO as the texture forming element of superhydrophobic coatings.....  | 33         |
| <b>CHAPTER 2. Materials and methods .....</b>   | <b>45</b>  |
| 2.1 Reagents and materials .....  | 45         |
| 2.2 Preparation of ZnO and its composites via precipitation method.....   | 50         |
| 2.3. Preparation of organo-mineral coatings .....   | 53         |
| 2.4. Instrumental methods of characterization .....   | 54         |
| <b>CHAPTER 3. Water repellent coatings on the basis of red mud .....</b>  | <b>62</b>  |
| Conclusions to Chapter 3 .....  | 71         |
| <b>CHAPTER 4. Obtaining of ZnO based particles with controlled morphology ..</b>  | <b>73</b>  |
| 4.1. Particle morphology control by synthesis environment tuning .....  | 73         |
| 4.2. ZnO particles morphology control via doping .....  | 82         |
| 4.3. Tuning of ZnO-TiO <sub>2</sub> composite particles morphology via oxides ratio .....                                     | 102        |
| Conclusions to chapter 4 .....  | 110        |
| <b>CHAPTER 5. ORGANO-MINERAL COATINGS OBTAINING AND CHARACTERIZATION .....</b>  | <b>111</b> |
| 5.1. Dependence of wetting properties of textured coatings on the filler particles content and type.....                      | 112        |

|   |            |
|---|------------|
| 5.2 Wetting transition of particulate filled textured coatings..... | 131        |
| Conclusions to Chapter 5 .....                                      | 135        |
| <b>CHAPTER 6. Thin organic coatings on mineral surfaces .....</b>   | <b>138</b> |
| Conclusions to Chapter 6 .....                                      | 147        |
| <b>CONCLUSIONS.....</b>   | <b>149</b> |
| <b>References list .....</b>  | <b>151</b> |

## **LIST OF ABBREVIATIONS**

ATR – Attenuated Total Reflection  
CA – Contact Angle  
CB – Cassie–Baxter  
CVD – Chemical Vapor Deposition  
DI – Deionized Water  
EDS – Energy Dispersive X-ray Spectroscopy  
FESEM – Field Emission Scanning Electron Microscopy  
FTIR – Fourier Transform Infrared Spectroscopy  
HRTEM – High-Resolution Transmission Electron Microscopy  
IPA – Isopropyl Alcohol  
IR – Infrared  
JCPDS – Joint Committee on Powder Diffraction Standards  
LIPSS – Laser-Induced Periodic Surface Structures  
MTES – Methyltriethoxysilane  
OCTEO – Octyltriethoxysilane  
PL – Photoluminescence  
PTFE – Polytetrafluorethylene  
SEM – Scanning Electron Microscopy  
SLIPS – Slippery Liquid-Infused Porous Surfaces  
TEM – Transmission Electron Microscopy  
TEOS – Tetraethoxysilane  
UV – Ultraviolet  
WCA – water contact angle  
XRD – X-ray diffraction spectroscopy

## INTRODUCTION

**Relevance of the topic:** Textured surfaces represent a new class of functional materials with a range of beneficial properties. Depending on their surface energy, these materials can exhibit behaviors ranging from fully hydrophilic to superhydrophobic, particularly when the Cassie-Baxter effect is achieved. This versatility opens up numerous possibilities for applications, such as the creation of self-cleaning surfaces, controlled adhesion, gas bubble nucleation during boiling, reduced frosting, and friction reduction in liquid transport. However, the widespread adoption of such surfaces in technology is hindered by their limited scalability, as their production requires specialized methods such as photolithography, vacuum deposition, and electro-deposition. A promising solution to this challenge lies in the use of organic polymer-based coatings filled with dispersed mineral oxide particles that form the surface texture. The shape of these particles, particularly their hierarchical structure, and their intrinsic surface energy, play a critical role in the material properties. This work focuses on examining the influence of these factors using micro-sized red mud particles, titanium dioxide, silicon, and zinc nanoparticles, as well as composites derived from them. The study also explores the potential of micro-textured aluminum oxide as a means to achieve superhydrophobic and superhydrophilic surfaces.

**The connection of the work with scientific programs, plans, and topics:** The topic of the dissertation is included in the scientific work plan approved by the Department of Chemical Technology of Composite Materials at Igor Sikorsky Kyiv Polytechnic Institute, taking into account the law of Ukraine “About priority directions of science and technics development” No. 2623-III dated 11.07.2001 on the relevance of the thesis topic to the direction “novel substances and materials”.

**The purpose of the research:** The purpose of this study is to establish the connection between the structure and water repellency of organo-mineral surfaces.

**Objectives of the research:**

- to establish the basic principles of water repellency formation in organo-mineral textured systems;
- to obtain and characterize mineral disperse particles with different surface configuration/size;
- to study and tune the formation of water repellent ability of organo-mineral coatings;
- to demonstrate prospective use of obtained coatings;

**Research Object:** textured surfaces with tuned water repellency on the base of organic interface layer and mineral texture forming elements

**Research subject:** formation of water repellency of textures consisting of mineral structure formers and organic binding and interface layers.

**Research Methodology:** The research employed a comprehensive experimental methodology combining material synthesis, composite formulation, and systematic performance evaluation to establish correlations between the structure of organo-mineral coatings and their water-repellent properties. The approach involved the preparation of inorganic fillers (ZnO, TiO<sub>2</sub>, SiO<sub>2</sub>, and their composites) with controlled particle size, shape, and hierarchical morphology using precipitation and hydrothermal synthesis, followed by their incorporation into polymer matrices to produce coatings via casting or spraying. A wide range of instrumental methods was applied to characterize the obtained materials. Scanning and transmission electron microscopy (SEM, TEM) were used to examine surface morphology, particle size, and microstructural features, while X-ray diffraction (XRD) provided phase composition and crystallinity data. X-ray photoelectron spectroscopy (XPS) was employed for surface elemental and chemical state analysis. Diffuse reflectance spectroscopy (DRS) and photoluminescence (PL) spectroscopy were used to assess optical properties and

defect states of the fillers. Wettability was evaluated by static water contact angle measurements with statistical analysis to determine reproducibility and significance of differences between samples. Fourier-transform infrared spectroscopy (FTIR) was applied to study chemical bonding, functional groups, and filler–matrix interactions in the coatings.

### **Scientific novelty:**

- For the first time, it has been demonstrated - using red mud as an example - that surface inactivation of its particles, achieved by reducing their polarity through thermal treatment at 950 °C and modification with organosilicon compounds, enables the effective use of such waste as texture-forming components in the production of coatings with pronounced water-repellent properties. In particular, contact angles of approximately 143° were achieved on the treated surfaces.
- This study advances the theoretical understanding of the formation of water-repellent surfaces composed of dispersed micro- and nanoparticles embedded in organic polymer matrices. It was shown that particle surface topography and their chemical inertness play a critical role in generating effective surface texture. Additionally, fine-tuning the ratio between the polymer and the film-forming agent allows precise control over the coating structure, enabling the achievement of maximum contact angles. In this work, contact angles as high as 154° were obtained.
- This study further develops the understanding of the synthesis of zinc oxide (ZnO)-based particles with tunable morphology. It has been demonstrated that the particle shape is governed by a combination of factors, including the type of catalyst used, the synthesis temperature, the presence of dopants such as TiO<sub>2</sub> and SiO<sub>2</sub>, and the ZnO-to-dopant ratio. By adjusting these parameters, it is possible to control the particle morphology, ranging from plate-like structures typical of pure ZnO to complex hierarchical architectures characteristic of doped forms.

- It has been shown that doped forms of zinc oxide (ZnO) crystals exhibit pronounced photoactivity. This effect is significantly enhanced when titanium dioxide (TiO<sub>2</sub>) is used as a dopant. Specifically, photoluminescence analysis revealed that at a ZnO:TiO<sub>2</sub> ratio of 2:1, the photoactivity increases by approximately 6.5 times compared to undoped ZnO.
- For the first time, it has been demonstrated that the use of titanium-dioxide-doped zinc oxide particles with a highly developed surface structure leads to a significant enhancement in water-repellent properties compared to conventional nanoscale ZnO particles. At high filler loadings, the contact angle increases from 135° to 154°, classifying such coatings as superhydrophobic.
- It has been demonstrated for the first time that the developed hierarchical micro/nanostructure of doped zinc oxide particles enables the formation of highly water-repellent surfaces across a broad range of mass ratios between the polymer matrix and the mineral texture-forming particles. Specifically, when the content of doped ZnO/CO<sub>2</sub> particles ranges from 20% to 60%, contact angles remain above 140°. In contrast, the use of individual TiO<sub>2</sub>, CO<sub>2</sub>, or ZnO particles results in such high water-repellent performance only within much narrower concentration ranges.
- It has been shown that coatings containing texturing elements based on modified ZnO particles doped with TiO<sub>2</sub> and SiO<sub>2</sub> exhibit high resistance to UV-induced hydrophilization. These coatings transition from the Cassie–Baxter state to the Wenzel state only after 170 hours of UV exposure, while maintaining a contact angle of approximately 120°. Complete hydrophilization occurs only after 250–280 hours of continuous irradiation.
- It has been shown that textured surfaces, particularly those with hierarchical micro/nanostructures, are effective for fog water collection. The efficiency of water harvesting significantly increases upon hydrophilization of the surface, with an observed improvement of approximately 30–45% compared to hydrophobic surfaces.

### **The Practical Significance of the Obtained Results.**

- In the course of this work, a novel synthesis method was developed for doped hierarchical ZnO–SiO<sub>2</sub> and ZnO–TiO<sub>2</sub> particles. These materials can serve as a basis for water-repellent textured coatings and are also considered promising hydrophilic materials for atmospheric moisture harvesting. Additionally, both types of particles exhibit pronounced photoactive properties, expanding their potential for use in multifunctional surface applications.
- The developed organo-mineral coating formulations based on composite hierarchical ZnO particles doped with titanium dioxide and silicon dioxide exhibit stability under ultraviolet irradiation for over 170 hours. These coatings retain their hydrophobic properties under prolonged UV exposure, making them promising candidates for use as UV-resistant water-repellent surfaces.

**Contributions of the author:** All scientific results, conclusions, and statements presented for defense were obtained by the applicant personally. In the co-authored scientific works, the applicant participated in task formulation, conducting the experimental research, discussing and summarizing results, and writing and formatting the articles. In the co-authored publications, the author's contribution is primary. The research results have been presented by the applicant personally at scientific conferences. The co-authors of the scientific works are the scientific supervisor and researchers with whom the joint studies were conducted.

**Approbation of the results of the dissertation:** The results of the study were presented and discussed at 3 international conferences: “Composite Materials” (2023, 2024, Kyiv, Ukraine) and IEEE 5th KhPI Week on Advanced Technology (2024, Kharkiv, Ukraine)

**Publications.** The study results were published in 6 scientific publications, that are 6 scientific papers published in profile journals: 4 in category B of profile journals of Ukraine and 2 - indexed in Scopus international citations database.

**Structure and scope of work**

The paper consists of an introduction, six chapters, a conclusion, a list of 114 references. The total number of pages in the paper is 165, with 133 pages for the main part. It includes 46 figures, 14 equations, and 19 tables.

## **CHAPTER 1. Formation of water repellent properties of composite coatings with mineral fillers and polymer matrix**

### **1.1. Research and application of superhydrophobic materials**

Superhydrophobicity refers to surfaces with a water contact angle of more than  $150^\circ$  and a sliding angle of less than  $10^\circ$  with water. With the progress of society and the continuous development of technology, superhydrophobic materials have broad application prospects in people's lives and the field of science and technology due to their unique properties [1]. There are many superhydrophobic phenomena in nature, such as lotus leaves. Barthlott [2], the discoverer of the 'lotus effect', and his colleague Neinhuis [3] summarised the contact angles and surface materials of the surfaces of hundreds of plants. The surface materials and structures have long-term stable superhydrophobic properties. Research has shown that the superhydrophobic properties of the surfaces of plant leaves such as lotus leaves and taro leaves are caused by a special structure combining micro and nanostructures and the presence of surface waxes. At present, an important direction of research on the hydrophobic part of solid surface materials is to imitate the microstructures of these plant leaf surfaces [4] and use various technical means to create superhydrophobic surfaces [5]. Researchers have studied the relationship between the surface roughness and chemical composition and surface wettability, and used a biomimetic approach [6] to construct various micro- and nano-scale surface structures to obtain a variety of superhydrophobic surfaces. In addition, superhydrophilic [7] and superhydrophobic superoleophilic [8] surfaces have also been prepared, which provides a direction for promoting the research on superhydrophobic materials.

The research on superhydrophobic surfaces can be roughly divided into two different categories: one is to establish theoretical models to characterize the various properties of superhydrophobic surfaces through physical and chemical principles, and modify the models as needed [9]; the other is the research on new materials, advanced

manufacturing technologies and their applications in the preparation of superhydrophobic surfaces [10]. The establishment and development of theoretical models is not only for the purpose of explaining and analysing wetting phenomena on solid surfaces, but more importantly, it is to obtain material surfaces with specific functions by regulating the wettability of the material surface, so as to solve the problems faced by the material in service due to special environmental or functional requirements.

At present, superhydrophobic surfaces that mimic those in nature have been prepared and are widely used on various material substrates, such as glass [11], metal [12], fabric [13], polymers [14], etc. This special phenomenon occurs because water droplets will remain on superhydrophobic surfaces rather than covering them.

## 1.2. Fundamentals of surface wetting

Surface wettability (also known as wettability) is a very important characteristic of solid surfaces. It refers to the ability of a liquid to displace a gas and spread on a solid surface [15]. This property has a significant impact in many fields, including daily life, industry, agriculture, etc., and its research covers multiple disciplines such as chemical, biological and physical engineering [16][17][18] [19].

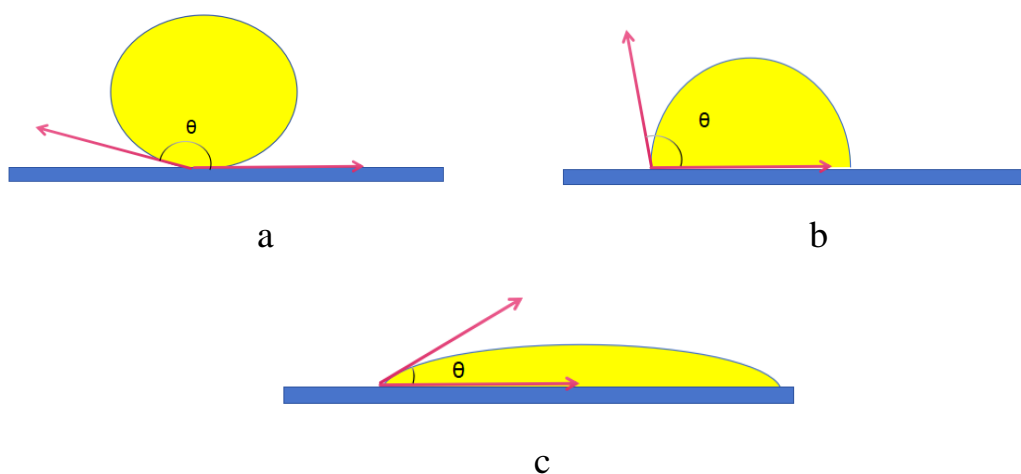


Figure 1.1 Wetting states: a – superhydrophobic; b – hydrophobic; c – hydrophilic.

The angle formed by the liquid spreading naturally on the solid surface is the contact angle  $\theta$ . By measuring the contact angle of a material's surface, the material can be classified as superhydrophobic ( $180^\circ > \theta > 150^\circ$ ), hydrophobic ( $150^\circ > \theta > 90^\circ$ ) and hydrophilic ( $\theta < 90^\circ$ ) (Fig. 1.1) [20].

Beyond surface roughness and chemical composition, several other factors can significantly influence the measured water contact angle. One such factor is surface contamination - adsorbed organic molecules, dust, or residual solvents can alter surface energy and affect wettability. Ambient conditions such as temperature and humidity also play a role; for instance, higher humidity can lead to condensation on the surface, reducing contact angles. Additionally, the method of droplet deposition and the droplet volume can introduce variability, as larger droplets may flatten more due to gravity. Surface aging or exposure to ultraviolet light can further modify the surface state, especially in photoactive materials like ZnO, leading to time-dependent changes in contact angle measurements. These variables must be carefully controlled to ensure reliable and reproducible wettability data.

The factors affecting the wettability of a solid surface are the solid surface's free energy and surface roughness. The solid surface's free energy, directly affects the wettability of a liquid droplet and its contact angle. The greater the surface's free energy value, the more easily the surface is wetted by the water; the smaller the surface's free energy value, the more difficult it is to be wetted. According to the difference in surface tension, solid surfaces can be divided into two main categories: one is low surface energy surfaces, generally organic solids and polymers such as polytetrafluoroethylene and other high polymers are low surface energy (usually less than 30 mJ/m<sup>2</sup>) [21], the PTFE surface is difficult to wet with water, because water does not spread spontaneously on a solid with a surface free energy of less than 72.8 mN/m [22]. The second type is a surface with high surface energy, generally inorganic salts, metal oxides, etc. This type is a hydrophilic surface, and the surface is easily wetted by water. For example, clean glass has a surface energy of approximately 200–300 mJ/m<sup>2</sup>, while titanium dioxide (TiO<sub>2</sub>) exhibits a surface energy around 280 mJ/m<sup>2</sup>. In contrast, water

has a surface tension of 72.8 mN/m at room temperature, so when the solid's surface energy significantly exceeds this value, water spreads easily across it. As a result, such materials typically exhibit low contact angles with water, often below 30°, indicating strong hydrophilicity.

The surface energy parameter of a substance can be used as a basis not only to measure its surface hydrophilicity, but also its hydrophobicity. For solid surfaces with low surface energy, the wettability can be changed when the hydrogen in the contained polymeric hydrocarbons is replaced by other elements. The more hydrogen atoms are replaced by other atoms, the lower the free energy of the solid surface becomes, and water droplets cannot spread on its surface, so it exhibits hydrophobicity. Yin et al. [23] etched copper sheets with a mixed solution of sodium hydroxide and persulfate at a certain concentration ratio to obtain a rough surface with a lotus-like structure. Then, the rough surface was modified with lauric acid, which has a low surface energy, to convert it from superhydrophilic to superhydrophobic, illustrating the influence of surface chemical composition on surface wettability. It has also been found that another important factor affecting the wettability of solid surfaces is the roughness of the solid surface.

Surface roughness can affect the behaviour of liquid droplets on solid surfaces [24], so the factor of surface roughness plays a very important role in the study of surface wettability. Increasing the surface roughness not only makes the solid surface more hydrophobic, but also changes the size of its contact angle. Therefore, by changing and regulating the chemical composition, micro and macro geometric structure of the solid surface, the surface wettability can be artificially controlled.

Surface wettability is one of the most important properties of solid surfaces. In 1805, Young proposed the equation for the static contact angle of a liquid on an ideally smooth solid surface [25]. The principal distribution of surface forces is shown in Fig. 1.2, and in the form of equation is listed as follows (1):

$$\gamma_{SV} - \gamma_{SL} = \gamma_{LV} \cos \theta \quad (1)$$

where  $\gamma_{SV}$  represents the interfacial tension between solid and gas,  $\gamma_{SL}$  represents the interfacial tension between solid and liquid,  $\gamma_{LV}$  represents the interfacial tension between liquid and gas, and  $\theta$  represents the intrinsic contact angle of the solid surface.

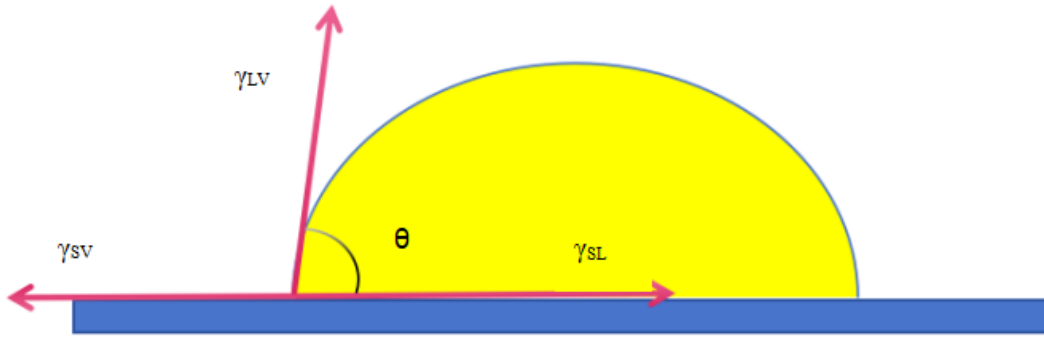


Figure 1.2 Illustration of Young equation

It can be seen from Young's equation that, when other conditions remain unchanged, by reducing the surface free energy of the solid, the contact angle will increase and hydrophobicity will be enhanced. Conversely, when the surface free energy of the solid increases, the contact angle will decrease and hydrophilicity will be enhanced. Nakamae et al. [26] formed a  $-\text{CF}_3$  group on a glass surface to form a hexagonal arrangement of smooth solid surfaces with a surface energy of  $6.7 \text{ mJ/m}^2$ , which is considered to have the lowest surface energy of a solid surface, however, the contact angle with water is only  $119^\circ$ , while in reality the contact angle of many rough surfaces such as lotus leaves with water is as high as  $160^\circ$ . This is far beyond the scope of Young's model. Therefore, Young's model is only applicable to ideal smooth surfaces. To analyse the formation mechanism of the high contact angle on the surface of some natural plant leaves, the effect of surface roughness on the apparent contact angle must be considered.

The Young equation discusses the situation limited to an ideal smooth surface, while in reality the roughness of a solid surface directly affects its wettability. The Wenzel [27] first proposed a wetting model for rough solid surfaces and introduced the roughness factor  $r$ . After the introduction of roughness, there are two types of contact

angles on solid surfaces: the contact angle measured on an ideal surface is the intrinsic contact angle, while the contact angle measured on a surface with a different rough structure is called the apparent contact angle. It is assumed that when a water droplet contacts a rough surface, the water droplet can completely submerge in the grooves of the rough surface to form a uniform solid-liquid interface. The hydrophobicity can be improved by increasing the roughness of the solid surface. In the Wenzel model (Fig. 1.3. a), the roughness  $r$  can significantly increase the actual contact area between the solid and liquid phases, and the actual contact angle satisfies the following formula (2):

$$\cos \theta\pi = \frac{r(\gamma^{SV} - \gamma^{SL})}{\gamma^{LV}} = r \cos \theta \quad (2)$$

where  $\theta\pi$  represents the apparent contact angle of the real rough solid surface,  $\theta$  represents the solid surface's intrinsic contact angle, and  $r$  represents the roughness (The ratio of the actual area to the geometrically projected area of the rough surface) [28]. As can be seen from the definition of the surface roughness factor  $r$ ,  $r > 1$ , the contact angle of a rough surface with a liquid is greater than the contact angle of a smooth surface with a liquid  $\theta$ . For hydrophobic surfaces with low surface energy, the rougher the surface structure, the greater the contact angle and the more hydrophobic it becomes. The Wenzel equation reveals the relationship between the apparent contact angle and the intrinsic contact angle of a homogeneous rough surface. However, it is not applicable when the solid surface is composed of different types of materials.

For this reason, Cassie and Baxter [29] further developed Wenzel's theory and concluded that the contact of a liquid drop with a rough surface is a composite contact. When the gaps on a rough surface are very small (Fig. 1.3 b), the liquid droplets cannot penetrate into the gaps. In this case, the grooves on the rough surface will trap some air, which supports the liquid droplets and prevents complete wetting. Assuming that the solid surface is composed of substances 1 and 2, the surfaces of these two different components are uniformly distributed on the surface in the form of very small blocks (each block has an area much smaller than the droplet size). Their intrinsic contact angles can be expressed as  $\theta_1$  and  $\theta_2$ , respectively, and  $f_1$  and  $f_2$  are the surface area

fractions occupied by the liquid droplet's contact with the gas and solid phases ( $f_1+f_2=1$ ). The formula is (3):

$$\cos \theta \pi = f_1 \cos \theta 1 + f_2 \cos \theta 2 \quad (3)$$

In general, when the liquid is water, since the intrinsic contact angle of water on an air surface is  $180^\circ$ , it can be rewritten as formula (4):

$$\cos \theta \pi = f_1 (\cos \theta 1 + 1) - 1 \quad (4)$$

This shows that the greater the air retained on the surface, the greater the contact angle. In general, constructing a nanometer rough structure on the surface of a material will make the surface of a hydrophilic material more hydrophilic and the surface of a hydrophobic material more hydrophobic. This is the principle of changing the surface properties of a material.

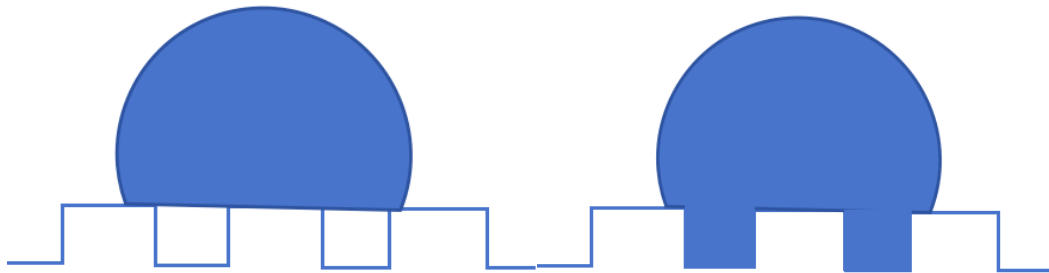


Figure 1.3 Wetting anomalies: a – Cassie-Baxter state; b – Wenzel state

In addition to promoting high apparent contact angles, the Cassie wetting state offers significant functional advantages, particularly low contact angle hysteresis and a reduced sliding angle. These characteristics mean that water droplets can easily roll off the surface with minimal tilt or external force, often at angles below  $10^\circ$ . This behavior contributes to excellent self-cleaning properties, as rolling droplets effectively pick up and remove dust, contaminants, or microbes. Moreover, the reduced

contact time between water and the surface enhances anti-icing and anti-corrosion performance, making Cassie-state surfaces ideal for applications in outdoor coatings, solar panels, and aerospace components.

Wenzel and Cassie models indicate that the surface roughness is integral in promoting hydrophilicity and hydrophobicity on surfaces. Many superhydrophobic surfaces in nature have significant roughness and micro/nano-structures [30]. Scientists have used various methods to mimic naturally occurring superhydrophobic surfaces.

### 1.3. Methods of superhydrophobic surfaces obtaining

According to the two factors affecting wetting mentioned above, the construction of superhydrophobic coatings also usually needs to satisfy these two basic conditions: (1) a microstructure with a certain degree of surface roughness; (2) a chemical component with a low surface energy. That is to say, the rough structure with micro-nanocomposite is prepared first, and then low surface energy substances are used to modify it; or a certain micro-nanocomposite structure is constructed directly on the surface of low surface energy materials. At present, the main methods commonly used to prepare superhydrophobic coatings on the surface of solid materials are: photo-etching, sol-gel method and so on.

Lithography is a method used to transfer computer-designed patterns onto a substrate surface, and is a widely used method for preparing superhydrophobic surfaces. Currently, several methods are commonly used, such as laser etching, plasma etching, and chemical etching. Lan et al. [31] used nanosecond laser etching to construct a grid-like microstructure with grooves and pits on the surface of stainless steel. After self-assembly with fluorosilane, an ultra-sup hydrophobic surface with a contact angle of  $164^\circ$  and a rolling angle of  $3^\circ$  was prepared, which could be ultrasonically treated for 75 minutes and exhibited good stability.

The sol-gel method involves adding a chemical precursor to water to cause hydrolysis or condensation, forming a gel with a three-dimensional network structure through cross-linking between sol particles, and then constructing a nanostructure through drying and sintering. Finally, the material is modified to be hydrophobic to obtain a superhydrophobic coating. When the precursor contains low surface energy substances, the sol-gel method can produce superhydrophobic coatings without the need for subsequent hydrophobic treatment. The sol-gel process is simple, and can produce materials with special physical properties such as low thermal expansion coefficient, low ultraviolet absorption and high visible light transmittance. It is of great significance for the realization of multifunctional superhydrophobic coatings.

Chen et al. [32] prepared organo-inorganic hybrid modified silica sol, which can be dip-coated on a variety of flat and curved substrates. The superhydrophobic coating prepared can be used for oil-water separation, and the separation effect can reach 80%. In addition, the sol-gel process parameters were also investigated, and it was found that the water content, ammonia content and low surface energy substance concentration have an important effect on the hydrophobicity of the coating.

In nature, lotus leaves are considered to be a model for superhydrophobic surfaces. The structure of these leaves consists of two nanometer/micrometer-scale natural wax coverings over the entire surface. Lotus leaves have high superhydrophobicity, with a WCA of  $>160^\circ$ . The surface of the lotus leaf remains clean even when covered in mud and dirt. Etching technology is mainly inspired by this natural structure, with the main purpose of increasing the surface roughness of the substrate.

Zheng et al. [33] prepared a superhydrophobic coating with a micro-nano hierarchical structure on basalt scales by NaOH etching and fluorination modification, with a contact angle of up to  $165.1^\circ$  and a rolling angle as low as  $0.7^\circ$ . It has excellent wear resistance, UV resistance, corrosion resistance and antibacterial properties.

Chemical vapour deposition (CVD) is a technique that involves the deposition of a gas precursor on a heated substrate to form a desired solid film. CVD involves a

chemical reaction. CVD can be used to prepare rough surfaces, prepare micro/nanoparticles, transform nanorods into macrostructures, or deposit a thin hydrophobic film on a rough surface. CVD as a technique for depositing hydrophobic films is currently an area of great interest to researchers.

Huang et al. [34] used induced chemical vapour deposition (iCVD) to construct transparent superhydrophobic coatings with customised nano-cone array structures. This iCVD process uses aggregated nanoscale monomers as nucleation centres, which subsequently produce vertically aligned polymer nano-cones. By adjusting the deposition conditions, the height and density of the nano-cones can be precisely controlled. The resulting polymer nano-cone array coating achieves a contact angle of  $151^\circ$  and a rolling angle of  $2^\circ$  in the visible light range. rolling angle, an average visible light transmittance of 94.5%, and excellent self-cleaning ability and resistance to water droplets and sand impacts. This indicates that the coating prepared by this method can maintain long-term mechanical durability in outdoor environments and has potential practical application value. However, this type of method is time-consuming and often uses organic solvents, which can cause environmental pollution.

However, the use of superhydrophobic surfaces still has many problems, such as lack of durability, poor performance, and high preparation costs, which limits the large-scale promotion and application of superhydrophobic surfaces [35]. Nanomaterials have attracted widespread attention due to their special properties, which makes their application in nano-coatings a matter of great interest.

Combining nanomaterials with surface coating technology to prepare surface composite coatings containing nanoparticles can improve the modification effect of surface technology. Superhydrophobic nanocoatings refer to coatings containing at least one nanoscale component, in which the morphology or properties of the nanoscale scale play a key role in the superhydrophobic properties. In recent years, there has been increasing interest in the manufacture of superhydrophobic nanocoatings with micro-to-nanoscale structures. A variety of nanofillers have been used to prepare superhydrophobic coatings, such as nano-titanium dioxide [36], nano-zinc oxide [37],

nano-silica [38], etc. These superhydrophobic nanocoatings have been widely used in industrial production and have shown broad application prospects in various fields.

Nanomaterials have attracted attention due to the particularity of their physical and chemical properties caused by their special structure [39]. Broadly speaking, nanomaterials generally refer to materials that are measured at the nanoscale in terms of external dimensions or internal structure and exhibit additional or different unique properties. When the size of a material is between 1 and 100 nm, its physical and chemical properties change, exhibiting many strange phenomena that are different from both macroscopic objects and individual isolated atoms. These strange phenomena include, but are not limited to, properties such as magnetism, light, electricity, melting point, surface tension and solubility. The physical properties of nanoparticles change from classical physics to quantum physics as their size changes, so changing the size or composition of nanoparticles can change their physical and chemical properties.

In 1991, carbon nanotubes were discovered [40]. They are one sixth the mass of steel of the same volume, but 10 times stronger, so nanotechnology has become a hot topic in scientific research. Nanomaterials, also known as ultrafine particle materials, are composed of nanoparticles and are in a transitional region at the boundary between atomic clusters and macroscopic objects. From the usual microscopic and macroscopic point of view, such a system is neither a typical microscopic system nor a typical macroscopic system, but a typical mesoscopic system. It has surface effects, small size effects and macroscopic quantum tunnelling effects. When a macroscopic object is broken down into ultrafine particles, it will exhibit many strange properties, that is, its optical, thermal, electrical, magnetic, mechanical and chemical properties will be significantly different from those of a large solid.

#### 1.4. Use of ZnO as the texture forming element of superhydrophobic coatings

With the rapid development of science and commerce, people have gained a deeper understanding of nano-semiconductor materials. In long-term research, it has been found that ZnO semiconductor nanomaterials have more advantages. Nano zinc oxide is a new type of multifunctional inorganic material with a particle size of about 1-100 nm. Due to the miniaturisation of the grains, the surface electronic structure and crystal structure change, and it has high transparency and good dispersion. In addition, zinc oxide exhibits many special properties, with excellent thermal stability and unique mechanical, optical and electrical properties. In addition, zinc oxide also has piezoelectric and pyroelectric properties.

Zinc oxide (ZnO) is an important direct wide band gap semiconductor material. Its band gap is 3.37 eV at room temperature, and the binding energy of excitons is 60 meV. Due to its small particle size and large specific surface area, nanometer-scale ZnO exhibits many unique physical and chemical properties in optics, electronics, catalysis, magnetism, biology and electrical engineering.

This inherent polarity, resulting from the wurtzite crystal structure and strong ionic bonding between  $\text{Zn}^{2+}$  and  $\text{O}^{2-}$ , gives ZnO surfaces a high surface energy and strong affinity for water molecules. As a result, nanostructured ZnO often demonstrates superhydrophilic behavior, with water contact angles approaching  $0^\circ$ , especially after UV irradiation or surface activation. The presence of polar  $-\text{OH}$  groups on the surface, formed through adsorption of moisture from the environment, further enhances its hydrophilicity. This makes ZnO a promising candidate for applications requiring water spreading and film formation, such as antifogging coatings, photocatalytic surfaces, and biomedical devices.

ZnO is a 'green' environmentally friendly material that is cheap, non-toxic, biodegradable and biocompatible. It is an important functional material for semiconductors. At present, the wide application of high-performance materials is increasingly dependent on the control of the grain size and morphology of the

constituent materials. Nano ZnO has excellent properties that bulk materials cannot match, such as non-toxicity, non-migration, fluorescence, piezoelectricity, and the ability to absorb and scatter ultraviolet light. The emergence of novel morphologies such as nano ZnO in the form of flowers, hexagonal flakes, needles, and lines will bring many excellent properties. Therefore, adjusting the surface roughness of the material and reducing the surface free energy are two effective ways to improve the wettability of the material surface. The surface wettability of ZnO can be controlled by regulating its surface morphology, as in Myint [41] studied the synthesis and properties of superhydrophobic surfaces composed of ZnO. Nano-ZnO, which is hydrophilic in nature, is used as the zinc source to construct a superhydrophobic surface without chemical modification. Nano-ZnO seeds are printed on a glass slide using inkjet printing to form a microconvex hull, and then ZnO microcrystalline rods are generated by hydrothermal method to obtain a superhydrophobic surface. The measured surface contact angle is  $153^\circ$ . This method can be used in industrial applications, such as self-cleaning windows or car roof windows. In addition, the size of the microconvex hull can be adjusted to determine the optimal combination of a binary rough surface (created by a double surface topography) that meets the criteria for the lotus effect.

The method of reducing surface energy is to modify the material with some commonly used low surface energy substances such as siloxanes and fluorides. These substances mainly modify the surface of nano-ZnO by breaking chemical bonds and breaking chains to form a hydrophobic surface by covalent bonding. The microstructure of the modified nano-ZnO does not change, and nano-ZnO materials with both semiconductor properties such as light, electricity and magnetism, and superhydrophobic properties can be obtained. Guo et al. [42] prepared transparent ZnO nanorod array films by hydrothermal method. The reaction used  $\text{Zn}(\text{CH}_3\text{COO})_2 \cdot 2\text{H}_2\text{O}$  as the zinc source, and an 18-mercaptol solution as a low surface energy substance to modify the obtained film, so that the hydrophobic angle of the superhydrophobic coating changes from  $9.6^\circ$  to  $156^\circ$  after modification.

At present, the design and controlled growth of ZnO nanoparticles is the direction for the future application and preparation of ZnO nanomaterials. In short, ZnO nanomaterials have broad application prospects in fields such as catalyst supports, optics, and biosensors [43].

One of the key advantages of working with ZnO is the well-established and versatile nature of its synthesis methods. A wide range of morphologies - such as nanorods, nanoflakes, nanospheres, and hierarchical flower-like structures - can be readily obtained through controlled hydrothermal, sol-gel, or chemical vapor deposition techniques. This morphological tunability provides an excellent opportunity to systematically study how different surface architectures influence the formation of superhydrophobic properties when combined with low surface energy modifications. By tailoring the surface roughness at the micro- and nanoscale through specific ZnO structures, it becomes possible to enhance water repellency and optimize the coating's performance for targeted applications.

There have been many studies on hydrothermal synthesis of zinc oxide with different morphologies [44], but few studies on its use in hydrophobic coatings. Therefore it is a perspective research direction.

There are many methods for preparing nano-ZnO, which are divided into chemical and physical methods depending on whether a chemical reaction occurs. Among these methods, the chemical method is a method for preparing ZnO materials of different sizes and morphologies by reacting zinc salts chemically, while the physical method refers to a method for crushing bulk ZnO materials into nano-ZnO materials using mechanical methods in addition to chemical methods. Among them, the preparation of ZnO is mainly based on chemical methods. According to the state of the raw materials during the preparation process, it can be divided into three categories: solid phase method, liquid phase method and gas phase method. Common chemical methods for preparing nano ZnO include precipitation method, sol-gel method, hydrothermal method, microemulsion method, etc. Among them, the liquid phase method is currently

the most widely used method in research. This article mainly describes the chemical method (hydrothermal method) for preparing nano ZnO particles.

Solid-phase methods for preparing nano ZnO include mechanical crushing and solid-phase chemical reaction methods. Mechanical crushing is a method in which ZnO or zinc raw materials are directly crushed and ground mechanically to produce ZnO nanoparticles. However, it has its own disadvantages, such as low efficiency, high energy consumption, uneven powder particles, and easy mixing of impurities, which is why this method is rarely used to produce ZnO. The solid-phase chemical reaction method uses zinc metal salts or oxides as raw materials, which are mixed and ground with other solid raw materials, and then calcined at high temperatures to form ZnO nanocrystals through a solid-phase reaction. The heating rate and temperature during the calcination process cause different temperatures inside and outside the ZnO material system result in a temperature difference inside and outside the material, which in turn has a certain degree of impact on the structure or crystallinity of the material [45].

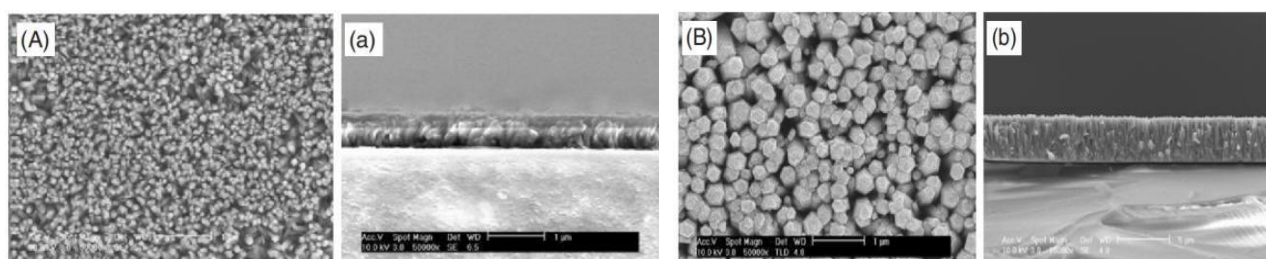
The hydrothermal method was first studied by geologists in the mid-19th century to simulate natural mineralization. After 1900, scientists established the theory of hydrothermal synthesis, and later began to shift their research to functional materials. Hydrothermal synthesis belongs to the field of liquid phase chemistry. It is an effective method of inorganic synthesis and materials processing in which an aqueous solution is used as the reaction system in a specially designed sealed reactor, and the reaction system is heated and pressurised. Hydrothermal methods are one of the most commonly used methods for preparing nanomaterials. [46]. Its main advantages are as follows:

(1) The hydrothermal method uses medium-temperature liquid-phase control, which has relatively low energy consumption and is widely applicable. It can be used to prepare not only ultrafine particles, but also single crystals with larger sizes, and inorganic ceramic films can also be prepared. (2) The raw materials are relatively cheap and easy to obtain. The reaction takes place in the liquid phase with rapid convection,

resulting in high yield, uniform phase, high purity, good crystallinity, and controllable shape and size. [47] (3) During the hydrothermal process, factors such as reaction temperature, pressure, treatment time, solution composition, pH value, and the types of precursors and mineralizers can be adjusted to effectively control the reaction and crystal growth characteristics. [48], (4) The reaction is carried out in an airtight container, and the reaction atmosphere can be controlled to form suitable redox reaction conditions to obtain certain special phases. This is especially beneficial for synthetic reactions in toxic systems, which can minimize environmental pollution.

Hydrothermal reactions provide a special physical and chemical environment for the reaction and crystallisation of various precursors that cannot be obtained under normal pressure conditions. Generally, the temperature of a hydrothermal reaction is controlled at 100-200°C. Different conditions can be adjusted to achieve different preparations. In a hydrothermal reaction system, the morphology of nanomaterials can be changed by changing the type of specific solvent, pH, temperature and pressure in the reactor, so it is also very beneficial for the preparation of nanoscale materials. [49]

2009, Yu et al. [50] Using ammonia-hexahydrate zinc nitrate as a raw material, Zn O nanorod arrays with an average diameter of about 500 nm and a length of about 7  $\mu\text{m}$ . By controlling the solution concentration, nanorod arrays with different morphologies were prepared (as shown in the Fig. 1.4.). Experiments have shown that ammonia plays a key role in the growth of ZnO nanorod arrays, because the appropriate amount of ammonia can inhibit homogeneous nucleation in the growth solution and reduce unnecessary consumption of solutes. The reaction mechanism of this process is as follows: (1) ammonia provides a complex  $[\text{Zn}(\text{NH}_3)_4]^{2+}$ , (2) provides the alkaline environment required for the growth of ZnO nanorods (Fig. 1.4):



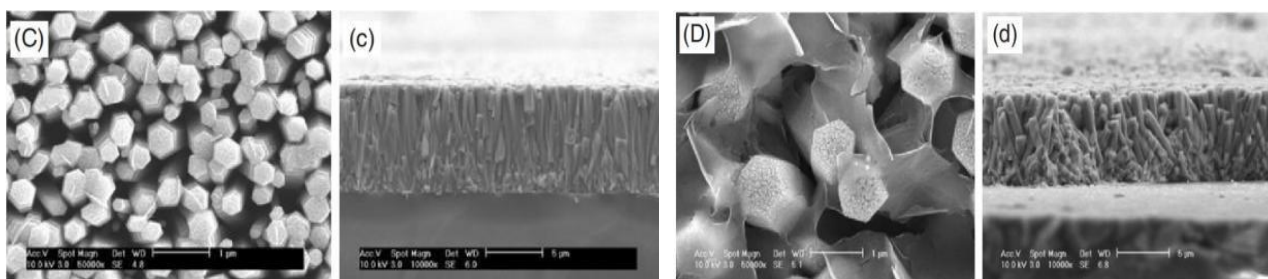


Figure. 1.4 SEM images of ZnO arrays prepared with different zinc salt concentrations: A, (a) 0.05 M; B, (b) 0.10 M; C, (c) 0.15 M; D, (d) 0.20 M. (taken from [51])

The sol-gel method mainly involves the two most basic reactions of hydrolysis and polymerisation. A stable sol is first formed in a solution, which then ages to form a gel. Finally, the gel is solidified and sintered to finally synthesise the required micron- or nanometre-scale material. This method has been widely used in the preparation of glass, ceramics, fibres, composite materials, etc. At present, many researchers have widely applied the sol-gel method to the preparation of nano ZnO. The advantages of this method are that the nano powder prepared has a relatively uniform distribution, the particle size is controllable, and the equipment used is simple and easy to operate. The disadvantage is that some of the raw materials used are organic compounds, which are harmful to health.

Hayat et al. [52] Nano ZnO particles of different sizes were successfully synthesized using the sol-gel method. It was found that as the calcination temperature increased, the nano ZnO particles tended to agglomerate, while the activity of the catalyst decreased. The sample obtained under calcination conditions of 500 °C had higher photocatalytic oxidation activity towards phenol. The main reason is that the smaller particle size of nano ZnO-500 results in better dispersion and uniformity

The microemulsion method is one of the common methods for preparing nano powders. It is a method of precipitating a solid phase from an emulsion formed by two immiscible solvents with the help of a surfactant. Nanoparticles prepared using this method have small particle sizes, narrow distributions, high surface activities, good

monodispersity, and are not prone to agglomeration [53]. The key factor determining the structural form of nanoparticles is the microstructure of the inverse microemulsion. When the components are constant, the main influencing factors are the molar ratio of water to surfactant, the content of surfactant in the oil phase, the mass ratio of co-surfactant to surfactant, and the concentration of reactants.

Chemical Vapor Deposition (CVD) is one of the most widely used techniques in the semiconductor industry for depositing a variety of materials. It mainly uses two or more gaseous raw materials to form various ions through chemical reactions in the gas phase, and then goes through the two stages of nucleation and growth in the gas phase, finally generating thin films, particles, crystals and other solid materials on the wafer. Mainly includes: physical vapor deposition [54], chemical vapor deposition [55], spray pyrolysis [56], magnetron sputtering [57] and molecular beam epitaxy [58]. Nanomaterials synthesized using the CVD method have a relatively high degree of purity because the particles nucleate and grow in the gas phase, where there is a lot of space, and the resulting product particles are smaller in size and more uniform in shape, with good monodispersity. Moreover, the entire reaction process is carried out in a sealed container, which ensures that the generated particles are highly pure, and the relative product purity is high.

Lupan et al. [59] obtained ZnO nanowires with diameters between 50 and 200 nm by CVD at 650 °C. The method uses the vapor from solid zinc evaporation as the Zn source and an oxygen-argon mixture as the gas-phase reactant introduced, and the growth of vertically aligned nanowires is controlled by controlling the molar ratio of O to Zn. This single ZnO nanowire can be used as a material for nanosensors and has a higher response speed to hydrogen at room temperature.

In recent years, with the deepening of research on these two surface states, researchers are no longer satisfied with the preparation of a single wettable surface, but are more concerned with how to achieve reversible regulation of surface wettability. The Fujishima research group [60] was the first to study the wetting characteristics of semiconductors. After studying  $\text{TiO}_2$ , it was found that ultraviolet light irradiation can

reduce the water contact angle (WCA) of the  $\text{TiO}_2$  surface from  $72^\circ$  to  $0^\circ$ . This caused  $\text{TiO}_2$  to exhibit superhydrophilic properties. This has aroused research interest in the variable wettability of the surfaces of wide bandgap inorganic semiconductor materials. At present, the method of achieving a change in the wettability of the material surface is mainly to change the external stimulus (such as light, temperature, acidity and alkalinity, etc.) to cause reversible changes in the chemical composition, spatial configuration or polarity of the surface active molecules of the material to achieve a change in wettability.

Chen et al. [61] obtained a responsive surface by modifying a rough gold surface with an alkyl mercaptan 2-benzoic acid using the interaction between the mercapto group and the metal atom. This surface exhibits a near-superhydrophobic state in low pH solutions, with a contact angle of  $144^\circ$ , and a superhydrophilic state in high pH solutions, with a contact angle approaching 0.

Sun et al. [62] used an atom transfer radical polymerisation method to graft a poly N-isopropylacrylamide film on a silicon wafer substrate, obtaining two surfaces with different wettabilities. The smooth silicon wafer substrate changed from a hydrophilic state ( $\text{CA} = 63.5^\circ$ ) to a hydrophobic state ( $\text{CA} = 93.2^\circ$ ) in the temperature range of  $25\text{--}40^\circ\text{C}$ . The principle of this research is that at temperatures below the LCST, the main intermolecular hydrogen bonds between the polymer chains and water molecules contribute to the hydrophilicity of the film; at temperatures above the LCST, the intramolecular hydrogen bonds between the  $\text{C}=\text{O}$  and  $\text{N-H}$  groups in the polymer chains make it difficult for the hydrophilic  $\text{C}=\text{O}$  and  $\text{N-H}$  to interact with water molecules, so the film exhibits hydrophilicity at high temperatures.

Feng et al. [63] synthesized  $\text{ZnO}$  nanorod array film via hydrothermal method. Under the induction of ultraviolet (UV) light, the  $\text{ZnO}$  nanorod film undergoes a significant surface wettability transition. The inorganic oxide film, which exhibits superhydrophobicity, becomes superhydrophilic under ultraviolet light. After the film is placed in the dark, the wettability returns to superhydrophobicity.

An effective and scalable strategy for fabricating superhydrophobic surfaces involves combining nanoparticles of various morphologies with polymer binders to form composite coatings with hierarchical surface textures. This approach exploits the synergistic effects of surface roughness - introduced by the nanoparticles - and the low surface energy imparted by the polymer matrix or subsequent surface treatment. Nanoparticles such as ZnO, SiO<sub>2</sub>, TiO<sub>2</sub>, or PTFE can be selected and synthesized in diverse shapes, including spheres, rods, flakes, or flower-like assemblies, each contributing distinct micro- and nano-scale features to the final surface morphology. When dispersed in a polymeric medium, these particles create a textured surface that mimics natural superhydrophobic structures, such as the lotus leaf.

One of the key advantages of this method lies in its tunability: by adjusting the ratio of nanoparticles to polymer, it is possible to regulate the surface texture and, consequently, the wetting behavior. A higher particle loading generally increases surface roughness and may reduce the contact area between water droplets and the solid surface, promoting the Cassie–Baxter wetting regime and lowering both the contact angle hysteresis and sliding angle. Conversely, a lower particle content can yield smoother surfaces with less pronounced hydrophobicity, or even revert the coating to a hydrophilic state. This balance between particle dispersion and matrix continuity enables fine control over the degree of water repellency and facilitates the design of coatings with tailored wetting performance for specific applications.

Moreover, this composite coating technology is highly compatible with conventional paint and coating processes, such as spray-coating, dip-coating, roll-to-roll application, or doctor blading. These scalable techniques make the production of superhydrophobic surfaces industrially feasible without the need for expensive equipment or vacuum systems. By incorporating readily available polymer resins and surface-functionalized nanoparticles into traditional formulations, manufacturers can integrate superhydrophobic functionality into protective, self-cleaning, or anti-corrosion coatings. This adaptability makes particle–polymer hybrid coatings a highly

promising platform for widespread commercial use in fields such as construction, transportation, electronics, and consumer goods.

An extensive work in direction of particulate based superhydrophobic coatings was done previously in Igor Sikorsky Kyiv Polytechnic Institute. In the paper [64] authors consider simple two-component coatings on acrylic polymer and different particulate materials – from calcite to nanoscale silica. It was shown that the latter one may provide contact angle values close to  $150^\circ$ . In [65] the wear resistance and in [66] UV and water resistance of such superhydrophobic coatings was characterized. It was shown that the Cassie-Baxter state is reached at certain ratio between polymer and the particles. And this ratio depends on the particle's specific surface and the surface energy. Therefore, using hydrophobized particles may decrease the required polymer quantity. The particle size reduction, contrary, increase the required polymer fraction.

#### *Problem of research statement*

Given the promising potential of superhydrophobic coatings and the unique advantages provided by the Cassie–Baxter wetting regime—such as extreme liquid repellency, resistance to contamination, self-cleaning ability, and enhanced anti-icing performance—there is a growing demand for scalable and effective fabrication methods. Although the scientific foundations for producing superhydrophobic surfaces using dispersed particles and polymer matrices are already well established, the specific use of zinc oxide (ZnO) nanoparticles as a structural component in such coatings remains underexplored. ZnO exhibits favorable properties including surface polarity, diverse morphologies, and compatibility with wet chemistry synthesis routes. However, the influence of ZnO particle shape, size, and concentration on the formation and performance of textured superhydrophobic polymer-based coatings has not been thoroughly studied. This gap defines the core problem of the present research: to investigate and optimize the use of ZnO nanoparticles of different morphologies within

polymer matrices for the creation of scalable, high-performance superhydrophobic coatings with tunable wetting properties.

**The purpose of the research:** The purpose of this study is to establish the connection between the structure and water repellency of organo-mineral surfaces.

**Objectives of the research:**

- to establish the basic principles of water repellency formation in organo-mineral textured systems;
- to obtain and characterize mineral disperse particles with different surface configuration/size;
- to study and tune the formation of water repellent ability of organo-mineral coatings;
- to demonstrate prospective use of obtained coatings;

**Research Object:** textured surfaces with tuned water repellency on the base of organic interface layer and mineral texture forming elements

**Research subject:** formation of water repellency of textures consisting of mineral structure formers and organic binding and interface layers.

*The results of the analysis of scientific literature conducted during the preparation of this section are presented in the following publications:*

1. Миронюк, О. В.; Баклан, Д. В.; Лі, Ч. Водовідштовхувальні тонкоплівкові полімерні композити з частинками червоного шламу як структуроутворювачами. *Technologies and Engineering* 2023, No. 3, 56–66. 10.30857/2786-5371.2023.3.6. ISSN 2786-5371, 2786-538X
2. Че, Л.; Білоусова, А.; Миронюк, О. Establishing the type of texture forming particles on hydrophobic properties of coatings. *Herald of Khmelnytskyi National University Technical Sciences* 2024, 333 (2), 155–161. [10.31891/2307-5732-2024-333-2-25](https://doi.org/10.31891/2307-5732-2024-333-2-25). ISSN 2307-5732

3. Li, C.; Myronyuk, O.; Bilousova, A.; Pitak, Y. Synthesis and characterization of Zn-based ceramic particles with controlled morphology. *Scientific Research on Refractories and Technical Ceramics* 2024, No. 124, 104–110. [10.35857/2663-3566.124.11](https://doi.org/10.35857/2663-3566.124.11). ISSN 2663-3566

## CHAPTER 2. Materials and methods

The experimental part of this work was aimed at developing and characterizing composite coatings with enhanced water-repellent properties, achieved through the integration of inorganic particles into a polymer matrix. The general research strategy was built on the premise that both surface chemistry and microstructure govern the wettability of solid surfaces. Therefore, the methodological approach combined material synthesis, composite formulation, and performance evaluation under controlled laboratory conditions.

The study began with the selection and characterization of key components: polymer binders with suitable film-forming and weather-resistant properties, and inorganic fillers—primarily zinc oxide—capable of forming rough, hierarchical textures on the coating surface. Particular attention was given to the synthesis of ZnO particles using sol-gel and precipitation methods, enabling the control of particle size, shape, and surface area.

Prepared particles were introduced into the polymer dispersion or solution to obtain composite systems with tailored microstructures. Coatings were applied onto substrates by conventional film-deposition techniques, such as casting or spraying, followed by drying and curing. Surface morphology and composition were studied using scanning electron microscopy (SEM) and FTIR spectroscopy, while the wetting behavior was evaluated by measuring static contact angles and sliding angles. This multi-step experimental framework was designed to systematically investigate the relationship between particle characteristics, coating microstructure, and water-repellent performance.

### 2.1 Reagents and materials

Sodium hydroxide (NaOH), analytical grade (Merck) - Table 2.1.

Table 2.1 - Properties of sodium hydroxide

| Property            | Value                |
|---------------------|----------------------|
| Molar mass          | 39.997 g/mol         |
| Melting point       | 318 °C               |
| Boiling point       | 1,388 °C             |
| Solubility in water | 111 g/100 mL (20 °C) |
| Appearance          | White solid          |

Zinc nitrate hexahydrate ( $\text{Zn}(\text{NO}_3)_2 \cdot 6\text{H}_2\text{O}$ ), analytical grade (Merck) - Table 2.2.

Table 2.2 - Properties of Zinc nitrate hexahydrate

| Property            | Value                       |
|---------------------|-----------------------------|
| Molar mass          | 297.49 g/mol                |
| Melting point       | 36.4 °C                     |
| Solubility in water | 184 g/100 mL (20 °C)        |
| Appearance          | Colorless crystalline solid |

Copper nitrate trihydrate ( $\text{Cu}(\text{NO}_3)_2 \cdot 3\text{H}_2\text{O}$ ), analytical grade (Alfa Aesar) - Table 2.3.

Table 2.3 - Properties of Copper nitrate trihydrate

| Property            | Value                  |
|---------------------|------------------------|
| Molar mass          | 241.60 g/mol           |
| Melting point       | 114.5 °C (decomposes)  |
| Solubility in water | 125 g/100 mL (20 °C)   |
| Appearance          | Blue crystalline solid |

Diammonium phosphate ( $(\text{NH}_4)_2\text{HPO}_4$ ), analytical grade (Merck) - Table 2.4.

Table 2.4 - Properties of Diammonium phosphate

| Property            | Value                    |
|---------------------|--------------------------|
| Molar mass          | 132.06 g/mol             |
| Melting point       | 155 °C (decomposes)      |
| Solubility in water | 58 g/100 mL (25 °C)      |
| Appearance          | White crystalline powder |

Titanium dioxide (TiO<sub>2</sub>, P25), analytical grade (Evonik) - Table 2.5.

Table 2.5 - Properties of Titanium dioxide

| Property              | Value                   |
|-----------------------|-------------------------|
| Average particle size | ~21 nm                  |
| Crystal structure     | 80% anatase, 20% rutile |
| BET surface area      | ~50 m <sup>2</sup> /g   |
| Appearance            | White powder            |

Silica (Sipernat D 17 SiO<sub>2</sub>, Evonik, median particle diameter approx. 14 µm), analytical grade (Evonik) - Table 2.6.

Table 2.6 - Properties of Silica

| Property         | Value                 |
|------------------|-----------------------|
| Particle size    | ~14 µm                |
| Purity           | >99.8%                |
| BET surface area | 200 m <sup>2</sup> /g |
| Appearance       | White powder          |

Ammonia (NH<sub>3</sub>·H<sub>2</sub>O), analytical grade (Himlaborreaktiv, Kyiv) - Table 2.7.

Table 2.7 - Properties of Ammonia

| Property                      | Value                              |
|-------------------------------|------------------------------------|
| NH <sub>3</sub> concentration | 25–30%                             |
| Density                       | ~0.91 g/cm <sup>3</sup>            |
| Boiling point                 | ~37.7 °C (for solution)            |
| Appearance                    | Colorless liquid with pungent odor |

Deionised water (DI water) (Laboratory-produced) - Table 2.8.

Table 2.8 - Properties of Deionised water

| Property     | Value                   |
|--------------|-------------------------|
| Resistivity  | 18.2 MΩ·cm at 25 °C     |
| pH           | 5.5–7                   |
| Conductivity | <1 μS/cm                |
| Appearance   | Clear, colorless liquid |

Tetraethyl orthosilicate (TEOS), analytical grade (Sigma-Aldrich) - Table 2.9.

Table 2.9 - Properties of Tetraethyl orthosilicate

| Property      | Value                   |
|---------------|-------------------------|
| Molar mass    | 208.33 g/mol            |
| Boiling point | 168–170 °C              |
| Density       | 0.933 g/cm <sup>3</sup> |
| Appearance    | Colorless liquid        |

Isopropanol (IPA), analytical grade (Himlaborreaktiv, Kyiv) - Table 2.10.

Table 2.10 - Properties of Isopropanol

| Property      | Value                   |
|---------------|-------------------------|
| Molar mass    | 60.10 g/mol             |
| Boiling point | 82.6 °C                 |
| Density       | 0.786 g/cm <sup>3</sup> |
| Appearance    | Clear, colorless liquid |

Polymer resin (styrene-butyl methacrylate; Neocryl B 880), analytical grade (Covestro Resins) - Table 2.11 and Fig.2.1.

Table 2.11 - Properties of Polymer resin

| Property   | Value |
|--|-------|
| Average molecular weight                           | 90000 |
| Acid value (mg KOH)                                | 6     |
| Glass transition temperature (T <sub>g</sub> ), °C | 52    |
| Softening temperature, °C                          | 135   |
| Density, g/cm <sup>3</sup>                         | 1,07  |

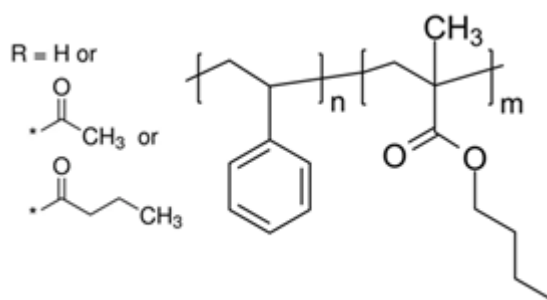


Figure 2.1. Structure of isobutyl methacrylate polymer **NeoCryl B-880**

p-Xylene (PX), analytical grade (Himlaborreaktiv, Kyiv) - Table 2.12.

Table 2.12 - Properties of p-Xylene

| Property      | Value                               |
|---------------|-------------------------------------|
| Molar mass    | 106.17 g/mol                        |
| Boiling point | 138.4 °C                            |
| Density       | 0.861 g/cm <sup>3</sup>             |
| Appearance    | Colorless liquid with aromatic odor |

All reagents were used without further purification.

## 2.2 Preparation of ZnO and its composites via precipitation method

Flower-like ZnO particles were synthesized using a simple one-step synthesis method [67]. The method contains the following stages: dissolve  $\text{Zn}(\text{NO}_3)_2$  in a beaker with deionised water, then transfer the beaker to a magnetic stirrer and stir for 30

minutes. The solution is referred to as A. Weigh a certain amount of NaOH, dissolve the NaOH completely in deionised water, and weigh B. Slowly add solution B to solution A while stirring for 2 hours. After the reaction, the beaker was placed in an incubator at 80°C for 5 hours. The suspension was centrifuged to obtain a precipitate, which was washed three times with deionised water and anhydrous ethanol, respectively, and transferred to an 80°C drying oven for 5 hours. Finally, the dried particles were placed in a muffle furnace at 500°C for 2 hours. Grinding was used to obtain ZnO particles.

Mix 0.5 g of ZnO in 30 mL of IPA for 30 minutes to obtain a homogeneous solution, which is referred to as solution A. Mix 2.5 g of TEOS with 20 mL of IPA to obtain solution B. The B solution was slowly added dropwise to the A solution while adding ammonia to maintain a pH of 8.5-9.5. The mixture was stirred for 1 h and aged at 80 °C for 6 h. The resulting solid was filtered, washed three times with deionised water and IPA, and dried. Finally, it was treated in a muffle furnace at 500 °C. Grinding the resulting product gave ZnO-SiO<sub>2</sub> composite particles.

#### Preparation of ZnO particles (NaOH)

First, a 0.1 mol/L Zn(NO<sub>3</sub>)<sub>2</sub>·6H<sub>2</sub>O solution (denoted as solution A) was added. Under magnetic stirring, a 5 M NaOH solution was slowly added to solution A, and the mixture was stirred for 30 min. The resulting mixture was transferred to a stainless steel reactor lined with polytetrafluoroethylene and heated under water at 150 °C for 6 h. After the reaction, the mixture was allowed to cool naturally to the first step, and the product was washed three times with deionized water and dried. Finally, the dried sample was dried in a muffle furnace at 400°C for 1 h to obtain ZnO particles.

Preparation of ZnO particles (NH<sub>3</sub>·H<sub>2</sub>O) represents a 0.1 mol/L Zn(NO<sub>3</sub>)<sub>2</sub>·6H<sub>2</sub>O solution A. The NH<sub>3</sub>·H<sub>2</sub>O solution was slowly added dropwise to solution A, and the pH of the solution was maintained at 8-9. The mixture was stirred magnetically for 30

min, transferred to a reaction vessel, and heated to 80 °C and 150 °C for 6 h. After cooling naturally, the mixture was washed three times and placed in a muffle furnace and burned at 400 °C in phosphoric acid for 1 h. ZnO particles were obtained.

#### Preparation of ZnO-TiO<sub>2</sub> nanocomposite

P25 (0.5 g) was mixed with a 0.1 mol/L Zn(NO<sub>3</sub>)<sub>2</sub>·6H<sub>2</sub>O solution (7.5 g), and the mixture was stirred for 30 min. Then, a 5 M NaOH solution was slowly added dropwise to the above mixture, and the mixture was stirred for another 10 min after the addition was complete. The resulting mixture was transferred to a high-pressure reactor lined with polytetrafluoroethylene and reacted under water at 150 °C for 6 h. After the reaction was completed, it was allowed to cool naturally to room temperature, washed three times with deionised water, preheated at 60 °C, and calcined at 400 °C for 1 h to obtain the ZnO–TiO<sub>2</sub> nanocomposite.

#### Preparation of ZnO-SiO<sub>2</sub> nanocomposite

SiO<sub>2</sub> (0.3 g, Evonik, median particle size of about 14 µm) and 0.1 mol/L Zn(NO<sub>3</sub>)<sub>2</sub>·6H<sub>2</sub>O solution (7.5 g) were weighed and mixed, and the mixture was stirred for 30 min. Then, 5 M NaOH solution was slowly added dropwise, and the mixture was stirred for another 10 min after the addition was complete. The resulting mixture was transferred to a stainless steel reactor lined with polytetrafluoroethylene and reacted at 150 °C for 6 h. After cooling naturally, the product was washed three times with deionized water, allowed to sleep at 60 °C, and oxidized and burned at 400 °C for 1 h to obtain ZnO–SiO<sub>2</sub> nanocomposite particles.

#### Preparation of ZnO-TiO<sub>2</sub> nanocomposites with different molar ratios

To study the effect of different Zn:Ti molar ratios on the structure and properties of the composite material, TiO<sub>2</sub> (P25) and 0.1 mol/L Zn(NO<sub>3</sub>)<sub>2</sub>·6H<sub>2</sub>O solution were

weighed and mixed in the ratios of Zn:Ti = 2:1, 4:1, 10:1, etc. After stirring the mixture for 30 minutes, 5M NaOH solution was slowly added, and then stirred for another 10 minutes. The resulting dispersion was transferred to a high-pressure reactor lined with polytetrafluoroethylene and reacted under water at 150 ° C for 6 hours. After the reaction, it was allowed to cool naturally to step. The product was washed three times with deionized water, dried at 60 ° C, and calcined at 400 ° C for 1 hour to obtain ZnO–Ti nanocomposites with different molar ratios were obtained.

### 2.3. Preparation of organo-mineral coatings

To prepare composite coating formulations, a solution was first obtained by combining the polymer resin and p-xylene solvent at a mass ratio of 1:5. The mixture was stirred continuously until a homogeneous and fully transparent solution was formed, indicating the complete dissolution of the resin in the solvent. This step ensured uniform distribution of the polymer chains and established a suitable medium for the subsequent dispersion of particulate additives.

Following dissolution, various inorganic fillers—namely silicon dioxide (SiO<sub>2</sub>), titanium dioxide (TiO<sub>2</sub>), zinc oxide (ZnO), and composite ZnO–SiO<sub>2</sub> particles—were introduced into the polymer solution. The fillers were added in predetermined mass fractions, denoted as X<sub>1</sub> wt%, X<sub>2</sub> wt%, X<sub>3</sub> wt%, and X<sub>4</sub> wt%, respectively. The selected ranges for each additive were as follows: SiO<sub>2</sub> (X<sub>1</sub>) from 0 to 40 wt%, TiO<sub>2</sub> (X<sub>2</sub>) from 20 to 95 wt%, ZnO (X<sub>3</sub>) from 20 to 80 wt%, while ZnO–SiO<sub>2</sub> composite particles were incorporated based on comparative formulations and served to evaluate synergistic effects in texture formation and surface functionality.

After the addition of fillers, the mixture was subjected to continuous mechanical stirring to ensure thorough dispersion of the particles throughout the resin solution. This step was critical to prevent agglomeration and to promote uniform surface texture in the final coating.

The resulting suspension was then applied onto clean glass substrates using a uniform film-casting technique. The substrates were standard microscope glass slides with

dimensions of 2.5 cm × 1.0 cm × 0.02 cm. Each coating was spread evenly across the surface to ensure consistent thickness and texture formation.

Finally, the coated glass slides were placed in a controlled thermal environment and dried at a temperature of 55 °C for 10 minutes. This drying process facilitated solvent evaporation and film solidification, yielding a dry composite coating ready for subsequent characterization.

## 2.4. Instrumental methods of characterization

### *Scanning electron microscope (SEM)*

The scanning electron microscope is the most commonly used instrument for studying nanomaterials. It mainly consists of an electron gun and a cathode emitting an electron beam. Under the action of the accelerating voltage between the anode and cathode, the electron beam is shot towards the lens tube, focused by a set of magnetic lenses, and then focused again by a set of scanning coils controlling the electron beam, and finally focused by an objective lens to hit the sample. In response to the sample, a series of signals are generated, such as secondary electrons, backscattered electrons and X-rays. Secondary electron signal absorption, backscattered electron signal absorption or X-ray energy spectrometer are equipped on the upper side of the sample as needed to distinguish these signals. These signals are detected by the corresponding detectors, amplified, converted, and turned into voltage signals, which are finally transmitted to the kinescope to display various information. The sample preparation methods also differ for different types of samples. For conductive materials (such as metals), as long as a sample of the right size is made, it can be tested directly. For non-conductive materials or materials with poor electrical conductivity (such as fibres, ZnO, SiO<sub>2</sub>, etc.), an electric charge tower will be generated under the action of the electron beam, which will affect the movement record of the electron beam spot and the emitted secondary electrons, thus reducing the image quality. Therefore, in addition to being

made into a suitable size, a conductive layer needs to be deposited on the surface of the sample before observation. Gold, silver or carbon films with high secondary electron emission rates are usually used as conductive layers. In this study we used JSM-6700F field emission scanning electron microscope (FESEM) in secondary electron mode at 15 kV.

*Transmission electron microscope (TEM)* crystal electron stand is a high-resolution, high-power crystal that can provide information on the tissue structure, crystal structure and chemical composition of fine materials. It is an important means of material science research. It is composed of five parts: the illumination system, the electromagnetic lens imaging system, the vacuum system, the recording system, and the power supply system. A high-energy electron beam generated by an electron gun is focused by an electron converging lens, and a concave lens forms an image that is then focused and amplified by an electromagnetic lens. The electron beam passing through the lens passes through an objective lens, where a high-quality magnified lens-shaped image is obtained on the image plane, and then magnified a second time by an intermediate lens and a projection lens to form a final three-stage magnified image that is displayed on a fluorescent screen. Since electrons are easily focused or absorbed by objects, the imaging power is relatively low, so there are strict requirements for sample preparation.

The lattice structure and lattice fringes of the prepared sample were characterised using a JEM-2010F model electron microscope at an accelerating voltage of 200 kV.

*X-ray diffraction (XRD)* analysis is a routine means of identifying the crystal structure of a substance and performing phase analysis, and is widely used. The main characteristic of crystalline materials is the periodic arrangement of atoms in the crystal lattice. When a parallel beam of X-rays strikes a crystal in a substance with regularly arranged atoms, the electrons in the atoms are excited to vibrate and become a source

of secondary X-rays. Each atom radiates scattered waves with a wavelength equal to the predicted X-ray wavelength in all directions in space, but only in certain directions, where the optical path difference is an integer multiple of the X-ray wavelength, can the capacitance be enhanced and a conductive peak be formed. In other directions, it is split or changed. In this thesis, the crystal structure of the sample was characterised using X-ray diffraction (XRD; Rigaku, RINT2000, CuK $\alpha$  emission line  $\lambda = 0.15418$  nm).

*X-ray photoelectron spectroscopy (XPS)* is a widely used surface analysis technique that is mainly used to determine the elemental composition and chemical state of the surface as well as the electron density around the atoms in molecules, in particular the atomic valence state and the electronic cloud and energy level structure of surface atoms. X-ray photoelectron spectroscopy is a type of electron spectroscopy based on the photoelectric effect. It uses X-ray photons to excite the inner electrons of atoms on the surface of a material. The energy of these electrons is analysed by XPS. XPS is a physical method, and in most cases the sample is not delaminated by X-rays, It is therefore a non-destructive analysis method. The sample is generally cleaned chemically before analysis. It can analyse a wide range of elements and in principle can analyse all elements except hydrogen. It is very similar to ultra-trace analysis, and can analyse samples of about  $10^{-6}$ g. The surface composition of the samples, including the chemical states of the elements, was characterized using ESCALAB MK II equipment.

*Diffuse reflectance spectroscopy (DRS)* is a valuable analytical technique used for the optical characterization of powdered solids, coatings, and other diffusely scattering materials. In this research, DRS was employed to analyze the light absorption and reflectance properties of composite coatings containing inorganic fillers such as SiO<sub>2</sub>, TiO<sub>2</sub>, and ZnO. This method enables the assessment of optical band gaps, surface composition, and the presence of light-absorbing species in non-transparent materials without requiring complex sample preparation.

The technique is based on the measurement of radiation diffusely reflected from the surface of a sample when illuminated by a monochromatic or polychromatic light source. Unlike specular reflectance, which is associated with smooth, mirror-like surfaces, diffuse reflectance occurs when the incident light is scattered in many directions due to surface roughness or internal scattering centers within the material. This scattered light is collected and analyzed to extract spectroscopic information.

Measurements were carried out using a UV-Vis spectrophotometer equipped with an integrating sphere accessory, which captures the diffusely reflected light over a wide angular range. The spectra were recorded over the wavelength range of 200–800 nm. Prior to each measurement, a baseline correction was performed using a standard reference material with known high reflectance, typically barium sulfate ( $\text{BaSO}_4$ ), to ensure accuracy and reproducibility.

The obtained reflectance data  $R$  were transformed into pseudo-absorption spectra using the Kubelka–Munk function:

$$F(R) = (1 - R)^2 / 2R \quad (4)$$

where  $F(R)$  is proportional to the absorption coefficient for strongly scattering samples. This transformation enables the application of Tauc plots for band gap estimation, particularly relevant for characterizing semiconductor fillers like  $\text{TiO}_2$  and  $\text{ZnO}$ .

DRS provides a non-destructive, rapid, and reliable approach to monitoring optical transitions and evaluating surface properties of complex coatings. In the context of this study, it contributed to understanding how different particulate compositions and morphologies influence the optical behavior and light-interaction mechanisms of the developed superhydrophobic coatings.

The ultraviolet-visible diffuse reflectance spectroscopy (UV-vis/DRS) of the prepared material was measured using a UV-2450 spectrophotometer from Tsukuba.

### *Photoluminescence (PL)*

Photoluminescence (PL) spectroscopy is a non-destructive optical technique that provides insights into the electronic structure, surface defects, and recombination mechanisms of semiconducting and luminescent materials. In this study, PL analysis was conducted to evaluate the optical emission characteristics of coatings containing oxide-based fillers, specifically focusing on zinc oxide (ZnO) and titanium dioxide (TiO<sub>2</sub>), as these materials exhibit strong excitonic and defect-related luminescence under ultraviolet excitation.

The PL measurements were carried out using a Hitachi F-4500 fluorescence spectrometer equipped with a xenon lamp as the excitation source. The excitation wavelength was set at 300 nm to effectively stimulate the intrinsic and defect-related luminescent centers in the inorganic phases of the composite coatings. Samples were positioned perpendicular to the excitation beam, and the emission spectra were recorded in the range of 350–700 nm.

This technique is particularly sensitive to surface and interface defects, such as oxygen vacancies, interstitial atoms, and surface adsorbates, which significantly affect the luminescence behavior of oxide particles. The resulting spectra were analyzed to identify emission peaks corresponding to near-band-edge (NBE) and deep-level emissions (DLE), which serve as indicators of material purity, crystallinity, and surface states.

### *Water contact angle (WCA) determination*

The static water contact angle of the coating was determined using the pendant drop method. The glass slide was placed directly below the syringe, and the contact angle test was performed after adjusting the glass slide to be flush (the water droplet was 5  $\mu$ L when testing the water contact angle). During this process, 3-5 different positions were selected for measurement. The shape of the fixture was observed using an electron microscope, and the angle between the fixture and the glass slide surface was measured. The fixture was used as the final test result. The equipment used was

Konus Accademy microscope with goniometry unit and HDCE 50H camera integrated with Scope Photo software.

To ensure the reliability and reproducibility of the wettability data, statistical analysis was performed on the measured static water contact angles (WCAs). For each coating formulation, at least five independent measurements were conducted on different surface locations. The resulting values were analyzed using OriginPro software (OriginLab Corporation), which allowed for comprehensive visualization and statistical evaluation of the data.

Descriptive statistics including mean, standard deviation, and coefficient of variation were calculated for each sample group. These metrics enabled the assessment of the consistency of the surface wetting behavior and helped identify potential heterogeneities in the coating texture. Box-and-whisker plots were generated to illustrate the data distribution and highlight the presence of outliers.

In addition, one-way analysis of variance (ANOVA) was employed to determine the statistical significance of differences between multiple sample groups with varying particle content or composition. A significance level of  $p < 0.05$  was considered indicative of meaningful differences in wettability. Where applicable, post hoc Tukey's tests were conducted to identify specific pairs of groups with statistically significant differences.

This statistical approach provided a robust basis for evaluating the influence of surface composition, filler morphology, and formulation parameters on the hydrophobic performance of the coatings. The combined use of experimental measurements and statistical analysis enhanced the scientific validity of the conclusions drawn from the contact angle data.

### *FTIR spectroscopy*

Fourier-transform infrared (FTIR) spectroscopy was used in this research to investigate the chemical structure of the materials involved, including polymer matrices, inorganic fillers, and hybrid organo-mineral composites. Two types of

spectrometers were utilized: the Specord IR-75 (Analytik Jena) operated in transmission mode and the Thermo Nicolet Nexus 4700, which was equipped with an Attenuated Total Reflectance (ATR) accessory. This combination of methods allowed for the analysis of a wide range of chemical bonds and surface functional groups across different types of samples.

For micro- and nanoscale particulate materials such as ZnO and ZnO–SiO<sub>2</sub> composites, the transmission spectra were acquired using the standard KBr pellet method. The sample and spectroscopic grade potassium bromide were combined at a mass ratio of 1:40 (sample:carrier) and thoroughly homogenized using an automated ball mill. The resulting mixture was pressed into transparent pellets using a hydraulic press under a pressure of 0.6–0.8 MPa. This technique enabled high-quality spectra in the mid-infrared region, particularly in the fingerprint zone below 1000 cm<sup>-1</sup>, where metal–oxygen vibrations can be detected.

For analysis of the polymer matrix and hybrid composite coatings, thin films were cast from solution onto infrared-transparent windows such as KBr and KRS-5 using the doctor blade technique. The formulations included styrene–acrylate resins combined with inorganic fillers and were homogenized using a high-speed bead mill (IKA UltraTurrax) to ensure uniform dispersion. After solvent evaporation, the resulting dry films were subjected to FTIR analysis in ATR mode to obtain surface-sensitive information and assess the chemical integrity of the coatings.

The FTIR spectra were recorded over a scanning range of 400–4000 cm<sup>-1</sup>. Characteristic absorption bands of ZnO particles, including Zn–O stretching vibrations, were typically observed near 500 cm<sup>-1</sup>. Additional bands were analyzed to confirm the presence of hydroxyl groups, surface carbonates, and organic residues from surface modification processes. For the styrene–acrylate matrix, peaks corresponding to ester carbonyl groups (~1730 cm<sup>-1</sup>), aliphatic and aromatic C–H stretches (2800–3100 cm<sup>-1</sup>), and C=C aromatic ring vibrations (~1600 cm<sup>-1</sup>) were used to verify structural features. Comparative analysis allowed for evaluation of filler–matrix interactions,

chemical stability, and the impact of various additives on the overall chemical composition of the coating systems.

### **CHAPTER 3. Water repellent coatings on the basis of red mud**

At this stage, the technology of water-repellent coatings is in a state of development and is quite far from large-scale implementation due to a number of limitations, including scaling difficulties, high cost of obtaining such structures and their rather low stability under atmospheric conditions [68]. The scaling problem can be solved using existing industrial practices for applying organo-mineral coatings, and the cost problem for large-scale hydrophobic surfaces can be solved by using waste particles such as particles responsible for texture formation [69, 70]. An obstacle to this solution is the rather high chemical activity of this waste and the presence of water-soluble components, which, however, can be overcome in a number of ways – inactivation with acid gases or the same waste, the hydrothermal method [71–74], and as well as high temperature annealing. The latter method, as shown in [72], makes it possible to incorporate recycled waste into the composition of building materials, since the resulting particles turn out to be quite chemically inert. Taking into account the possibility of average particle size control by usual for filler industry grinding and the following classification, the desired granulometry may be provided. The relatively inactive surface after sintering may be a good candidate for the microstructure formation, similar to that was illustrated in [73]. This chapter is aimed to demonstrate the possibility of manufacturing thin-layer water-repellent coatings based on red mud particles.

The red mud was used was obtained from PJSC "Zaporozhye aluminum plant" as an industrial waste generated during the processing of bauxite ore. The deactivation process was carried out in a muffle furnace at a temperature of 950 °C in order to lower the particles surface activity. Grinding was carried out in a handled mortar for 20 minutes. Next, the crushed red mud powder was sieved through a sieve with a pore diameter of 63 microns. For the creation of superhydrophobic coatings it is better practice to use pre-treated particles with reduced surface energy. This may be obtained

by the hydrophobization of initially hydrophilic surface, that is formed in the annealing and crushing processes.

Hydrophobization of red mud was carried out with the following modifiers: stearic acid, Methyltriethoxysilane (MTES), Octyltriethoxysilane (OCTEO). MTES and OCTEO are possible options for replacing fluorine-containing water repellents to improve environmental friendliness [74]. The modification was made by immersing red mud samples in an isopropyl alcohol MTES/OCTEO solution (1 wt. %) for 30 min at a temperature of 20–25 °C. And then the material was dried in an oven at 130 °C for 1 hour [75]. Modification with stearic acid was carried out in 3 wt. % solution in isopropyl alcohol, after 60 minutes of exposure, the red mud was washed and dried in an oven at a temperature of 60 °C [76].

To create the compositions, a styrene-acrylate binder (NeoCryl B-880, DSM coating resins) was used. The film forming polymer was dissolved in xylene. And the modified red mud filler was introduced in the specified amounts into the said solution upon mixing.

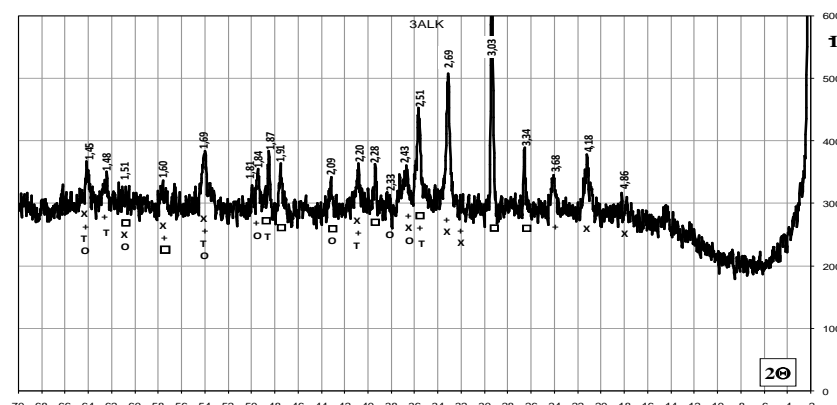
A FRITSCH Analysette 22 laser particle analyzer was used to obtain particle size data. An optical microscope and a digital camera (Delta Optical HCDE-50) were used to obtain photographs of the surface of the samples. To confirm the red mud modification, IR spectroscopy (Specord IR 75, in the wavenumber range from 400 to 4000 cm<sup>-1</sup>) was used using KBr tablets as an inert carrier. The contact angles were measured by the sessile drop technique, using a digital goniometer, using a digital camera (Delta Optical HCDE-50, China) and the corresponding software (ScopeTek View). For statistical processing, a minimum of 5 measurements were made for each sample. To determine the contact angles, the technique described in [77] was applied, which is based on the Washburn thin-walled capillary impregnation technique. Wetting time was recorded using a digital video camera with an accuracy of 0.16 s. The number of time measurements for each solvent was 5 times.

It has been established that the pH of the water extract of the initial red mud is 11–12 close to reported in [78], while that of the annealed mud is reduced to 7, which can be explained by the binding of low-temperature alkaline sodium salts to the corresponding oxide (Table 3.1) in the composition of amorphous ceramics. The presence of a set of oxides of alkali and alkaline earth metals, however, causes the expected high polarity of the surface of the annealed material [79].

Table 3.1 - Chemical composition of the red mud

| Content, %       |                                |                                |                  |     |     |                   |         |
|------------------|--------------------------------|--------------------------------|------------------|-----|-----|-------------------|---------|
| SiO <sub>2</sub> | Al <sub>2</sub> O <sub>3</sub> | Fe <sub>2</sub> O <sub>3</sub> | TiO <sub>2</sub> | CaO | MgO | Na <sub>2</sub> O | Residue |
| 7,2              | 16,7                           | 50,6                           | 5,6              | 6,1 | 0,3 | 2,2               | 11,3    |

The analysis of mineralogical composition by X-ray diffraction (Fig.3.1) shows that this probe of the red mud contains a set of minerals on the basis of said oxides.



°C, the structure of primary particles changes insignificantly, and further grinding and sieving makes it possible to separate a fine submicron fraction.

Additional fine fraction in the treated sample in comparison to the neat one may be also seen at optical microscopy images (Fig. 3.3). The coarser particles after sieving may be mainly considered as the secondary ones, formed due the moisture aggregation. Considering them as aggregates, they even in this form may be beneficial in constructing hierarchial structures for enhanced water repellency.

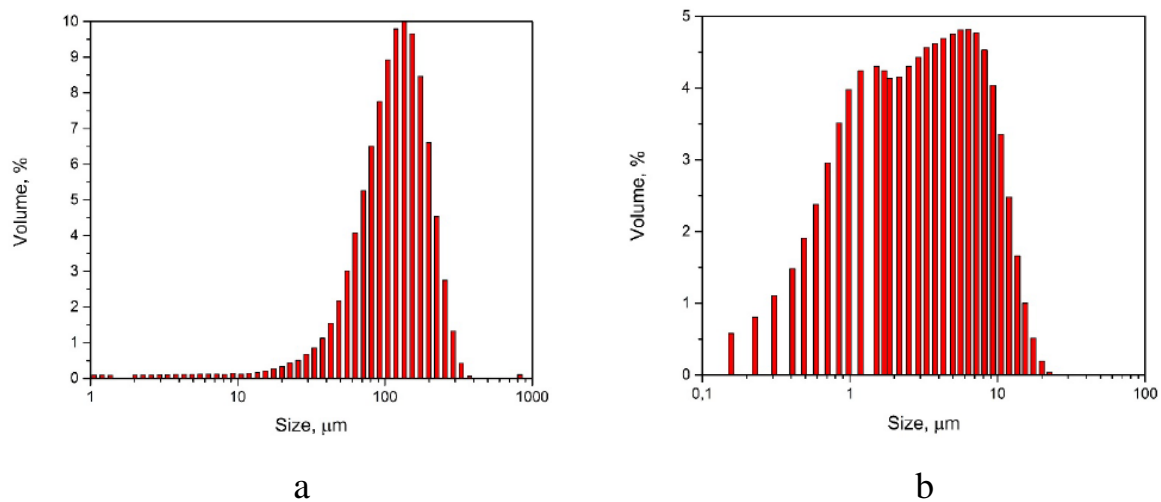


Figure 3.2. Particle size distribution of untreated (a) and sintered at 950 °C and sieved (b) red mud

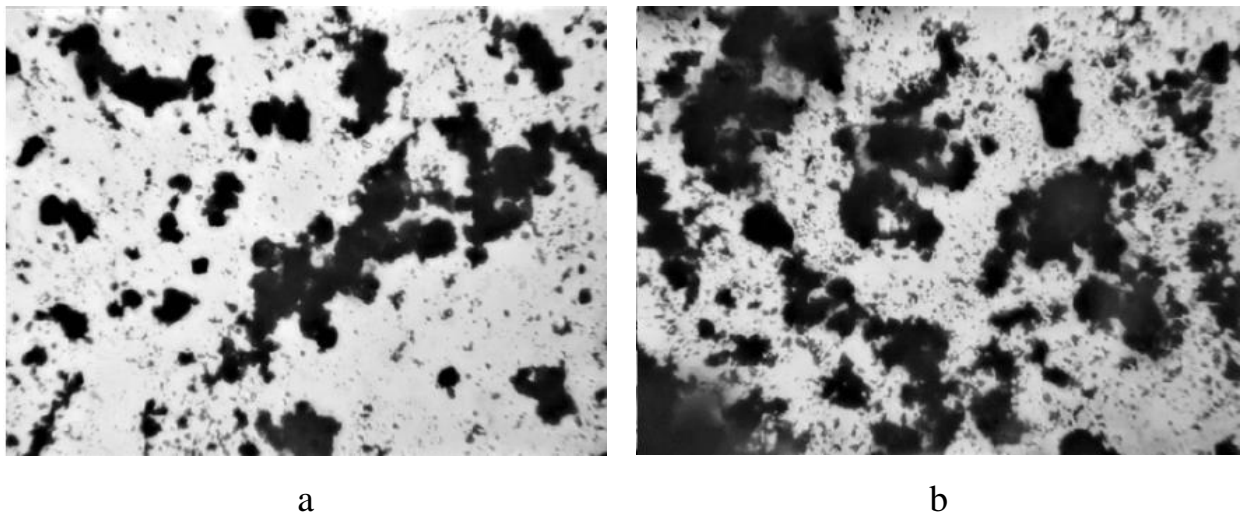


Figure 3.3 Optical microscopy photo of untreated (a) and sintered at 950 °C and sieved (b) red mud

In addition to the structural features of the surface textures of water-repellent coatings, the determining factor for the stability of the Cassie state is the intrinsic contact angle of the surface, which follows from the corresponding equation (1):

$$\cos\theta_{\text{app}} = f_1\cos\theta_1 + f_2\cos\theta_2, \quad (5)$$

where  $\cos\theta_{\text{app}}$  is the contact angle of a two-phase heterogenous surface,  $f_1$  and  $\cos\theta_1$  are the surface fraction and the contact angle of the first phase,  $f_2$  and  $\cos\theta_2$  are the surface fraction and the contact angle of the second phase (an air).

The texture, that is formed due to incorporation of disperse particles into the coating is responsible for  $f_1$  and  $f_2$  values. But  $\cos\theta_1$  is determined by the own surface energy of the material. This fact makes the decrease of the surface polarity of the red mud particles to be necessary.

The contact angle of the surface of particles of the initial red mud with water is  $53\pm3^\circ$ , and after annealing at  $950^\circ\text{C}$  it increases to  $55\pm3^\circ$ . The difference between the values is within the measurement error, which indicates the proximity of the polar components of their surface. This result is not surprising, since ceramic materials consisting of metal oxides are characterized by the presence of pronounced acidic and basic components of surface interactions [80]. After the treatment of the materials with stearic acid, OCTEO and MTES to reduce polarity, they were characterized with infrared spectroscopy.

In the infrared spectrum (Fig. 3.4 a) of untreated red mud, there is a peak at  $3470\text{ cm}^{-1}$ , which corresponds to  $-\text{OH}$  groups, which are absent in materials after thermal treatment, which can be explained by a decrease in the proportion of hygroscopically bound water due to the binding of soluble salts during annealing [81]. On Fig. 3.4 c peaks at  $2903\text{ cm}^{-1}$  and  $2836\text{ cm}^{-1}$  indicate the presence of symmetric and asymmetric C–H vibrations, which are evidence of the presence of a large amount of stearic acid

on the surface of the red mud [82]. All IR spectra of the original, after treatment, and modified red mud at 530–570  $\text{cm}^{-1}$  contain peaks of high intensity, which corresponds to the Si–O–Si bond [83]. The infrared spectra of the red mud treated with OCTEO and MTES do not differ significantly from the unmodified red mud after heat treatment, which indicates a low amount of adsorbed silane modifiers.

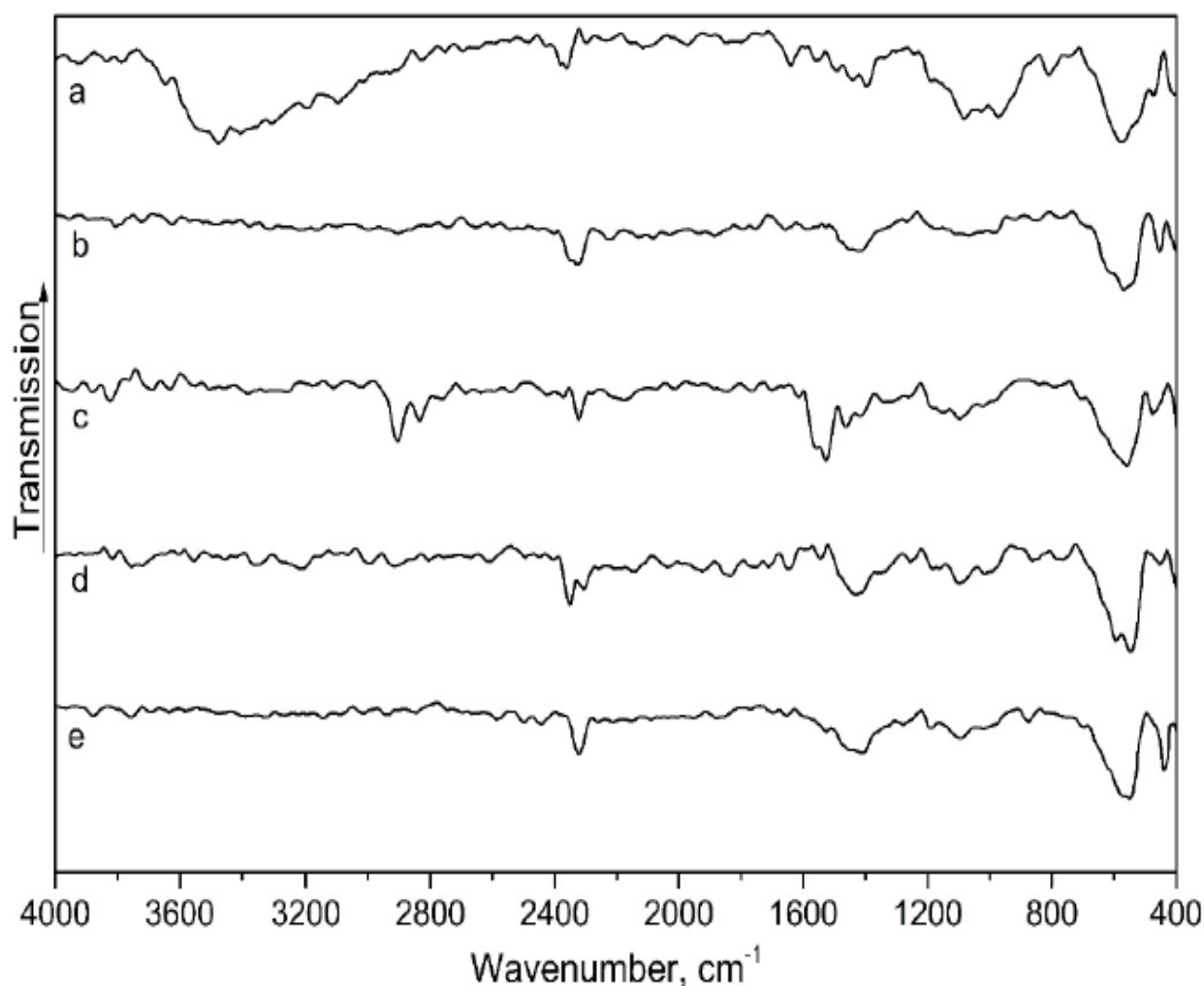


Figure 3.4. Infrared spectra of pristine (a), annealed at 950 °C (b), stearic acid modified (c), MTES modified (d) and OCTEO modified (e) red mud

It has been established that all water repellents used are effective and allow reaching the contact angle values of initially hydrophilic red mud particles above 90° (Fig. 3.5). It is interesting that the largest values of the contact angle – up to 136° are achieved when the red mud is modified with stearic acid, which can be explained by the large amount of the layer of this water repellent compared to silane ones. However,

the water repellent OCTEO approaches it in terms of its effectiveness. It is on his example that one can clearly see the difference in the efficiency of hydrophobization of annealed and unannealed red mud.

In order to form textured surfaces, a number of compositions were obtained, in which the content of the film-forming agent that binds the particles on the surface varied. It should be clarified that the intrinsic contact angle of the styrene-acrylic polymer is  $85^\circ$ , that is, it is quite close to the hydrophobic state.

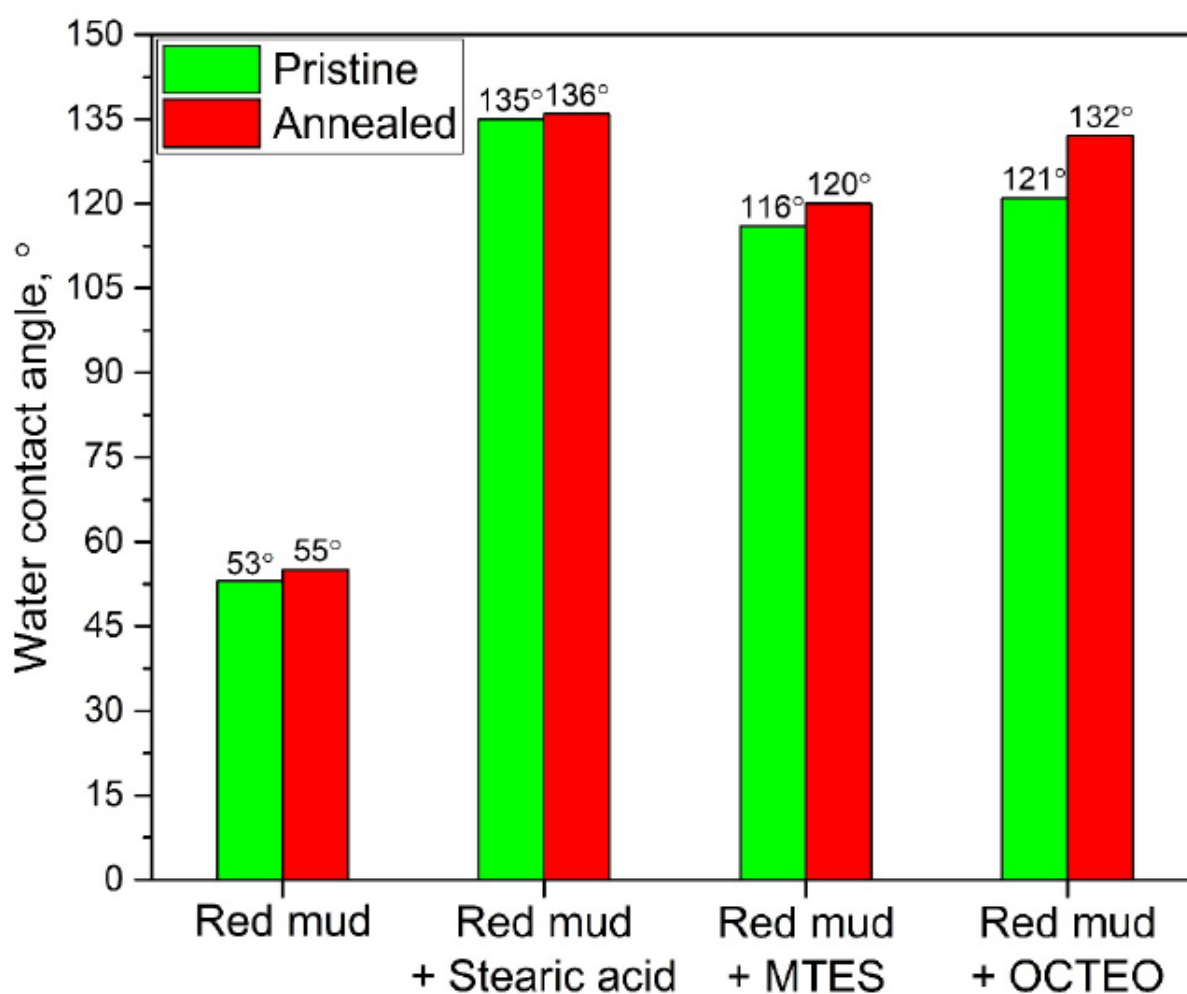


Figure 3.5. Water contact angles of red mud particles with different surface treatment

The surface of the coatings obtained by the layer coating method based on red mud and polymer is mostly heterogeneous. Areas with different wetting properties are present at all the samples. Some fractions of the surfaces are suffering from the the film former depletion, while others, on the contrary, are enriched (Fig. 3.6).

In the Fig. 3.6 a we can see the surface of just-annealed and sieved red mud without the film forming agent. And Fig. 3.6 b is chemically treated red mud. In the schematic representative model at the Fig. 3.6. the red mud particles are shown as red circles, the layer of chemical modifier molecules – yellow circle and the film forming agent (polymer) is of blue color.

Conventionally, according to the wetting properties, the sections of the compositions with the polymer can be described within three types. Type “C” (Fig. 3.6 c) is characterized by the presence of a minimum amount of polymer, which only allows the red mud particles to be bonded together. This type corresponds to high porosity and development of the surface structure.

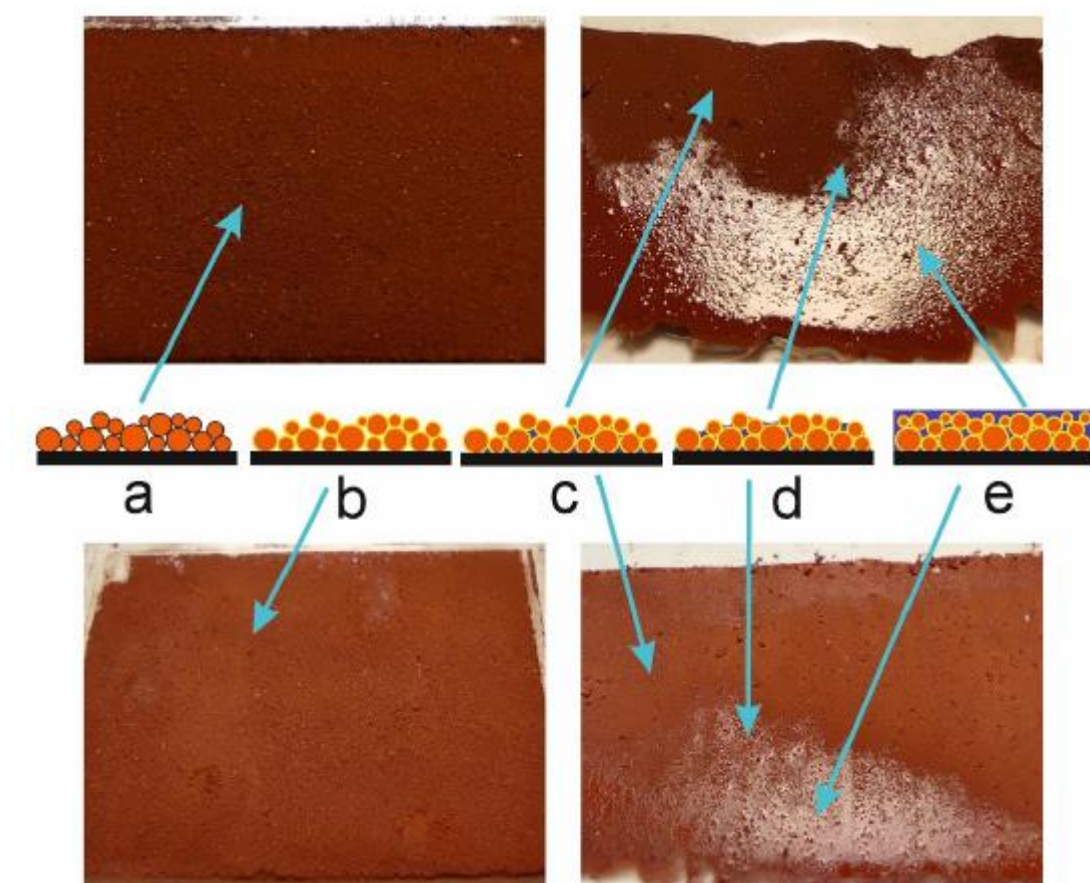


Figure 3.6. Thin film composites of red mud and acrylic polymer

Type “D” (Fig. 3.6 d) contains more polymer in its structure, which allows more filling of voids between the particles, however, the surface is still quite rough and

matte. Type “E” (Fig. 3.6 e) is characterized by a sufficient amount of polymer to completely cover the red mud particles.

Unannealed red mud particles without polymer give a water contact angle of  $53^\circ$ , while already with polymer the angle is  $131^\circ$ , with a filler content of 95%. A similar picture is observed with annealed red mud, where  $55^\circ$  and  $131^\circ$  are observed (at 90% filler), respectively).

In compositions with a binder, a gradient transition is observed from particles completely unwetted with polymer to completely wetted (Fig. 3.6 c, 3.6 d, 3.6 e). The “C” condition denotes the polymer wetness of only the lower red mud particles, resulting in water contact angles of  $133^\circ$  and  $138^\circ$  for unannealed and annealed, respectively. The “E” condition denotes complete polymer wetness of the red mud particles, resulting in water contact angles of  $86^\circ$  and  $101^\circ$  for unannealed and annealed, respectively. The average state “D” is also observed, in which there is conditionally half the wetness of the red mud particles by the polymer.

It should be noted that each state is characterized by certain orders of contact angle values (Table 3.2).

Table 3.2 - Water contact angles of red mud composites

| Red mud type | Modifier     | Contact angle in zone, ° |     |     |
|--------------|--------------|--------------------------|-----|-----|
|              |              | C                        | D   | E   |
| Annealed     | -            | 131                      | 104 | 86  |
| Annealed     | Stearic acid | 143                      | 130 | 104 |
| Annealed     | MTES         | 134                      | 127 | 97  |
| Annealed     | OCTEO        | 136                      | 128 | 97  |

It can be seen from the obtained data that the contact angles with water for states C, D, E differ numerically and the dependence of contact angles  $C > D > E$  is preserved.

This difference is determined by 2 factors. The first factor is the water repellency of the surface of the red mud particles themselves. The water repellant layer performs

the function of water repellency better than the styrene-acrylic polymer. This is explained by the presence of nonpolar hydrocarbon chains in the water repellent molecules both in the case of stearic acid and in the case of OCTEO and MTES [84]. This provides a larger contact angle than a polymer that contains polar groups such as  $\text{-OH}$  and  $\text{C=O}$  [85], which reduces the contact angle.

The second factor is determined by the surface texture. In a number of states C, D, E, a gradual decrease in contact angles is observed with an increase in the amount of polymer. At the same time, an increase in the amount of polymer reduces the roughness of the resulting surface, as can be seen from Fig. 3.6.

It is noteworthy that even the composition with untreated red mud water repellent shows a high water contact angle. This indicates that the styrene-acrylic polymer has good film-forming properties and makes it possible to obtain a stable coating that protects well from contact with water.

The most effective water repellent for this system is stearic acid, thanks to which it was possible to achieve a contact angle of  $143^\circ$  in state C. MTES and OCTEO have similar results. Coatings based on them have a contact angle in the C state of  $134^\circ$  and  $136^\circ$ , respectively.

### Conclusions to Chapter 3

In this chapter, it was shown that water repellent surfaces may be obtained using the treated waste red mud as a texture forming agent, that can be considered as a comparable alternative for usual fillers.

The red mud was treated by immobilization of its water-soluble part by annealing at a temperature of  $950^\circ\text{C}$ , the following sieving and chemical modification of the surface with silanes and stearic acid. The resultant disperse material has an average particle size of  $6\mu\text{m}$  and the water contact angle higher than  $140^\circ$  due to the chemical reaction of said treatment agents with the surface OH functional groups.

The organomineral composites on the base of treated particles and styrene-acrylate polymer were obtained. It is shown that the largest contact angle of  $143^\circ$  is achieved when using stearic acid as a water repellent in binder-depleted thin-film composites.

*The results of this chapter were published in:*

1. Миронюк, О. В.; Баклан, Д. В.; Лі, Ч. Водовідштовхувальні тонкоплівкові полімерні композити з частинками червоного шламу як структуроутворювачами. Technologies and Engineering 2023, No. 3, 56–66. 10.30857/2786-5371.2023.3.6
2. O. Myronyuk, D. Baklan, C. Li (2023) Thin film polymer composites incorporating red mud particles as agents for forming textured surfaces with water repellent properties XII international scientific-practical web-conference “Composition Materials” 64-67, Ukraine, <https://ela.kpi.ua/handle/123456789/62024>

## CHAPTER 4. Obtaining of ZnO based particles with controlled morphology

Zinc oxide was selected for nanoparticle synthesis due to its well-known ability to form particles with controllable morphology through variations in synthesis procedures. This system offers high potential for morphological tuning, particularly when employing the hydrothermal synthesis method, which enables precise control over particle shape and structure.

### 4.1. Particle morphology control by synthesis environment tuning

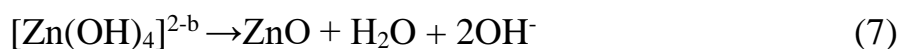
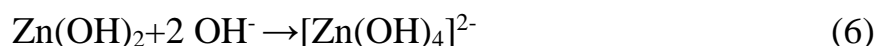
Controlling the synthesis of crystals with a specific morphology is one of the most important goals in crystal synthesis. Hydrothermal methods have become an important method for the controlled synthesis of crystals due to their simplicity and effectiveness. Generally, the precipitation of crystals from a solution involves two consecutive processes: nucleation and growth. The nucleation and growth of crystals can be controlled by adjusting the hydrothermal conditions [86], one can obtain the desired crystal morphology.

Although there have been many reports on the research related to ZnO preparation, it is still of great significance to systematically study the influence of various influencing factors in hydrothermal synthesis on microstructure, especially how to synthesize different morphologies of ZnO by changing simple conditions, which can lay the foundation for the construction of ZnO-related morphology and the realization of specific functions. At the same time, studying the growth mechanism of different morphologies of ZnO under hydrothermal conditions is also of great significance for further discovering the growth law of ZnO crystals.

This chapter mainly studies the synthesis of nano-scale ZnO in different reaction systems and hydrothermal conditions (such as reactant concentration, temperature, and solvent type), and systematically studies the hydrothermal synthesis conditions of morphologically controlled ZnO. At the same time, combined with the final

morphology of the ZnO crystal, the growth process of various morphologies of ZnO under hydrothermal conditions is analysed, and the growth mechanism is preliminarily discussed.

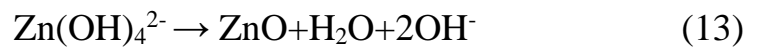
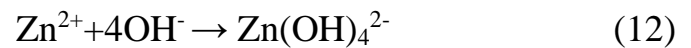
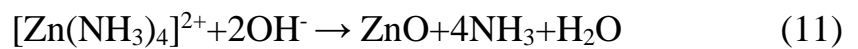
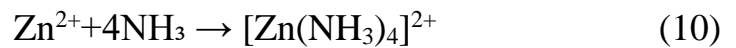
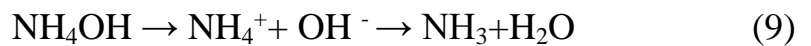
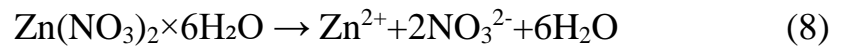
The hydrothermal synthesis may be catalized by alkali, for example sodium or ammonia hydroxide. In the case of NaOH, the simplified reaction stages for the formation of zinc oxide (5-7) :



Among them,  $[\text{Zn}(\text{OH})_4]^{2-}$ ; is the growth nucleus [87]. The formation of flaky nano-zinc oxide in the reaction is completed by dissolving one hydrolysis one nucleation one growth. The aqueous zinc nitrate solution and the aqueous sodium hydroxide solution are mixed to form a white flocculent precipitate of  $\text{Zn}(\text{OH})_2$ . When the solution becomes supersaturated,  $\text{Zn}(\text{OH})_2$  rapidly hydrolyzes to form growth nuclei  $[\text{Zn}(\text{OH})_4]^{2-}$ . The formation of zinc oxide nuclei is caused by the bridging of oxygen between the growth nuclei  $[\text{Zn}(\text{OH})_4]^{2-}$  and the protonation of anionic groups. The above analysis shows that the growth element  $\text{Zn}(\text{OH})_2$  is a key factor in the formation of zinc oxide nuclei. Since OH ions in the solution affect the structure of the growth element and the interfacial properties of the zinc oxide crystal, the growth element grows in different orientations on the zinc oxide nuclei under different  $[\text{OH}^-] / [-\text{Zn}^{2+}]$  molar concentration ratios, resulting in zinc oxide microcrystals with different morphologies. In the zinc blende structure, O<sup>2-</sup> is arranged in a close-packed hexagonal arrangement, with positive and negative charges alternately stacked along the (0001) direction, forming an electric dipole moment and separation of positive and negative charges, which polarises the zinc oxide nuclei. The zinc oxide nuclei form microspheres with  $\text{Zn}(\text{OH})_2$  as the centre through the force of electrical charges [88]. From a crystallographic point of view, the crystal morphology is determined by the

characteristics of the crystal structure, thermodynamics, dynamics and the actual experimental conditions. Zinc oxide crystals have three fast-growing faces: (0001), (1120) and (1010). The (0001) direction is also the hexagonal symmetry direction of zinc oxide crystals. If the growth rate in the (0001) direction is faster than in the other two directions, the resulting zinc oxide may be a columnar or conical crystal; if the growth rate in the (0001) direction is slower than in the other two directions, a flaky product may be obtained [89].

When ammonia is used as a precipitant, the reaction process can be divided into the following six steps (8-13):



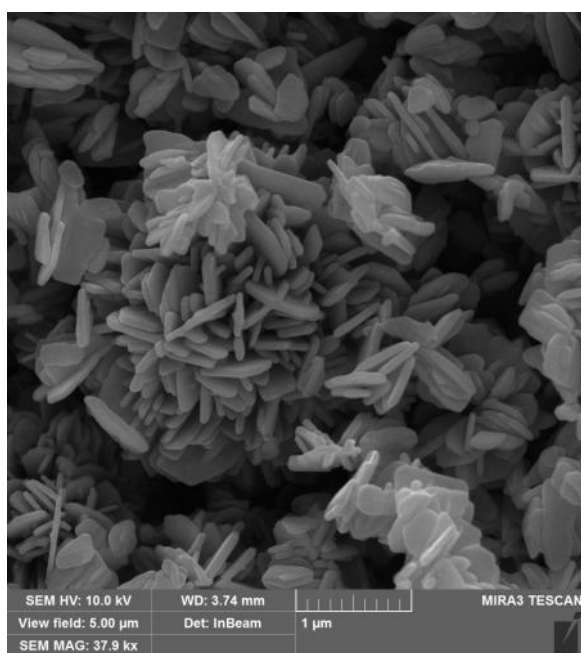
Ammonia is a weak base that, when used as a precipitating agent, does not react directly with zinc nitrate. Instead, it gradually and uniformly releases  $\text{OH}^-$  ions, which subsequently react with  $\text{Zn}^{2+}$  to form the tetrahydroxozincate complex,  $\text{Zn}(\text{OH})_4^{2-}$ . This controlled release of hydroxide ions moderates the rate of ZnO crystal formation, thereby minimizing particle agglomeration and preventing the formation of irregular particles resulting from localized, rapid reactions in the solution.

In aqueous solution,  $\text{NH}_3 \cdot \text{H}_2\text{O}$  dissociates into  $\text{NH}_4^+$  and  $\text{OH}^-$  ions, while simultaneously coordinating with  $\text{Zn}^{2+}$  ions to form the  $[\text{Zn}(\text{NH}_3)_4]^{2+}$  complex. This coordination complex then interacts with  $\text{OH}^-$  ions derived from the dissociation of

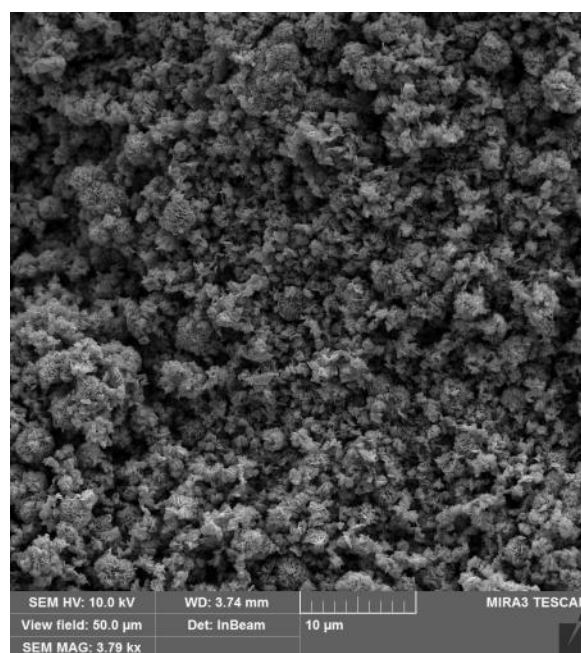
$\text{NH}_3 \cdot \text{H}_2\text{O}$ , leading to the initiation of nucleation. The formation of ZnO nuclei proceeds via a heterogeneous nucleation mechanism, marking the onset of microcrystalline ZnO development.

As reaction time or temperature increases, these ZnO nuclei preferentially grow along the crystallographic c-axis direction (0001), resulting in the formation of ZnO nanorods. Subsequently, depending on the assembly of these nanorods, secondary structures such as flower-like or rod-like morphologies may develop.

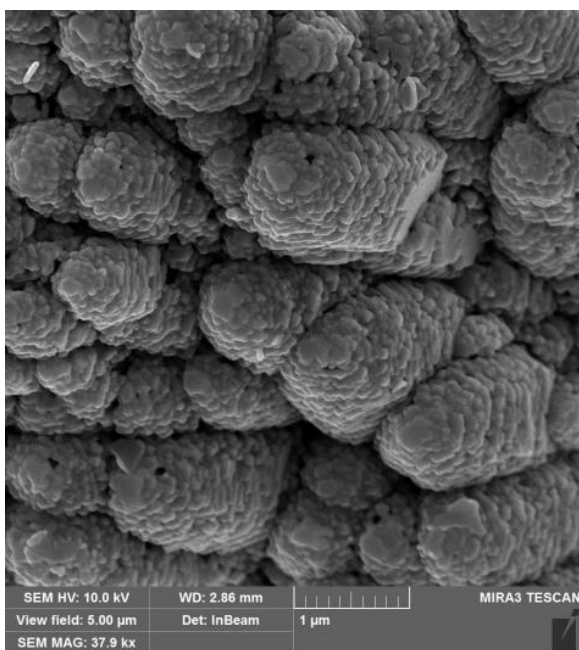
As shown in Fig. 4.1, replacing NaOH with  $\text{NH}_4\text{OH}$  in the reaction leads to fundamentally different crystal morphologies.



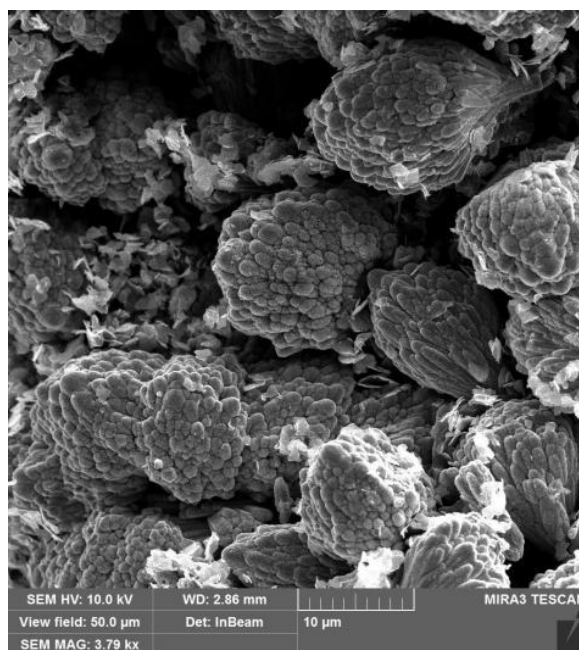
a



b



c



d

Figure 4.1 Effect of different catalysts on the morphology of ZnO: a, b - NaOH and c,d - NH<sub>4</sub>OH

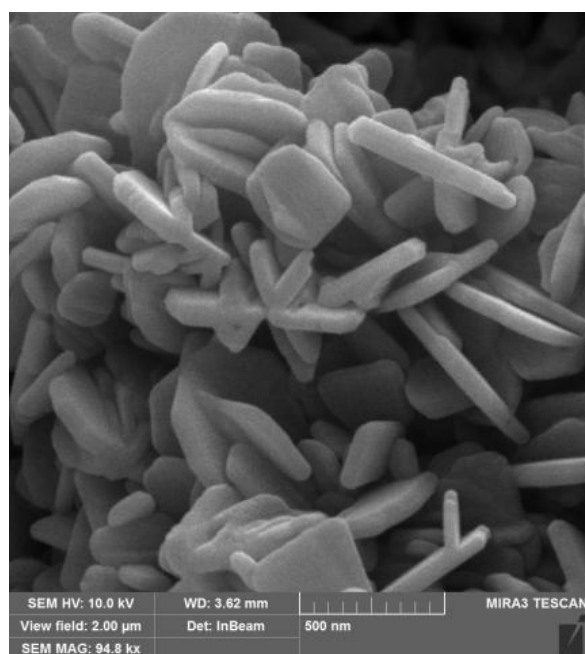
When NaOH is employed as the solvent, the resulting ZnO particles exhibit a flaky morphology characterized by irregularly shaped flakes. The surface of these flakes appears relatively smooth, with dimensions approximately 300–500 nm in length, ~300 nm in width, and ~50 nm in thickness.

In contrast, when NH<sub>4</sub>OH is used as the solvent, the resulting ZnO nanostructures predominantly exhibit a “bud-like” morphology, forming clustered assemblies. Two distinct morphological features are observed: (1) ZnO flower-like clusters are formed via single-growth events, with structures resembling buds. These aggregates typically range from 5 to 10 μm in size, and each “petal” within the bud is composed of a ZnO rod; (2) additionally, several irregular flaky particles are observed in the vicinity of the “buds”, though they are not structurally connected to the flower-like formations.

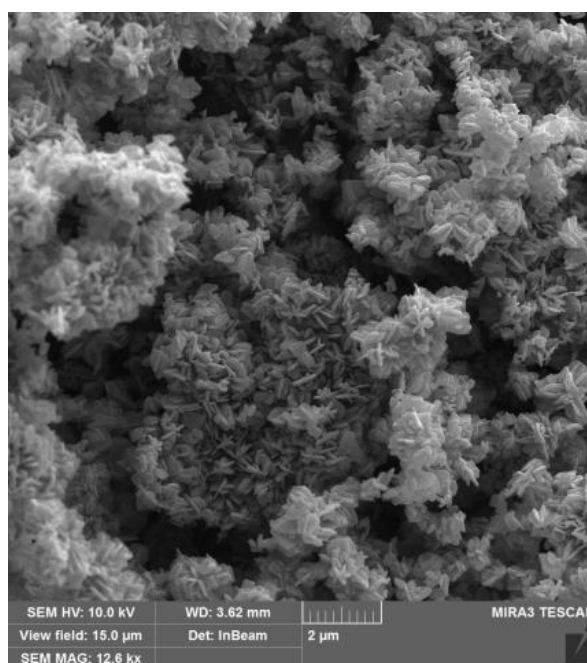
These detached flaky particles are hypothesized to result from incomplete aggregation during the initial stages of the reaction. Specifically, some nuclei of Zn(OH)<sub>2</sub> may have remained dispersed rather than aggregating, leading to the independent formation of spherical ZnO particles. Subsequent anisotropic growth of

these particles may have resulted in their transformation into flaky morphologies. The figure further reveals that a limited number of particles or flakes with both morphological types are distributed throughout the sample [90].

The concentration of the alkaline catalyst in hydrothermal synthesis is one of the key parameters influencing particle morphology. Therefore, this study investigates the effect of catalyst concentration as a means of controlling the structural characteristics of the synthesized particles (Fig 4.2).



a



b

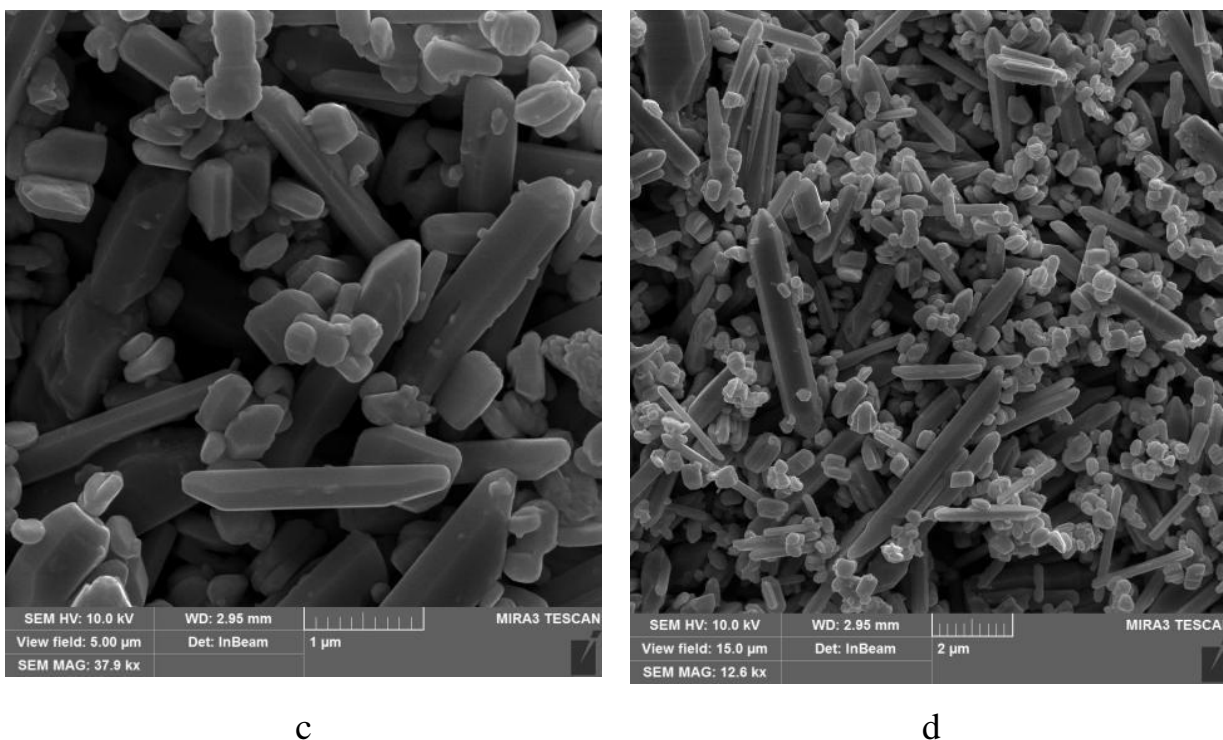
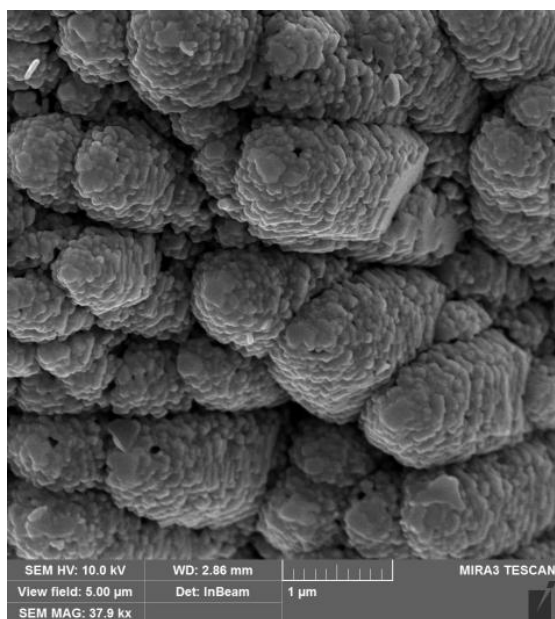


Figure 4.2 Effect of concentration factor of NaOH on particles' morphology

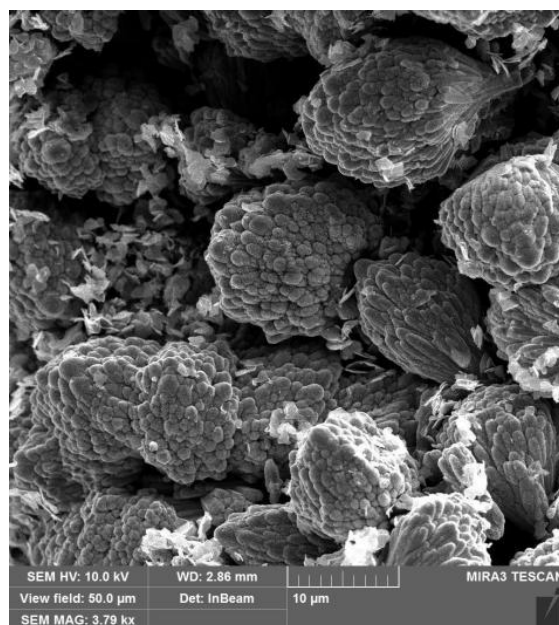
At a NaOH concentration of 5 M, the synthesized ZnO particles exhibit a flaky morphology with smooth surfaces. These nanosheets intersect with one another, and their structure shows a tendency to evolve toward more spheroidal forms.

With increasing NaOH concentration, the sheet-like morphology gradually disappears and is replaced by a rod-like structure. The ZnO product becomes predominantly rod-shaped, with smaller particle sizes and significant variation in rod lengths. The terminal facets of the ZnO nanorods exhibit hexagonal prismatic geometry. These nanorods are unevenly distributed throughout the sample, with some forming aggregated clusters.

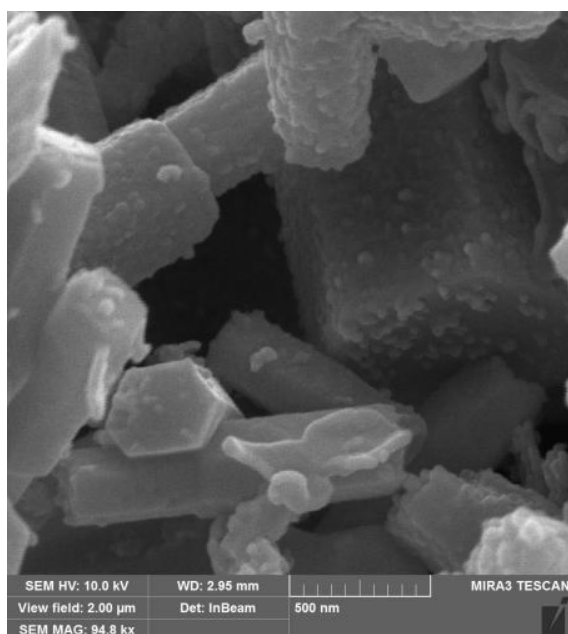
Hydrothermal synthesis temperature is also considered a key factor that enables broad control over particle morphology, shape regularity, and size distribution. Therefore, using  $\text{NH}_4\text{OH}$  as a catalyst, the influence of synthesis temperature (Fig. 4.3) was investigated as a variable parameter in this study.



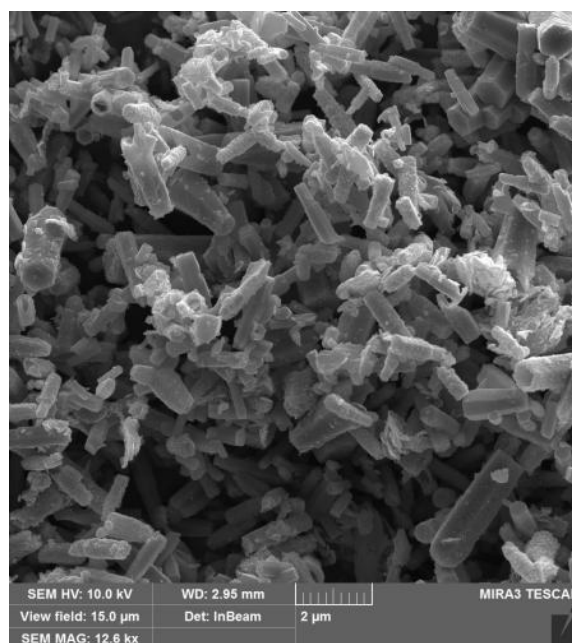
a



b



c



d

Figure 4.3 The effect of different temperatures of  $\text{NH}_4\text{OH}$  catalyzed synthesis of ZnO particles: a,b – 80 °C, c,d – 120 °C.

When ammonia is employed as the alkaline reagent, the morphology of the resulting ZnO structures is strongly influenced by the reaction temperature, even under identical reaction durations. At 80 °C, the ZnO product predominantly exhibits a flower bud-like morphology, whereas at 120 °C, hollow hexagonal prismatic ZnO structures

are obtained. The outer contours of these prismatic particles closely resemble regular hexagons, and their surfaces are decorated with unevenly distributed fine particles.

Observation of fractured regions and prism ends reveals that some prismatic ZnO structures possess closed ends, while others display open ends and hollow interiors, indicating the formation of hollow structures. These findings clearly demonstrate that variations in solvent type, concentration, and reaction temperature exert a pronounced influence on the resulting ZnO morphology under the studied synthesis conditions.

Thus, ZnO nanoparticles were synthesized via a hydrothermal method in a sealed reaction vessel, employing zinc nitrate hexahydrate ( $\text{Zn}(\text{NO}_3)_2 \cdot 6\text{H}_2\text{O}$ ) as the zinc precursor. The morphology of the resulting ZnO crystals was found to be highly sensitive to the nature, concentration, and temperature of the precipitating agent used during synthesis.

The use of NaOH or concentrated aqueous ammonia ( $\text{NH}_3 \cdot \text{H}_2\text{O}$ ) as precipitants led to the formation of ZnO structures with well-developed crystalline morphology. Specifically, under these conditions, the particles exhibited either flaky or flower-like shapes, indicating favorable growth along multiple crystallographic directions and efficient crystal maturation.

When varying the concentration of NaOH, a distinct transition in morphology was observed. At lower concentrations, ZnO predominantly formed as thin flakes, whereas higher NaOH concentrations promoted the formation of rod-like structures, likely due to the enhanced anisotropic growth along the [0001] direction. This suggests that the  $\text{OH}^-$  ion concentration plays a critical role in directing the preferential growth of ZnO crystals.

In contrast, when  $\text{NH}_3 \cdot \text{H}_2\text{O}$  was used as the precipitant, the resulting ZnO morphology was more sensitive to changes in temperature. At different synthesis temperatures, the particles exhibited transitions from flower-like to rod-like shapes. This behavior is attributed to the temperature-dependent release of  $\text{OH}^-$  ions and the

coordination dynamics of  $\text{Zn}^{2+}$  with  $\text{NH}_3$ , both of which affect the nucleation and growth rates during the crystallization process.

Overall, these findings highlight the strong dependence of ZnO nanostructure morphology on the choice and conditions of the alkaline environment, offering valuable insights for tailoring ZnO nanomaterials for specific functional applications.

#### 4.2. ZnO particles morphology control via doping

The use of alloying additives such as titanium dioxide ( $\text{TiO}_2$ ) and silicon dioxide ( $\text{SiO}_2$ ) represents a promising strategy for the synthesis of zinc oxide (ZnO) particles with controllable morphology. These oxides act as structure-directing agents during the crystallization process, influencing the growth rates of different crystallographic planes of ZnO. Their incorporation into the reaction medium can lead to the formation of new surface-active complexes or intermediate phases, which modify the nucleation and growth mechanisms. This enables the formation of ZnO particles with tailored shapes—such as rods, plates, or hierarchical structures—which are crucial for optimizing their functional properties in photocatalysis, optoelectronics, and sensor applications.

Moreover,  $\text{TiO}_2$  and  $\text{SiO}_2$  additives can affect the surface energy and charge distribution of growing ZnO crystals, promoting anisotropic growth under hydrothermal or solvothermal conditions. These additives can also serve as nucleation centers or inhibit uncontrolled agglomeration, leading to improved particle uniformity and dispersibility. The synergy between ZnO and these oxides may also enhance the thermal stability and surface reactivity of the resulting materials. Thus, the deliberate introduction of Ti- and Si-containing compounds during synthesis offers a versatile approach to engineer ZnO morphology and expand its application potential across a range of advanced technologies.

All doped particle materials were synthesized by a known solution exchange method described by Jiang et.al in [91] in a following way: (5 M) NaOH solution dropwise added to 15 mL (1.67 M)  $\text{Zn}(\text{NO}_3)_2 \cdot 6\text{H}_2\text{O}$  under stirring for 30 min; transferred to a 50 mL reactor at  $150^\circ\text{C}$  for 6 hours. The product wash twice with water on the centrifuge, and dried at  $80^\circ\text{C}$  for 6 hours to obtain ZnO sample. In one case 0.5g of  $\text{TiO}_2$  (P25, Degussa, median particle size 21 nm) was added at the initial step before alkali introduction – the sample is noted ZnO:Ti. In other case – the additive was 0.3 g  $\text{SiO}_2$  (Sipernat 22 S, Evonik, median particle size 14  $\mu\text{m}$ ) – the sample is noted ZnO:Si.

The doped materials were analyzed using various characterization techniques, with particular emphasis on X-ray diffraction (XRD) to assess their crystalline structure (Fig. 4.4).

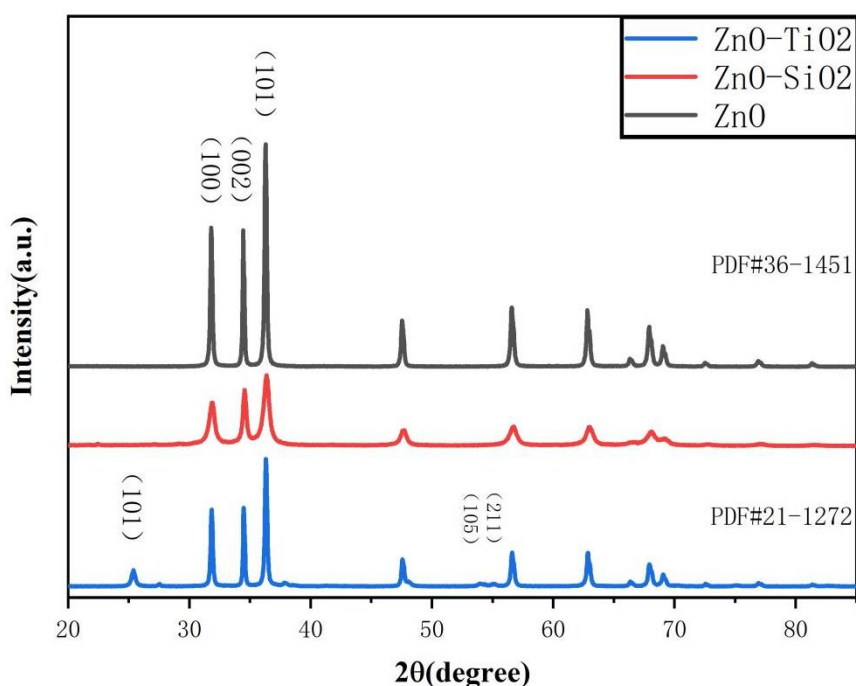


Figure 4.4 X-ray refractograms of synthesized doped particles

The diffraction peaks of the particles correspond to the JCPDS standard card (JCPDS36·1451). The diffraction peaks have  $2\theta$  angles of  $31.76^\circ$ ,  $34.42^\circ$ ,  $36.25^\circ$ ,  $47.53^\circ$ ,  $56.60^\circ$ ,  $62.86^\circ$ ,  $66.37^\circ$ ,  $67.96^\circ$ ,  $69.09^\circ$ ,  $72.56^\circ$  and  $76.95^\circ$ , which correspond

to (100), (002), (101), (102), (110), (103), (200), (112), (201), (004) and (202)) of ZnO nanoparticles. The absence of other diffraction peaks in the figure indicates that the samples prepared in this experiment are all pure zinc oxide.

The XRD test results of the composite material of ZnO - SiO<sub>2</sub> is shown in Figure 4.4. The diffraction peaks of the composite material correspond to the JCPDS standard card (JCPDS36-1451). The diffraction peaks have 2θ angles of 31.76°, 34.42°, 36.25°, 47.53°, 56.60°, 62.86°, 66.37°, 67.96°, 69.09°, 72.56° and 76.95°, which correspond to (100), (002), (101), (102), (110), (103), (200), (112), (201), (004) and (202) planes of ZnO nanoparticles.

Some diffraction peaks show bulges near 22.4°, and the diffraction peaks are wider and not as sharp as those of ZnO. This is because the addition of SiO<sub>2</sub> during the composite process inhibits the crystallisation of ZnO, and because Si enters the ZnO lattice, causing distortion of the ZnO lattice, preventing movement of the grain boundaries, inhibiting the growth of ZnO, and resulting in broadening of the peaks [92]. It can also be seen that the SiO<sub>2</sub> added in this experiment has an amorphous state and no obvious characteristic peaks [93]. Most of SiO<sub>2</sub> peaks are masked by the peaks of ZnO, and Si is highly dispersed in the ZnO crystal lattice, which weakens the characteristic peak signal and is therefore not obvious in the XRD spectrum [9495],

The X-ray diffraction (XRD) analysis of the composite material comprising flaky ZnO and TiO<sub>2</sub> is presented in Fig. 4.4. The diffraction peaks associated with ZnO are in good agreement with the standard reference data provided by the Joint Committee on Powder Diffraction Standards (JCPDS card no. 36-1451), confirming the crystalline structure of the ZnO phase. The identified peaks appear at 2θ angles of 31.76°, 34.42°, 36.25°, 47.53°, 56.60°, 62.86°, 66.37°, 67.96°, 69.09°, 72.56°, and 76.95°, which correspond to the (100), (002), (101), (102), (110), (103), (200), (112), (201), (004), and (202) crystallographic planes, respectively. These reflections indicate the presence of a hexagonal wurtzite structure of ZnO, which is characteristic of well-crystallized ZnO nanoparticles.

In addition, distinct diffraction peaks corresponding to  $\text{TiO}_2$  are observed and are consistent with the anatase phase, as confirmed by comparison with the standard JCPDS card no. 21-1272. The prominent peaks appear at  $2\theta$  values of  $25.281^\circ$ ,  $48.049^\circ$ ,  $53.890^\circ$ , and  $55.060^\circ$ , which can be indexed to the (101), (200), (105), and (211) crystallographic planes, respectively. These reflections confirm the successful incorporation of anatase-phase  $\text{TiO}_2$  nanoparticles within the  $\text{ZnO}/\text{TiO}_2$  composite structure.

The presence of sharp and well-defined diffraction peaks for both  $\text{ZnO}$  and  $\text{TiO}_2$  phases indicates a high degree of crystallinity in the composite material. The coexistence of these two phases without the appearance of impurity peaks suggests that the synthesis process preserved the individual crystalline structures of  $\text{ZnO}$  and  $\text{TiO}_2$ , enabling the formation of a structurally stable heterojunction.

However, the positions and shapes of the characteristic peaks of the composite  $\text{ZnO}$  with different doping are slightly different, indicating that the crystal structures of the composite  $\text{ZnO}$  are not completely the same. The possible reasons for this are that Si or Ti is doped into the  $\text{ZnO}$  lattice, or is attached to the crystal surface, which causes lattice distortion and results in changes.

The morphology of all three materials—pure  $\text{ZnO}$ ,  $\text{ZnO}$  doped with silicon dioxide, and  $\text{ZnO}$  doped with aluminum oxide—was studied using scanning electron microscopy (Fig. 4.5), which enabled detailed evaluation of the structural features of the resulting crystals.

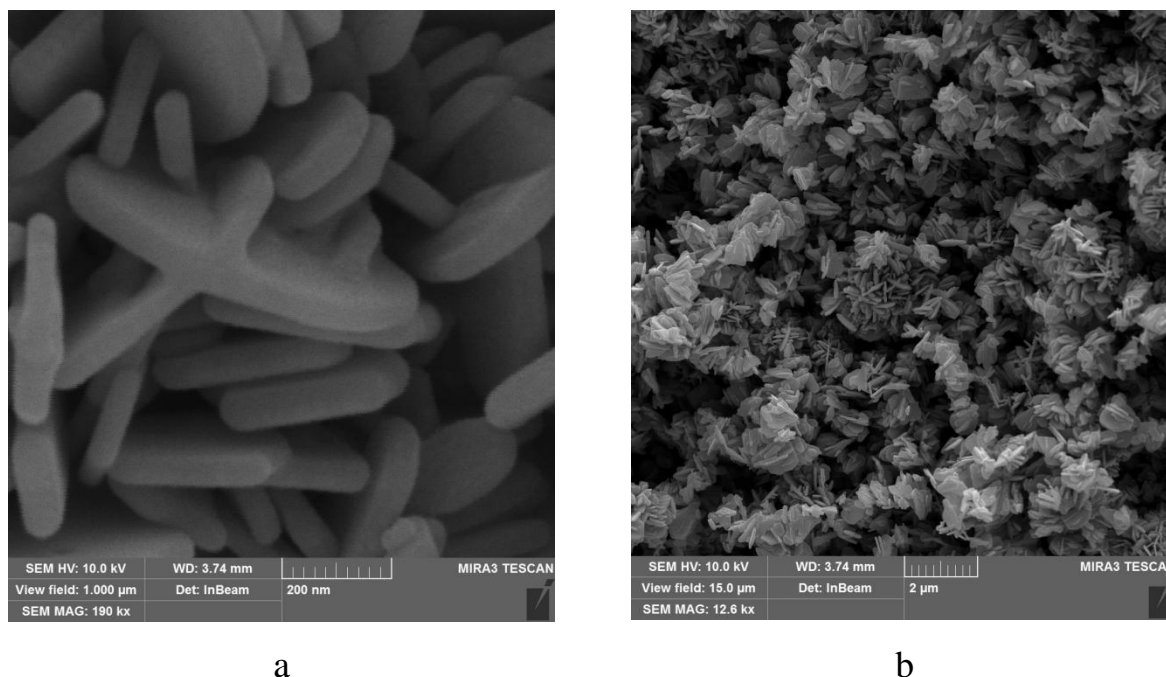


Figure 4.5 Morphology of ZnO particles at different magnification (a,b)

As illustrated in Figure 4.5, the ZnO particles synthesized using sodium hydroxide (NaOH) as the precipitating agent predominantly exhibit the morphology of thin, smooth-surfaced nanosheets. These ZnO flakes display a high degree of uniformity, with lateral dimensions averaging approximately 500 nm in diameter and a thickness of around 50 nm. The nanosheets are intricately intertwined and interconnected, forming a loosely stacked, three-dimensional network. This assembly demonstrates a clear tendency toward a quasi-spherical architecture, indicative of self-organization into hierarchical layered structures.

Such hierarchical structuring, which integrates both micro- and nanoscale features, is reminiscent of natural superhydrophobic surfaces, such as those observed on lotus and taro leaves. These biological analogues are known for their unique surface textures, which contribute to properties such as water repellency and self-cleaning. Similarly, the ZnO nanosheet assemblies exhibit structural complexity that may be advantageous for applications requiring large surface area, enhanced light scattering, or multifunctional surface activity.

The ZnO nanosheets also demonstrate good dispersion, a narrow particle size distribution, and well-defined morphology, suggesting a high level of control during the synthesis process. X-ray diffraction (XRD) analysis of the ZnO powder reveals diffraction patterns consistent with the standard JCPDS card no. 36-1451, confirming that the crystal structure corresponds to the wurtzite (hexagonal) phase of ZnO. No secondary or impurity phases were detected, indicating high phase purity of the synthesized product.

As depicted in Figure 4.6, the synthesized ZnO material primarily consists of interwoven, sheet-like nanoparticles that form a loosely packed, layered structure. These nanosheets are characterized by clearly visible striations on their surfaces, indicative of anisotropic crystal growth and well-developed planar facets. Granular SiO<sub>2</sub> particles are observed to be deposited on the surface of the aggregated ZnO sheets, adhering both individually and in small clusters without significantly altering the underlying ZnO morphology.

The incorporation of SiO<sub>2</sub> does not appear to substantially affect the geometric parameters of the ZnO nanosheets. The characteristic dimensions of the sheets remain largely consistent after silica loading, with lengths ranging from 200 to 500 nm, widths between 300 and 400 nm, and thicknesses maintained within the 30 to 50 nm range. This indicates that the SiO<sub>2</sub> particles are predominantly surface-bound rather than embedded within the ZnO crystal lattice, suggesting a heterogeneous composite structure formed via physical adsorption or surface interaction mechanisms.

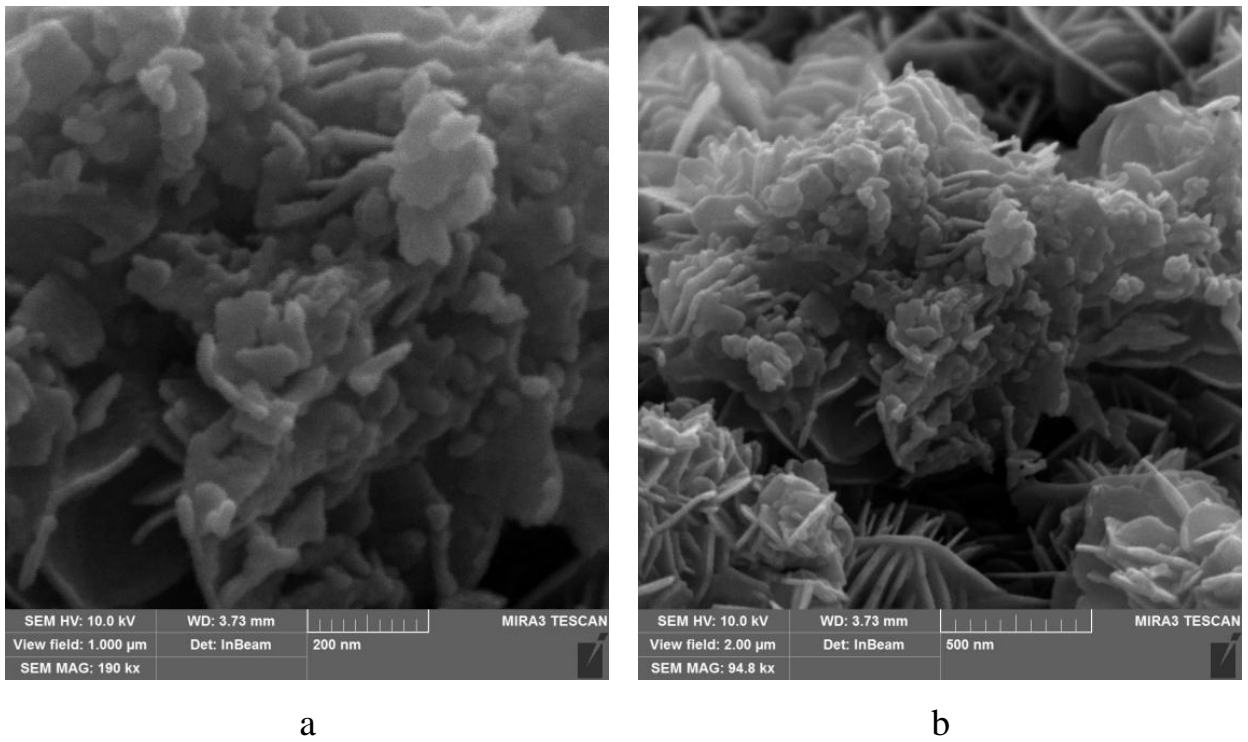


Figure 4.6 Morphology of ZnO - SiO<sub>2</sub> particles at different magnification (a,b)

The preservation of the nanosheet structure following SiO<sub>2</sub> deposition is advantageous for maintaining the intrinsic surface area and directional properties of ZnO, while potentially imparting new surface functionalities—such as enhanced chemical stability, tunable surface energy, or improved compatibility with organic or hybrid systems. The retained sheet morphology and structural clarity also imply that the silica addition does not interfere with the nucleation or growth pathways of ZnO during synthesis, highlighting the robustness of the nanosheet architecture under modification.

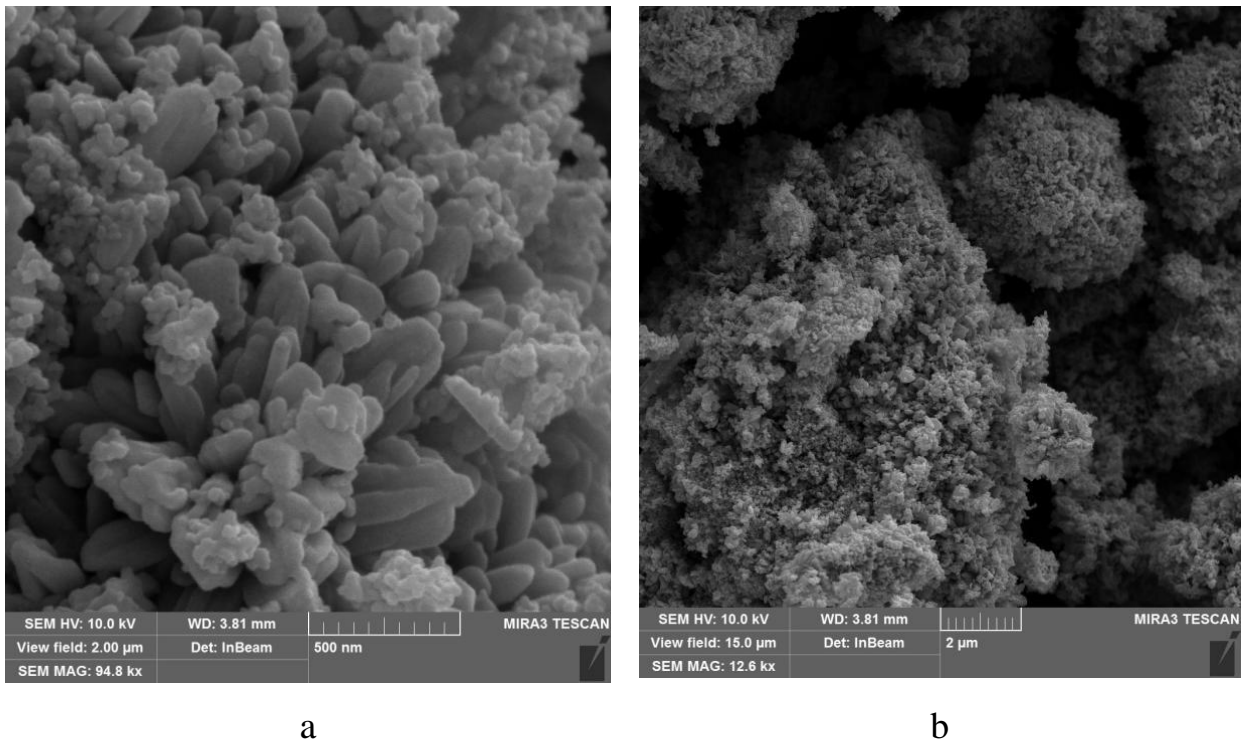


Figure 4.7 ZnO-TiO<sub>2</sub> particles at different magnification (a,b)

Figure 4.7 presents the morphological characteristics of the ZnO–TiO<sub>2</sub> composite nanoparticles. Upon the introduction of TiO<sub>2</sub> into the system, the surface of the pre-formed flaky ZnO nanosheets becomes uniformly coated with a fine layer of TiO<sub>2</sub> nanoparticles. This surface modification results in a marked transformation in the dispersion behavior and overall morphology of the ZnO component.

Compared to the pure flaky ZnO particles, which exhibit well-defined, smooth, and highly dispersed nanosheet structures, the presence of TiO<sub>2</sub> significantly reduces the dispersibility of the ZnO flakes. The individual nanosheets begin to exhibit a stronger tendency toward aggregation, leading to a more compact and disordered arrangement. The clear morphological features that were previously observed become less distinct, and the overall shape of the particles becomes more irregular. Furthermore, there is a noticeable shift in the growth direction, with the structure showing a tendency to evolve toward more spheroidal or partially rounded forms.

This morphological transformation may be attributed to the possible incorporation of TiO<sub>2</sub> species into the ZnO crystal lattice or their interaction at the ZnO surface. Such

interactions could disrupt the anisotropic growth kinetics of ZnO, suppressing grain elongation along preferred crystallographic directions and leading to inhibited crystallite growth. This, in turn, favors the formation of more isotropic, agglomerated structures.

The resulting composite material exhibits a loosely packed, fluffy, and porous architecture, with a distinctly rough surface texture. This hierarchical surface topography is of particular importance, as it plays a critical role in enhancing the material's hydrophobic properties. The presence of micro- and nanoscale roughness promotes the formation of air pockets on the surface, which is essential for achieving water-repellent behavior through the Cassie–Baxter effect.

A more in-depth analysis of the doped materials was performed using transmission electron microscopy (TEM), supported by complementary techniques such as energy-dispersive spectroscopy (EDS) to characterize the elemental composition of the synthesized products.

High-resolution transmission electron microscopy (HRTEM) analysis was conducted to examine the morphology, particle size, lattice structure, and internal crystalline features of the synthesized nanomaterials. The observations were carried out using a JEM-2010F transmission electron microscope (JEOL, Japan Electronics Co., Ltd.), a high-performance instrument suitable for advanced structural characterization at the nanoscale.

Prior to imaging, the sample was prepared by dispersing a measured quantity of the synthesized material in absolute ethanol using ultrasonication to ensure uniform dispersion and to minimize particle agglomeration. A small droplet of the resulting suspension was then carefully deposited onto a carbon-coated copper grid. After drying at ambient conditions, the grid was introduced into the TEM chamber for analysis.

The instrument was operated under the following conditions: an accelerating voltage of 200 kV, a point resolution of 0.23 nm, and a lattice resolution of 0.14 nm. The microscope offered a magnification range from 50× to 1,500,000×, enabling both

low- and high-magnification imaging of structural and morphological features. The high-resolution imaging capability allowed for direct visualization of atomic lattice fringes, from which interplanar spacings (d-values) could be accurately measured. These d-spacing values serve as fingerprints for identifying crystalline phases and distinguishing between different types of nanomaterials present in the sample.

By comparing the measured lattice spacings with standard crystallographic databases, the specific phases and structures of the nanoparticles - such as ZnO or TiO<sub>2</sub> - can be conclusively identified. This analytical approach is essential for verifying the successful formation of composite or doped nanomaterials, as well as for understanding the relationship between synthesis conditions and the resulting microstructural features.

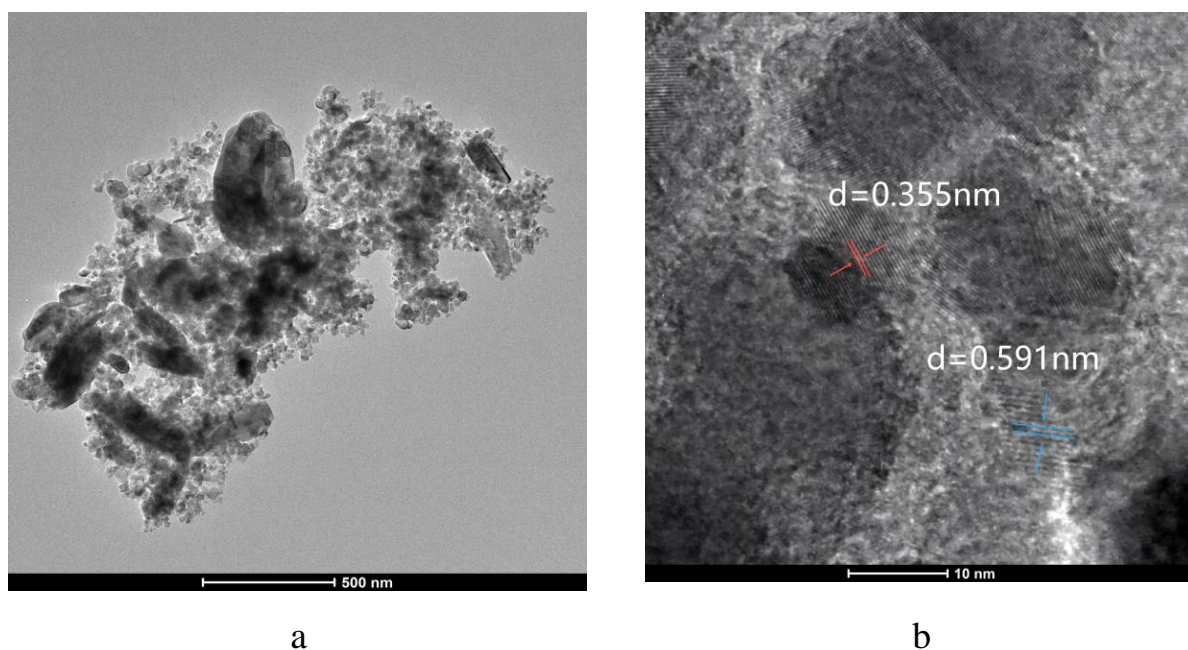


Figure 4.8 TEM image of ZnO-TiO<sub>2</sub> sample: a - 500 nm image, b - high-magnification TEM

As shown in Figure 4.8b, the ZnO –TiO<sub>2</sub> composite sample exhibits clearly visible lattice fringes under high-resolution transmission electron microscopy (HRTEM), indicating a well-defined crystalline structure. The measured interplanar spacing between these fringes is approximately 0.355 nm, which corresponds to the (200)

crystallographic plane of  $\text{ZnO}_2$ , confirming the presence of this specific orientation within the ZnO phase.

Figure 4.8a provides a broader overview of the material's morphology, revealing the characteristic flaky structure of the ZnO particles. Surrounding these flakes, granular  $\text{TiO}_2$  nanoparticles are observed to be distributed relatively uniformly across the surface and interstitial regions. The overall particle size appears consistent, further supporting the homogeneity of the synthesized composite.

To gain deeper insight into the internal crystal structure of the composite, detailed analysis was performed in the region highlighted by the blue line in the HRTEM image. This region displays well-ordered and distinct lattice fringes, further confirming the high crystallinity of the material. These lattice features are attributed to the  $\text{TiO}_2$  component of the composite and are consistent with its anatase phase.

Specifically, the lattice spacing in this region was measured to be approximately 0.591 nm, which corresponds to the (420) plane of anatase  $\text{TiO}_2$ . This assignment is in agreement with standard crystallographic data and confirms the presence of anatase-structured  $\text{TiO}_2$  integrated within the ZnO matrix. The coexistence of multiple crystallographic phases with well-resolved lattice structures highlights the successful formation of a structurally coherent ZnO– $\text{TiO}_2$  composite, which may be advantageous for applications requiring heterojunction-based functionalities, such as photocatalysis or sensing.

The elemental distribution maps in Figure 4.9 provide insight into the spatial arrangement of oxygen, titanium, and zinc in the ZnO– $\text{TiO}_2$  composite. Image (a), corresponding to oxygen (O), reveals a relatively uniform dispersion of oxygen throughout the sample, indicating that both ZnO and  $\text{TiO}_2$  phases are well distributed. The oxygen signal closely follows the morphology of the particles, covering both flaky and granular features, which confirms its involvement in both oxide components.

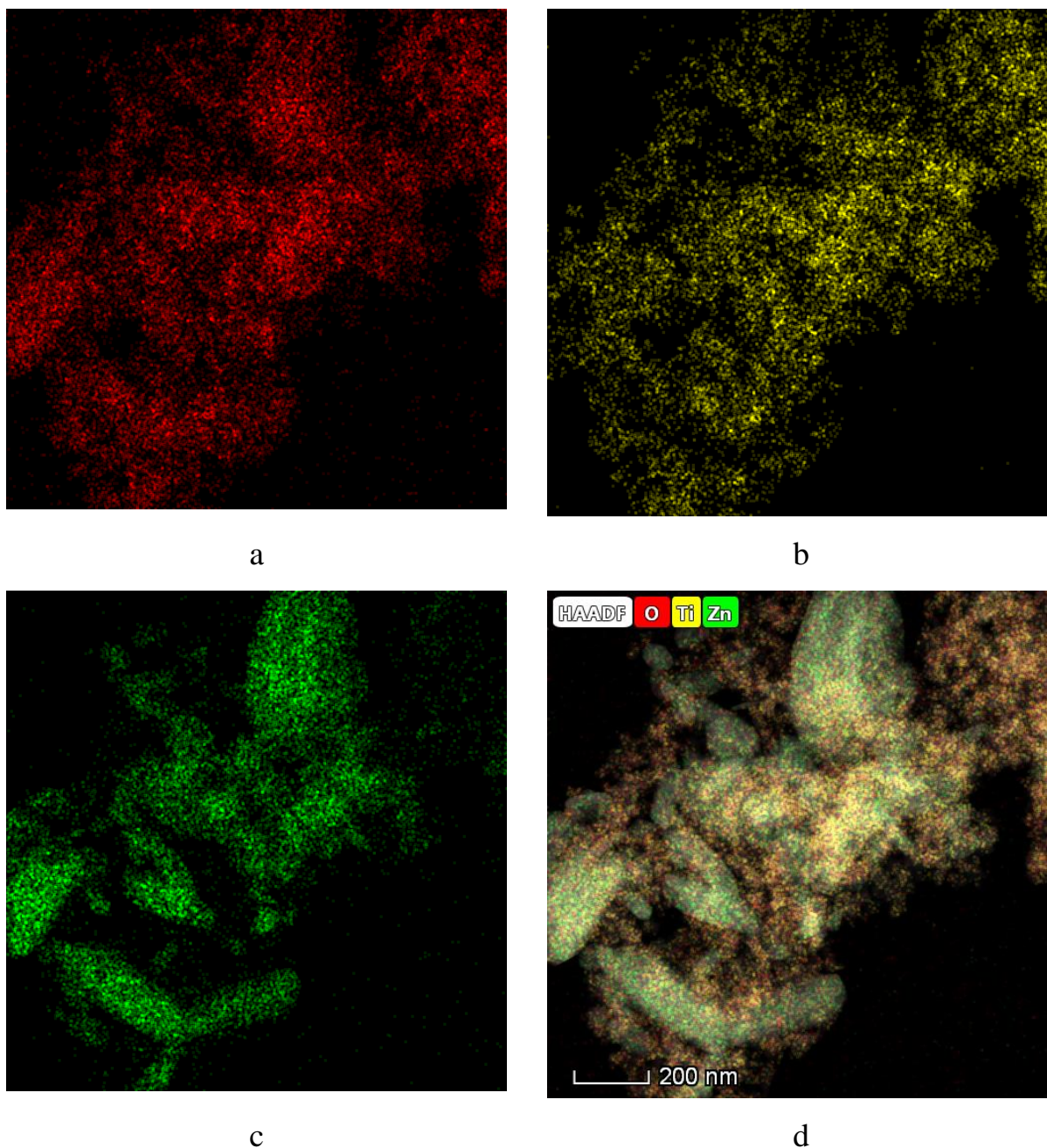


Figure 4.9 Element distribution in ZnO–TiO<sub>2</sub> composite: a – oxygen (O); b – titanium (Ti); c – Zinc (Zn); d - total element distribution map

Image (4.9 b) represents the distribution of titanium (Ti). The Ti signal is concentrated in discrete, granular regions, which are scattered over the sample. These regions correspond to TiO<sub>2</sub> particles, suggesting their localized deposition around or between the larger ZnO platelets. The absence of titanium signal in the flaky domains

further supports the conclusion that  $\text{TiO}_2$  is present as a separate, finely distributed phase rather than forming a solid solution with  $\text{ZnO}$ .

In image (c), the zinc (Zn) signal is observed predominantly within the larger, flake-like structures, confirming their attribution to  $\text{ZnO}$ . This spatial separation between the Ti and Zn signals is clearly visible in the total element distribution map (d), which overlays the signals for O, Ti, and Zn. In this composite image, the  $\text{ZnO}$  flakes are highlighted in green, while the  $\text{TiO}_2$  granules appear as yellow-red zones, emphasizing the phase separation and the successful formation of a heterogeneous composite with distinguishable oxide domains.

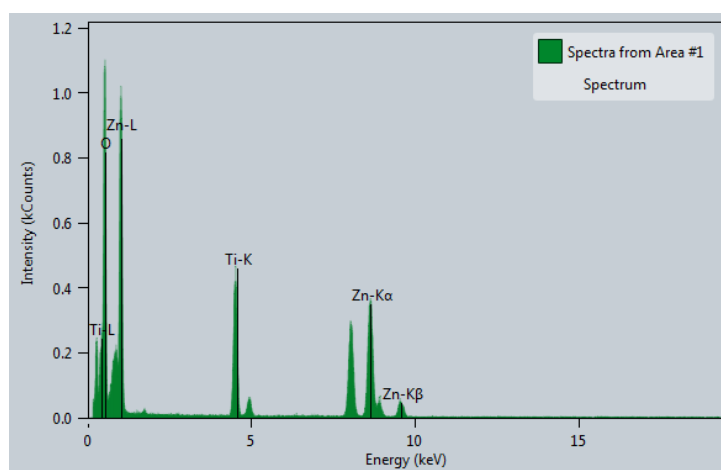


Figure 4.10 EDS spectrum of the corresponding area of  $\text{ZnO-TiO}_2$

The EDS spectrum presented in Figure 4.10 confirms the presence of the key elements constituting the  $\text{ZnO-TiO}_2$  composite. The most intense peak appears at approximately 0.5 keV, corresponding to the oxygen  $\text{K}\alpha$  line, which reflects the high oxygen content expected from the metal oxide phases. The sharp peaks at ~1 keV (Zn-L) and ~8.6 keV (Zn- $\text{K}\alpha$ ) are attributed to zinc, indicating the dominance of the  $\text{ZnO}$  phase in the analyzed region.

A distinct peak at ~4.5 keV corresponds to the Ti- $\text{K}\alpha$  line, confirming the presence of titanium within the scanned area. The relative intensity of the titanium signal,

compared to that of zinc, suggests a lower local concentration of  $\text{TiO}_2$  particles, in agreement with the elemental mapping results. Additionally, the  $\text{Zn-K}\beta$  peak is observed at  $\sim 9.6$  keV, further reinforcing the identification of zinc as a major component.

No peaks from other elements are present in the spectrum, indicating a high purity of the  $\text{ZnO-TiO}_2$  system in the examined area and absence of contaminants or residual precursors. The spectrum thus validates the compositional integrity of the composite and supports the interpretation of spatially distinct but coexisting  $\text{ZnO}$  and  $\text{TiO}_2$  phases.

These analytical methods were also applied to characterize the composite material based on zinc oxide and silicon dioxide.

The TEM images presented in Figure 4.11 provide insight into the nanoscale morphology of the  $\text{ZnO/SiO}_2$  composite material. The left image, captured at lower magnification, reveals that the  $\text{ZnO}$  component forms distinct, well-defined crystalline lamellae with sharp edges and varying aspect ratios. These structures are embedded within an amorphous matrix, which is likely attributed to the  $\text{SiO}_2$  phase. The spatial distribution of the lamellae suggests partial agglomeration, yet the contrast differences between crystalline and amorphous regions clearly distinguish the two phases. The average dimensions of the lamellar  $\text{ZnO}$  particles are on the order of 50–150 nm in length.

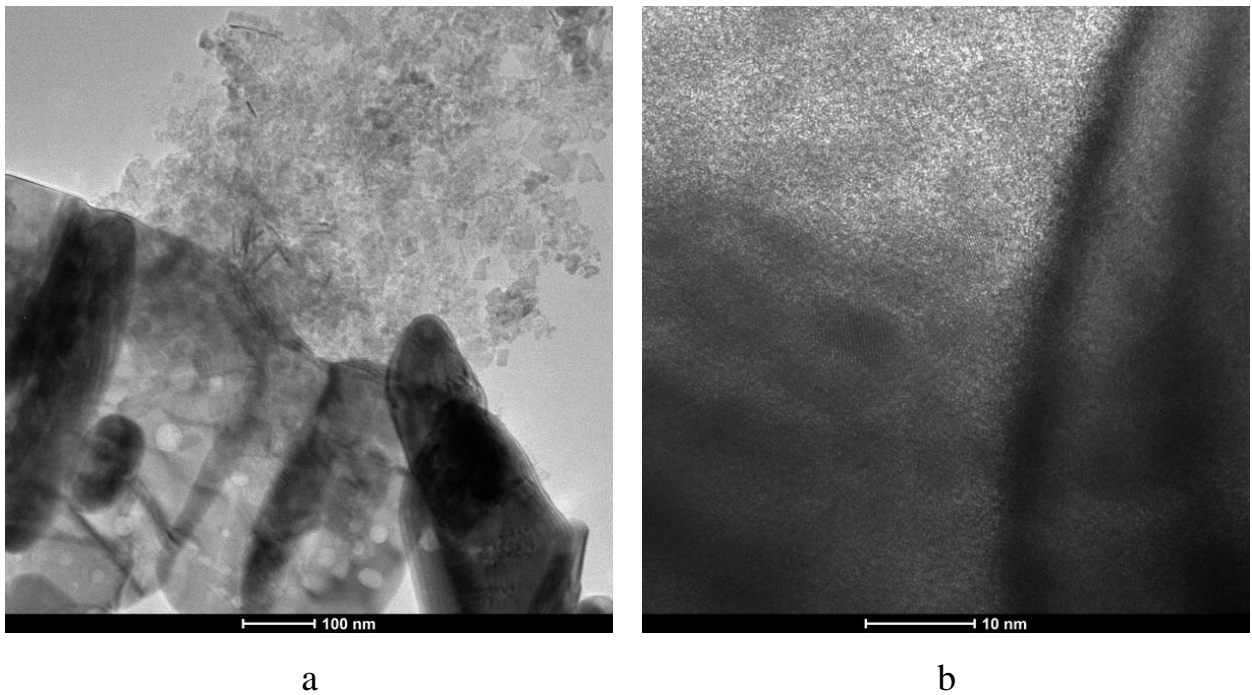
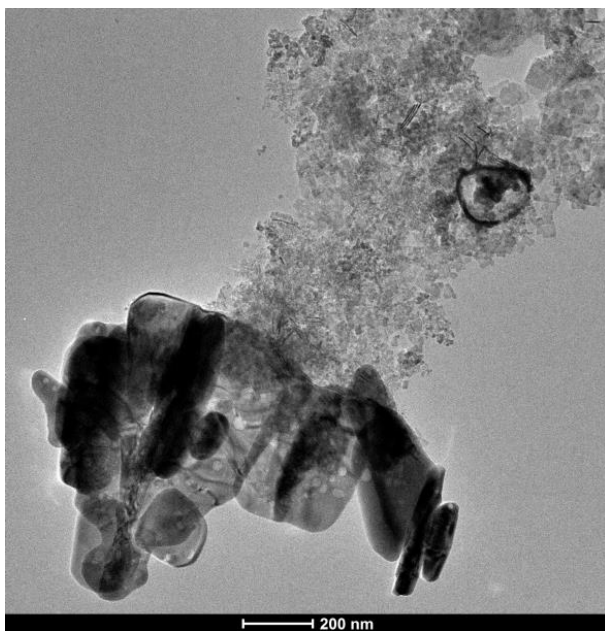
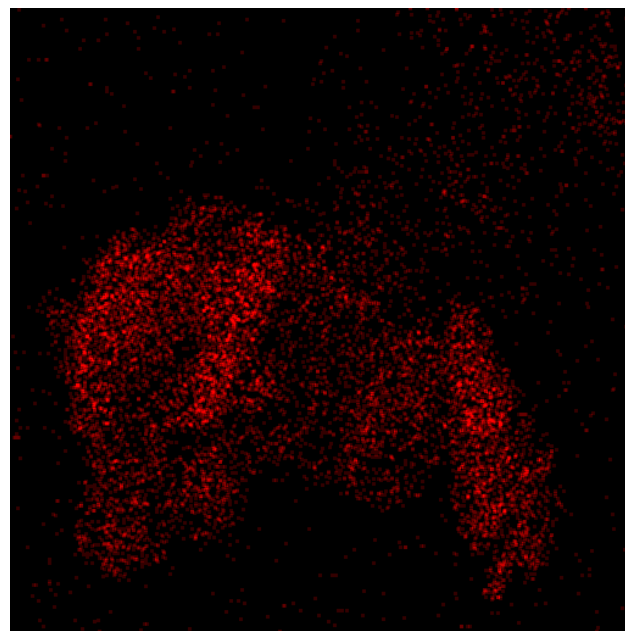


Figure 4.11 High-resolution electron microscope photo of the surface of a nanometer ZnO/SiO<sub>2</sub> composite material

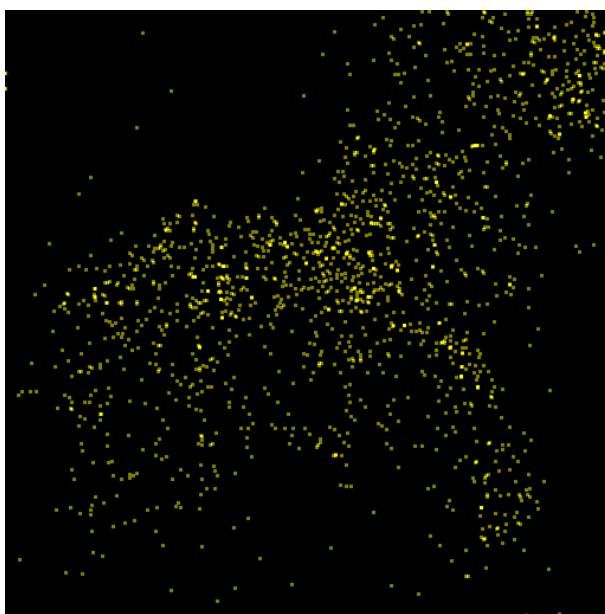
The right image, taken at higher magnification, shows the surface of the composite in greater detail. The absence of lattice fringes within the amorphous regions supports the assignment of these zones to silica, whereas adjacent regions with uniform texture and faint contrast gradients correspond to the crystalline ZnO phase. The interface between the ZnO and SiO<sub>2</sub> appears smooth and continuous, suggesting a homogeneous integration at the nanoscale. This intimate contact between the crystalline and amorphous phases is favorable for achieving synergistic effects in composite materials, particularly for applications requiring high surface area and interfacial interaction.



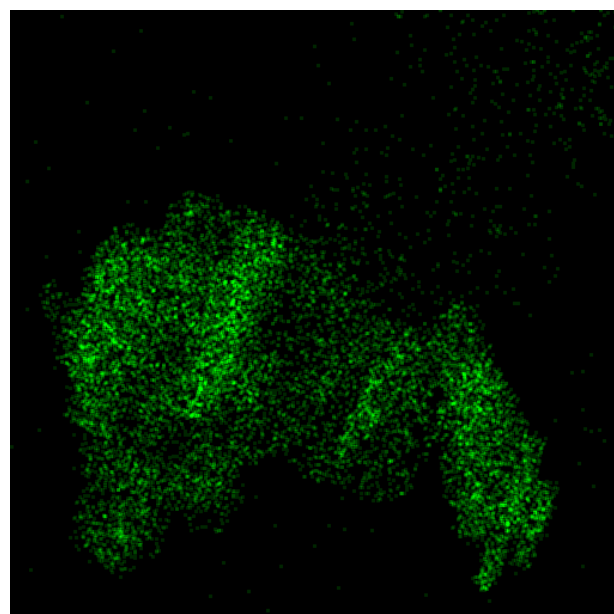
a



b



c



d

Figure 4.12 Element distribution in ZnO–SiO<sub>2</sub> composite: a – oxygen (O); b – titanium (Ti); c – Zinc (Zn); d - total element distribution map

The elemental mapping data presented in Figure 4.12 confirms the successful formation of the ZnO–SiO<sub>2</sub> composite and illustrates the spatial distribution of its constituent elements. The oxygen (O) signal (Fig. 4.12a) is uniformly distributed across

the entire sample, reflecting its presence in both ZnO and SiO<sub>2</sub> phases. The zinc (Zn) signal (Fig. 4.12c) is concentrated within distinct regions, indicating the localized presence of ZnO crystallites. These areas coincide with the denser domains observed in the TEM image, supporting the interpretation that these are Zn-rich crystalline phases embedded in an amorphous matrix.

The titanium (Ti) distribution (Fig. 4.12b), while less intense and more diffuse, suggests a low-level doping or surface modification rather than a separate TiO<sub>2</sub> phase. The total element distribution map (Fig. 4.12d) integrates the signals from all elements, highlighting the compositional heterogeneity at the nanoscale. The core of the structure appears enriched with zinc, while the surrounding zones contain higher concentrations of oxygen and silicon, consistent with an amorphous SiO<sub>2</sub> shell or matrix. These findings confirm the composite nature of the material and the successful spatial integration of the metal oxides at the nanoscale.

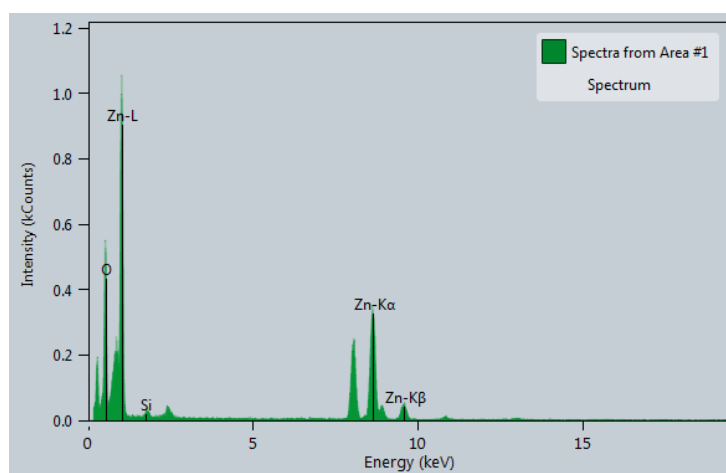


Figure 4.13 EDS analysis results for ZnO–SiO<sub>2</sub> composite particles

The EDS spectrum shown in Figure 4.13 confirms the elemental composition of the ZnO–SiO<sub>2</sub> composite particles. The dominant peaks correspond to zinc (Zn), with strong signals observed for the Zn L $\alpha$  (~1 keV), Zn K $\alpha$  (~8.6 keV), and Zn K $\beta$  (~9.5 keV) transitions, indicating a high concentration of zinc within the analyzed area.

These peaks are characteristic of the ZnO phase and align well with the previous TEM and elemental mapping data, verifying the presence of crystalline zinc oxide regions.

In addition to zinc, smaller peaks are also observed in the lower energy region, corresponding to oxygen (O) and silicon (Si), which are consistent with the presence of the amorphous SiO<sub>2</sub> phase. The relatively lower intensity of these peaks compared to Zn suggests that SiO<sub>2</sub> is present in a dispersed or less concentrated form within the composite. The absence of any significant impurity peaks confirms the chemical purity of the synthesized material. Overall, the EDS analysis supports the successful formation of a ZnO–SiO<sub>2</sub> composite with a dominant ZnO content and an integrated silica matrix.

As illustrated in Figure 4.14, the photoluminescence (PL) spectra of ZnO, ZnO–SiO<sub>2</sub>, and ZnO–TiO<sub>2</sub> samples are presented for comparative analysis. All three materials exhibit a prominent emission peak in the wavelength range of 550–650 nm, which is characteristic of deep-level emissions commonly observed in ZnO-based nanostructures. This emission is attributed to the radiative recombination of photoexcited electrons from the conduction band with holes in the valence band. The energy released during this recombination process gives rise to visible light emission, indicating the presence of intrinsic or defect-related electronic states.

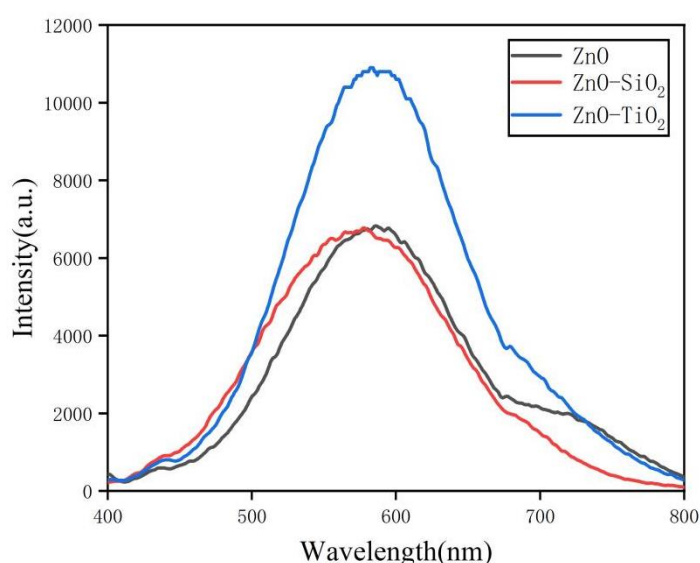


Figure 4.14 Photoluminescence spectra for ZnO and its doped composites

When comparing the PL emission positions, a distinct spectral shift is observed relative to pure ZnO. In the ZnO–SiO<sub>2</sub> composite, the emission peak experiences a blue shift, suggesting a modification in the band structure or defect states due to the presence of SiO<sub>2</sub>. This shift may be attributed to quantum confinement effects or surface passivation, which influence the electronic transitions. In contrast, the ZnO–TiO<sub>2</sub> sample exhibits a red shift in its emission peak, indicating changes in defect levels or interfacial charge transfer dynamics between ZnO and TiO<sub>2</sub> that result in lower-energy photon emission.

The intensity of the PL signal also provides insight into the defect structure of the materials. A stronger PL emission is generally associated with a higher concentration of surface oxygen vacancies, crystal lattice defects, and surface hydroxyl groups. These structural features play a key role in determining the surface chemistry of the material, particularly influencing its hydrophilic or hydrophobic behavior. As reported in the literature [95], the presence of such defects enhances surface reactivity, making the wetting properties of the material more pronounced.

Overall, the PL analysis confirms that surface modification of ZnO with SiO<sub>2</sub> and TiO<sub>2</sub> not only alters the emission behavior but also affects the defect structure and surface functionality of the composite materials.

The UV–visible absorption spectra presented in Figure 4.15 compare the optical properties of pure ZnO and its doped composites with SiO<sub>2</sub> and TiO<sub>2</sub>. All samples exhibit a sharp absorption edge in the near-UV region, characteristic of ZnO, which corresponds to its intrinsic band gap transition. The absorption edge for pure ZnO is observed around 370 nm, consistent with a band gap energy of approximately 3.3 eV. This confirms the direct band gap nature of ZnO and its suitability for UV-active applications.

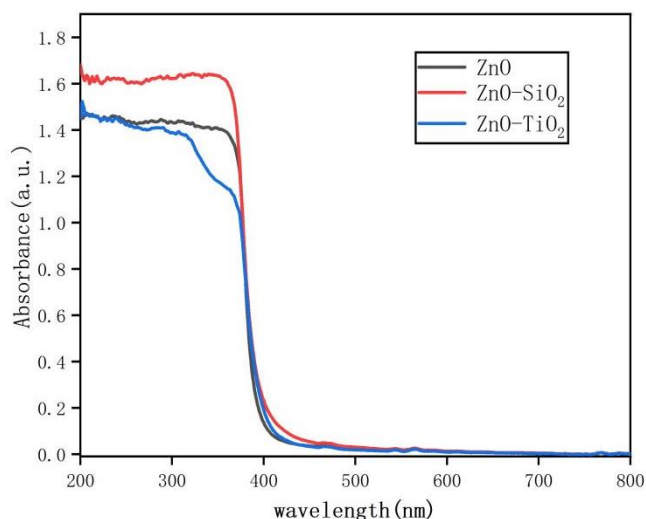


Figure 4.15 UV-visible spectra of ZnO and its doped composites

Upon doping with  $\text{SiO}_2$  and  $\text{TiO}_2$ , a slight red shift of the absorption edge is observed. The  $\text{ZnO-TiO}_2$  composite shows a more pronounced shift compared to  $\text{ZnO-SiO}_2$ , indicating a reduction in band gap energy. This effect can be attributed to the interaction between ZnO and the dopant oxides, which introduces defect levels or modifies the electronic structure of the host material. Additionally, both doped composites exhibit slightly lower absorbance in the UV region compared to pure ZnO, suggesting changes in surface states and light scattering due to the presence of amorphous or secondary phases. These spectral modifications imply that doping not only affects the electronic properties of ZnO but may also enhance its photocatalytic or optoelectronic performance.

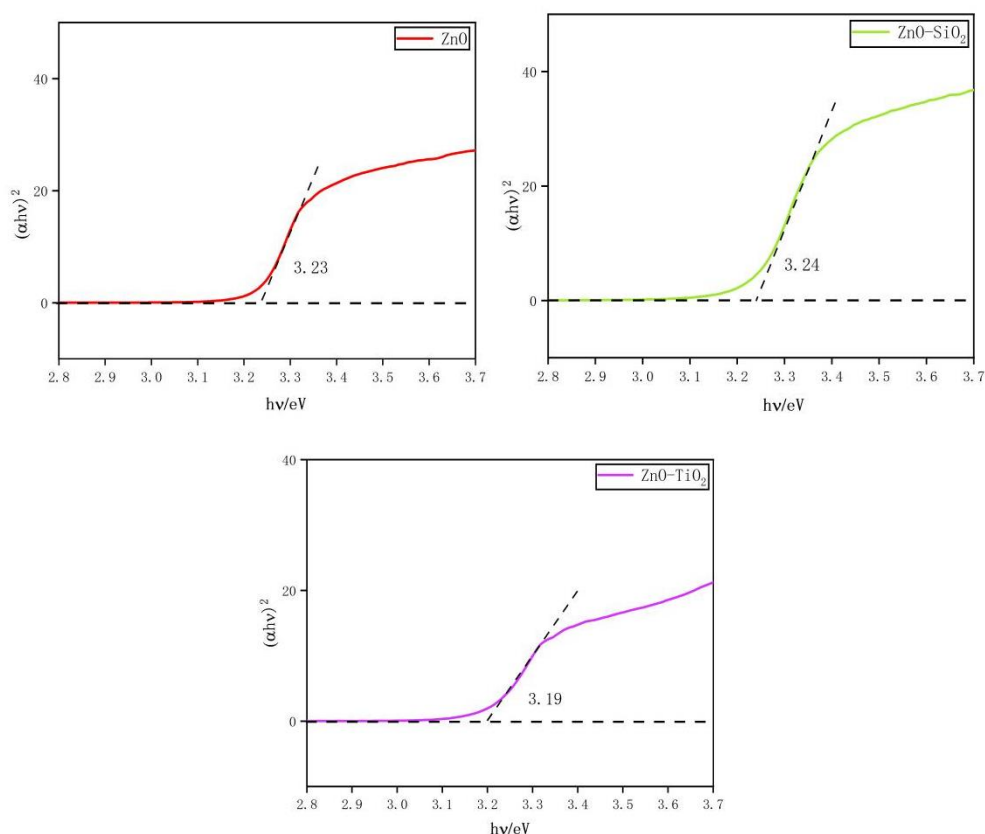


Figure 4.16 Band gap diagrams of ZnO and its doped composites

The band gap values of different samples can be obtained using the Kubelka-Munk formula ( $\alpha h\nu = A(h\nu - E_g)^{n/2}$ ). Figure 12 shows the band gap diagram of each sample after calculation. ZnO, ZnO-SiO<sub>2</sub> and ZnO-TiO<sub>2</sub> are 3.23 eV, 3.24 eV and 3.19 eV, respectively. After ZnO is doped with TiO<sub>2</sub>, the absorption edge of ZnO, which broadens the absorption range of ZnO for visible light and improves its absorption efficiency for visible light.

#### 4.3. Tuning of ZnO-TiO<sub>2</sub> composite particles morphology via oxides ratio

As with the previous samples, the ZnO-TiO<sub>2</sub> composites were characterized using the same methodological approach to assess particle morphology, chemical composition, and crystal structure features.

Figure 4.17 shows the XRD pattern of a ZnO/TiO<sub>2</sub> composite with a doping amount of Zn:Ti with a molar ratio of (2:1, 4:1, 10:1). The results show that the diffraction peaks at 2θ angles of 31.76°, 34.42°, 36.25° and 47.53° correspond to the hexagonal zinc blende ZnO (PDF#36-1451) structure. A characteristic peak of 25.318° appears at the 2θ angle of the diffraction peak, which corresponds to the characteristic peak of anatase TiO<sub>2</sub> (PDF#21-1272), and the corresponding crystal plane is (101).

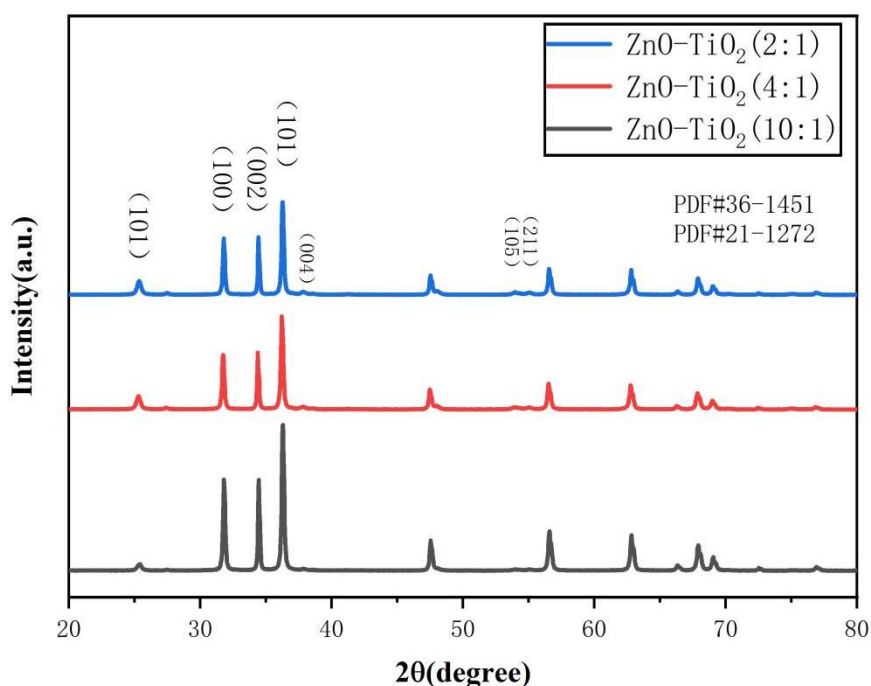


Figure 4.17 X-ray reflectogram of ZnO-SiO<sub>2</sub> composites with different oxides weight ratio

Moreover, with the increase of the doping amount of TiO<sub>2</sub>, the intensity of the corresponding anatase phase diffraction peak in the XRD spectrum increases, while the relative intensity of the main diffraction peak of ZnO will decrease decrease. However, ZnO still accounts for the majority, so its characteristic peaks can still be clearly observed.

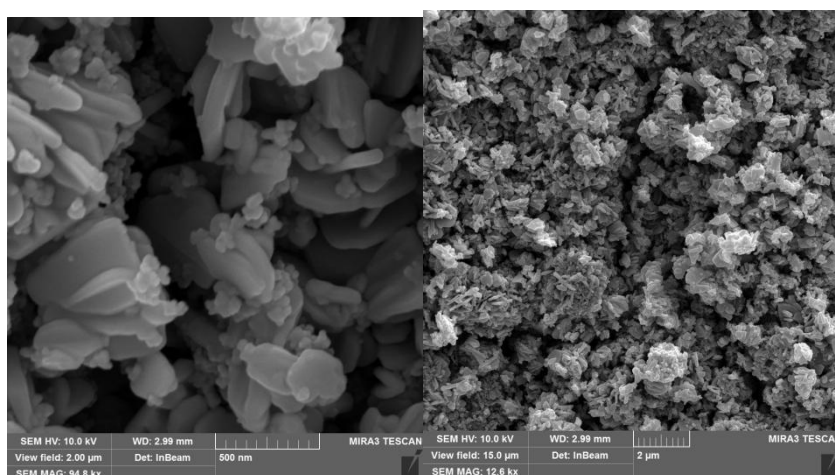
Figure 4.18 (a, b, c) presents the morphological features of ZnO-TiO<sub>2</sub> composite materials prepared with varying TiO<sub>2</sub> doping levels. Across all samples, the composite structure is composed of a heterogeneous mixture of flaky nanosheets and roughly

spherical nanoparticles, indicating the coexistence of distinct morphological phases within the material.

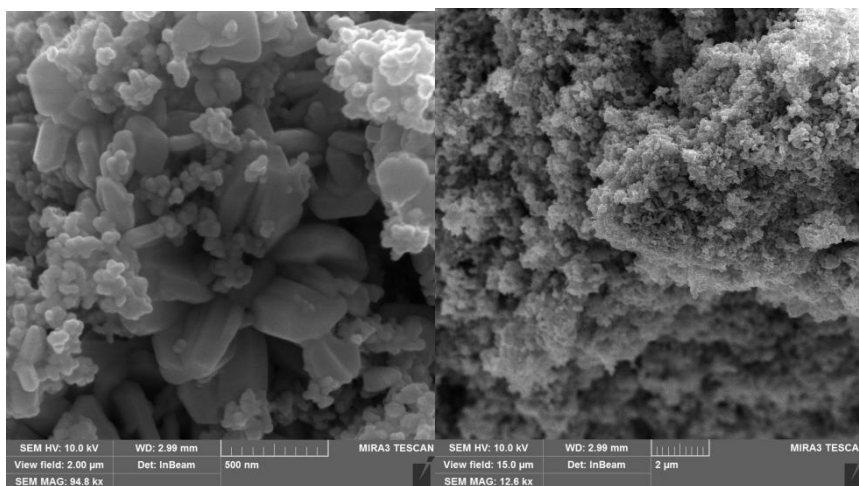
As the  $\text{TiO}_2$  doping concentration increases, a noticeable trend emerges: the proportion of smaller, spherical  $\text{TiO}_2$  nanoparticles within the composite becomes significantly higher. This increase in fine particle content leads to a denser packing of particles and a corresponding rise in particle aggregation throughout the sample. The nanosheets, which are characteristic of the ZnO component, remain present in all samples, but their surface is increasingly obscured by the accumulation of smaller  $\text{TiO}_2$  particles as doping levels rise.

This progressive agglomeration is likely driven by enhanced surface energy interactions and decreased interparticle spacing due to the higher density of nanoscale particles introduced by  $\text{TiO}_2$ . The resulting structures become more compact and less distinguishable at higher doping levels, which can adversely affect particle dispersion and surface area—two critical factors in applications such as catalysis, sensing, or surface wettability.

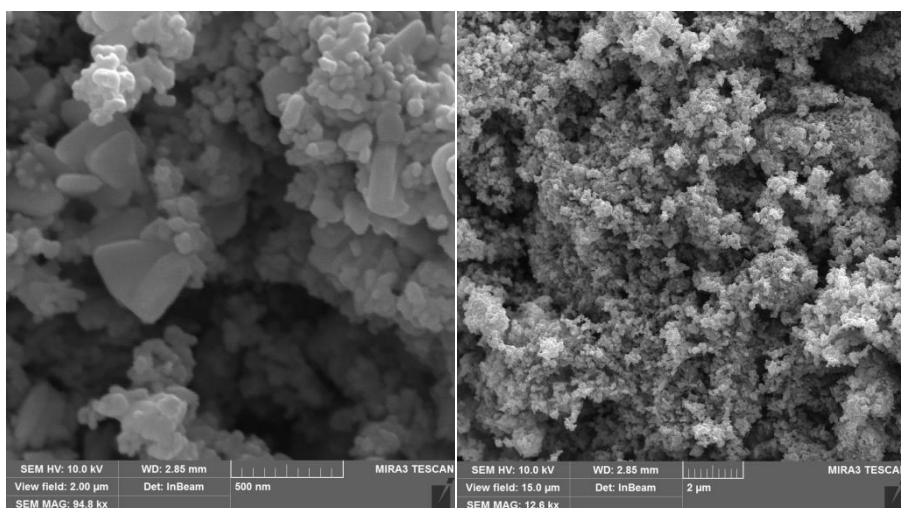
Overall, the microstructural evolution observed with increasing  $\text{TiO}_2$  content highlights the importance of doping concentration in tuning the morphology and dispersion behavior of ZnO– $\text{TiO}_2$  composites. Careful control of the  $\text{TiO}_2$  loading is thus essential to optimize material performance in target applications.



a



b



c

Figure 4.18 SEM images of ZnO-TiO<sub>2</sub> particles of oxide ratio: a – 10:1; b – 4:1; c – 2:1

Figure 4.18a displays the SEM image of the ZnO–TiO<sub>2</sub> composite with a mass ratio of 10:1. The image shows that TiO<sub>2</sub> nanoparticles are adsorbed onto the surface of the flaky ZnO. These TiO<sub>2</sub> particles are distributed either as isolated dots or in small agglomerated clusters on the ZnO flakes, yet they do not significantly alter the overall outline of the flake structures. Distinct, relatively flat ZnO flakes with well-defined edges and corners remain clearly visible.

Figure 4.18b presents the SEM image for the ZnO–TiO<sub>2</sub> composite with a ratio of 4:1. Compared to Figure 4.18a, the increased TiO<sub>2</sub> content results in a higher density

of  $\text{TiO}_2$  particles, which begin to form a continuous or partially aggregated coating on the surface. This leads to increased surface roughness of the flakes and a more pronounced aggregation of  $\text{ZnO}$  particles than observed in the previous sample.

Figure 4.18c shows the SEM image for the  $\text{ZnO-TiO}_2$  composite at a 2:1 ratio. At this higher doping level,  $\text{TiO}_2$  nanoparticles have largely covered the surface of the  $\text{ZnO}$  flakes. The flake-like  $\text{ZnO}$  morphology becomes increasingly stacked and less distinct. Nevertheless, the surface roughness of the composite is clearly greater than in the lower-doped samples.

At low  $\text{TiO}_2$  doping levels, the nanoparticles tend to distribute sparsely on the surface of  $\text{ZnO}$  flakes in a punctate or island-like pattern, which does not significantly alter the overall morphology. However, as the doping concentration increases,  $\text{TiO}_2$  particles accumulate to form more continuous or aggregated coatings. This leads to a pronounced roughening of the surface and, at sufficiently high doping levels, causes the  $\text{ZnO}$  flakes to become indistinct due to stacking and aggregation, making the individual structures more difficult to discern.

The optical properties of the prepared samples were studied using ultraviolet diffuse reflectance spectroscopy. Fig. 4.19 shows the ultraviolet-visible diffuse reflectance spectra of  $\text{ZnO-TiO}_2$  (2:1, 4:1, 10:1) samples with different doping ratios. All composite samples have strong absorption in the visible light region. The ultraviolet spectrum can visually show the light absorption properties of the material. It can be seen from the figure that the sample has a more obvious initial change in absorption near the 400 nm wavelength.

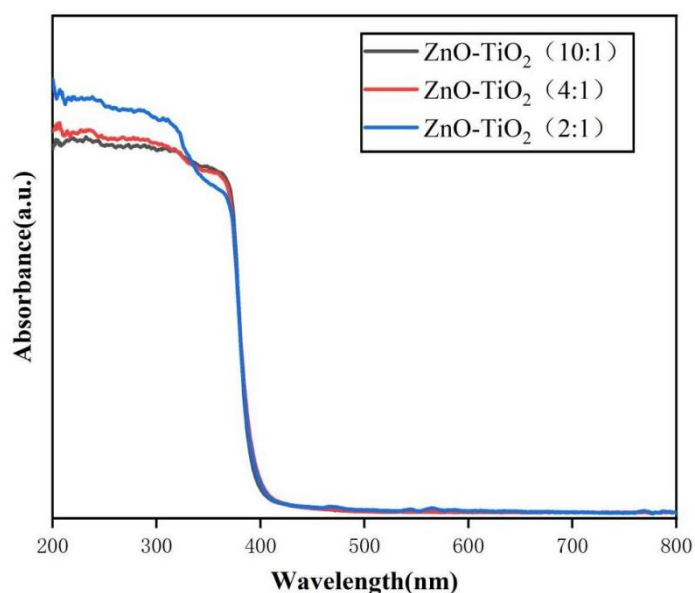


Figure 4.19 Ultraviolet-visible diffuse reflectance spectra of ZnO-TiO<sub>2</sub> composite particles

The band gap energy of semiconductors can be calculated using the Kubelka-Munk formula. Figure 4.20 shows the band gap diagram of each sample after calculation. The band gap energy of the ZnO-TiO<sub>2</sub>(2:1) sample is calculated to be about 3.21 eV, that of the ZnO-TiO<sub>2</sub>(4:1) sample is about 3.23 eV, and that of the ZnO-TiO<sub>2</sub>(10:1) sample is about 3.24 eV.

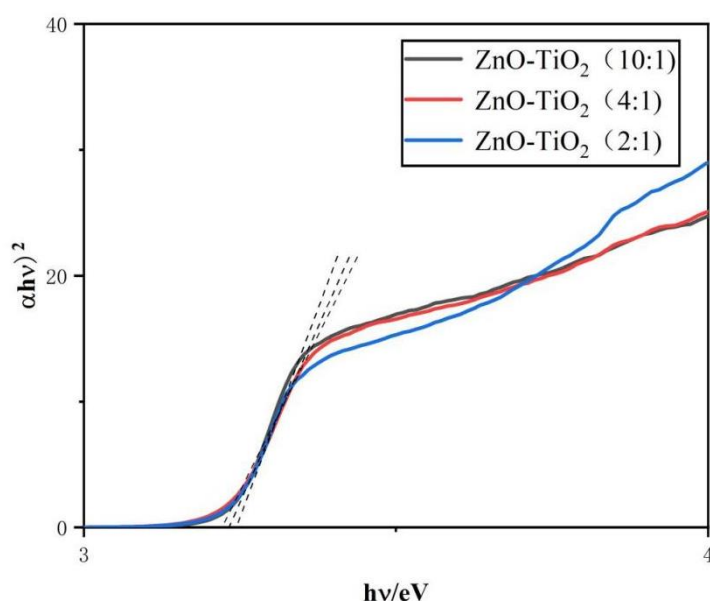


Figure 4.20 The band gap energy of ZnO-TiO<sub>2</sub> composites calculated via Kubelka-Munk equation

As shown in Figure 4.21, the PL spectra of the samples ZnO-TiO<sub>2</sub> (2:1), ZnO-TiO<sub>2</sub> (4:1) and ZnO-TiO<sub>2</sub> (10:1) are shown respectively. All samples have a strong emission peak near 565 nm. This phenomenon is caused by the energy released when electrons from the valence band jump to the conduction band, and then quickly recombine with the holes in the valence band. As the proportion of TiO<sub>2</sub> increases, the PL peak intensity decreases.

A lower photoluminescence (PL) peak intensity generally indicates a higher separation efficiency of photogenerated electron-hole pairs within a semiconductor catalyst, which is directly correlated with improved photocatalytic performance. PL spectral analysis reveals that both the TiO<sub>2</sub> nanomaterials and the TiO<sub>2</sub>/ZnO nanocomposites exhibit broad luminescence signals within the 350–550 nm wavelength range. The spectral trends of both materials are similar, suggesting that a low proportion of TiO<sub>2</sub> in the composite has minimal impact on the emission position of ZnO (Fig. 4.21).

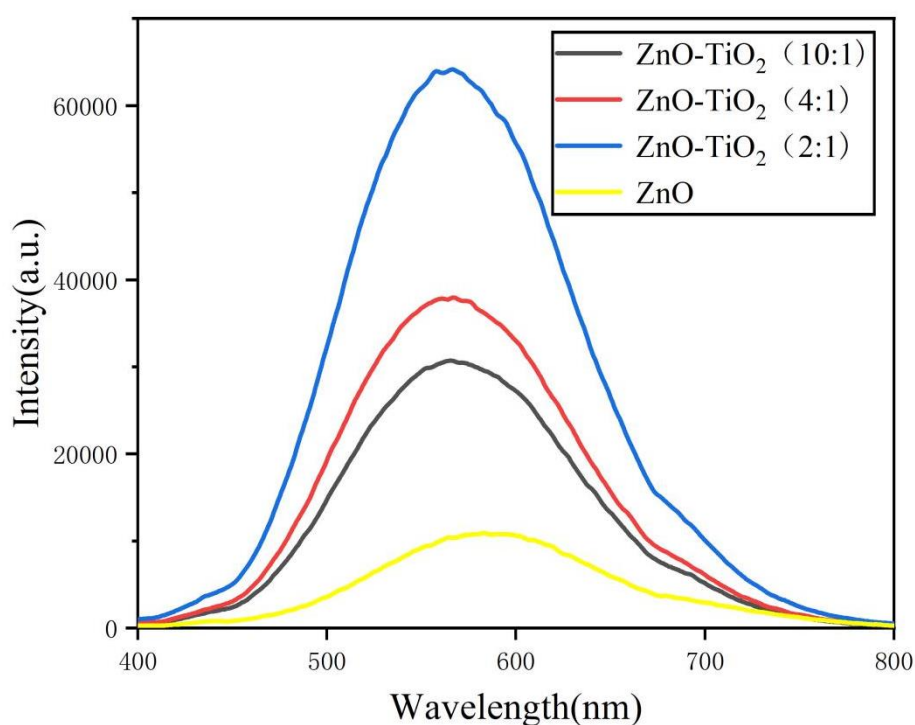


Figure 4.21 Photoluminescence spectra of ZnO-TiO<sub>2</sub> composites

As observed in the spectra, the PL intensity of the ZnO–TiO<sub>2</sub> nanocomposite is lower than that of pure ZnO, indicating a suppression of electron–hole recombination due to the interaction between ZnO and TiO<sub>2</sub>. This reduction in luminescence intensity can be attributed to the formation of heterojunctions between the two semiconductors, which facilitate charge carrier separation.

It is well established that the PL emission of semiconductor materials originates from the recombination of photogenerated electron–hole pairs. Therefore, a weaker PL signal typically reflects a lower recombination rate, which enhances the material's photoelectric conversion efficiency [96].

Given the similar bandgap energies of ZnO (3.3 eV) and TiO<sub>2</sub> (3.2 eV), the formation of a heterojunction between them leads to favorable band alignment. In this structure, electrons excited to the conduction band (CB) of ZnO can transfer to the CB of TiO<sub>2</sub>, while holes from the valence band (VB) of TiO<sub>2</sub> can migrate to the VB of ZnO. This bidirectional charge transfer significantly reduces the recombination of photogenerated carriers and increases the quantum efficiency of the material.

As a result, the TiO<sub>2</sub>/ZnO nanocomposites exhibit potentially enhanced photocatalytic activity compared to pure ZnO nanomaterials. Additionally, this heterojunction structure can influence the surface chemistry of the composite, contributing to modifications in its hydrophilic or hydrophobic behavior -an important factor in the performance of hydrophobic coatings.

## Conclusions to chapter 4

The study has demonstrated that the morphology of ZnO particles can be effectively tuned by adjusting hydrothermal synthesis parameters, such as the type and concentration of the alkaline catalyst and reaction temperature. Using NaOH favors the formation of smooth, flaky nanosheets, while increasing its concentration promotes rod-like morphologies due to accelerated anisotropic growth along the [0001] axis. In contrast, the use of NH<sub>4</sub>OH leads to more complex structures, including flower-like and hollow hexagonal prisms, with temperature playing a crucial role in determining the final morphology.

In addition to synthesis conditions, doping with TiO<sub>2</sub> and SiO<sub>2</sub> proved to be a powerful tool for further morphological and structural modification. TiO<sub>2</sub> was found to adhere to the surface of ZnO flakes and induce more compact and aggregated forms, possibly due to surface interaction or lattice distortion. SiO<sub>2</sub>, on the other hand, formed a loosely bound amorphous matrix without disrupting the original sheet-like ZnO structure, thus preserving the nanosheet morphology while introducing surface heterogeneity.

Characterization techniques, including SEM, TEM, XRD, and EDS, confirmed the structural purity of the synthesized materials, as well as the successful incorporation of dopants. Photoluminescence and UV–vis spectroscopy revealed changes in defect structures and optical properties upon doping, further confirming the sensitivity of ZnO's electronic structure to morphological and compositional modifications.

Among the tested materials, the ZnO–TiO<sub>2</sub> composite demonstrates the most promising features for further development of superhydrophobic coatings. Its hierarchically rough surface, composed of ZnO flakes coated with TiO<sub>2</sub> nanoparticles, creates the dual-scale texture necessary for achieving strong water repellency through the Cassie–Baxter effect. The presence of both crystalline phases and favorable interfacial contact further supports its potential as a functional layer for advanced surface engineering applications.

**The results of this chapter were published in:**

1. Wang, M.; **Li, C.**; Liu, B.; Qin, W.; Xie, Y. Influence of calcination temperature on photocatalyst performances of floral  $\text{Bi}_2\text{O}_3/\text{TiO}_2$  composite. *Catalysts* **2022**, *12* (12), 1635. [10.3390/catal12121635](https://doi.org/10.3390/catal12121635). ISSN 2073-4344
2. Wang, M.; **Li, C.**; Liu, B.; Qin, W.; Xie, Y. Facile synthesis of Nano-Flower  $\text{Bi}_2\text{O}_3/\text{TiO}_2$  heterojunction as photocatalyst for degradation RHB. *Molecules* **2023**, *28* (2), 882. [10.3390/molecules28020882](https://doi.org/10.3390/molecules28020882). ISSN 1420-3049
3. Li, C.; Myronyuk, O.; Bilousova, A.; Pitak, Y. Synthesis and characterization of Zn-based ceramic particles with controlled morphology. *Scientific Research on Refractories and Technical Ceramics* **2024**, No. 124, 104–110. [10.35857/2663-3566.124.11](https://doi.org/10.35857/2663-3566.124.11). ISSN 2663-3566
4. Myronyuk, O., Che, L., Bilousova, A., & Pitak, Y. (2024). Zinc Oxide Based Particles with Hierarchical Structure for Surface Wetting Modification (pp. 1–4). [10.1109/khpiweek61434.2024.10878067](https://doi.org/10.1109/khpiweek61434.2024.10878067)

## **CHAPTER 5. ORGANO-MINERAL COATINGS OBTAINING AND CHARACTERIZATION**

### 5.1. Dependence of wetting properties of textured coatings on the filler particles content and type

In this chapter, stable zinc oxide (ZnO) and silica–zinc oxide (SiO<sub>2</sub>–ZnO) composite particles were synthesized through a facile chemical precipitation technique performed at ambient temperature. This method allowed the formation of nanoscale particles with enhanced physicochemical characteristics, which are crucial for subsequent integration into polymer-based surface coatings. A total of four distinct filler materials were utilized in the preparation of these coatings: titanium dioxide (TiO<sub>2</sub>), silicon dioxide (SiO<sub>2</sub>), pure ZnO, and a hybrid ZnO–SiO<sub>2</sub> composition. Following synthesis, a detailed evaluation of the coatings' surface morphology and wettability properties was conducted in order to assess their structural integrity and functional performance.

The primary aim of this section is to investigate how the incorporation of various types of inorganic nanoparticles—namely TiO<sub>2</sub>, SiO<sub>2</sub>, and the synthesized ZnO and SiO<sub>2</sub>–ZnO—affects the water contact angle of styrene-butyl methacrylate-based composite coatings. Understanding the influence of nanoparticle composition on surface wettability is essential for applications requiring precise control of hydrophilic or hydrophobic behavior.

For the fabrication of the coatings, a styrene-arene copolymer was employed as the organic matrix. This polymer was first dissolved in xylene at a mass ratio of 1:5 (polymer to solvent) to ensure complete homogenization. Upon full dissolution, predetermined amounts of inorganic particles were added to the polymer solution in specific weight ratios: SiO<sub>2</sub> (ranging from 0% to 40%), TiO<sub>2</sub> (20% to 95%), ZnO (20% to 80%), and ZnO–SiO<sub>2</sub> (20% to 80%). The resulting suspensions were uniformly applied onto glass slides with dimensions of 2.5 cm × 1 cm × 0.02 cm, using a casting method, and were subsequently dried at 55 °C for 10 minutes to obtain solid nanocomposite films.

Fig. 5.1 presents a microscopic image of the TiO<sub>2</sub>-based coating, revealing the morphology of the embedded nanoparticles. The particle size was estimated to be in the range of approximately 25–50 nm. Notably, the image demonstrates a pronounced tendency for particle aggregation within the nanocomposite film, which can be attributed to the inherently high surface energy of TiO<sub>2</sub> nanoparticles. These aggregates are likely composed of both pure TiO<sub>2</sub> agglomerates and clusters encapsulated by the acrylic polymer during the drying process. Such agglomeration behavior is characteristic of nanoparticles with strong interparticle interactions and insufficient steric stabilization in the polymer matrix.

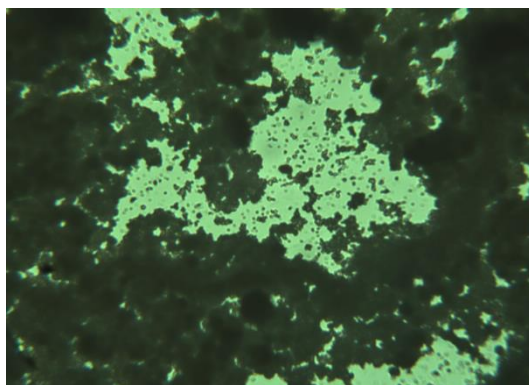
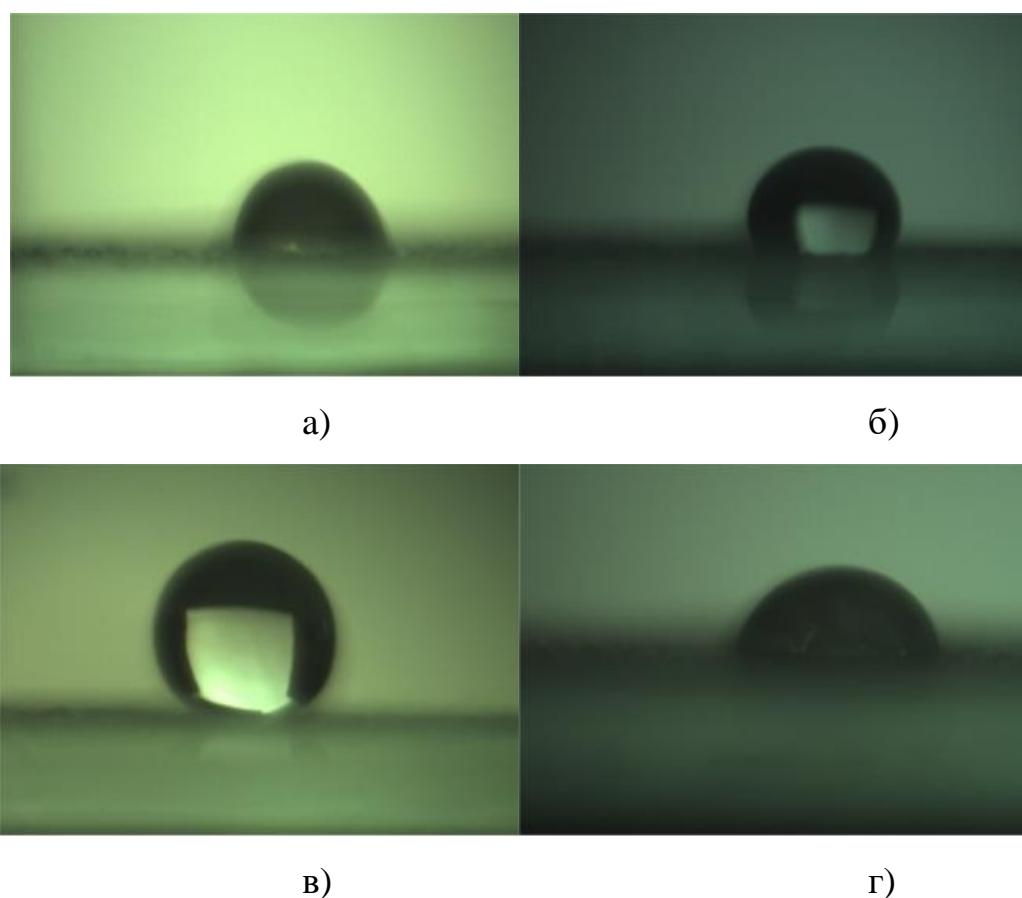


Figure 5.1. Morphology of TiO<sub>2</sub> filled coatings

Following the uniform deposition of the composite coating onto the glass substrate, the wettability of the modified surfaces was evaluated by measuring the static water contact angle. This parameter serves as a key indicator of surface hydrophilicity or hydrophobicity and is widely used to characterize interfacial interactions between water droplets and solid materials. As illustrated in Figure 5.2, the variation in TiO<sub>2</sub> content within the coating formulation had a non-linear effect on the contact angle behavior. Specifically, with increasing mass fraction of TiO<sub>2</sub>, the water contact angle initially increased, indicating enhanced surface hydrophobicity. However, beyond a certain concentration threshold, the contact angle began to decline, suggesting a reversal in wetting behavior.

This trend reflects the complex interplay between surface roughness introduced by  $\text{TiO}_2$  nanoparticles and the chemical composition of the coating's outermost layer. At lower concentrations,  $\text{TiO}_2$  particles may increase the nanoscale roughness of the surface, thereby amplifying hydrophobic effects through the Cassie–Baxter mechanism. Conversely, excessive  $\text{TiO}_2$  loading likely exposes more hydroxyl groups or creates defects in the surface structure, resulting in increased affinity for water molecules and, consequently, reduced contact angles.



**Рис. 2. Кут контакту покриття при різному вмісті  $\text{TiO}_2$ : а) 20%; б) 40%; в) 80%; г) 85%**

Table 5.1 presents the measured water contact angles for  $\text{TiO}_2$ -containing coatings at varying mass fractions of the filler. At the lowest concentration examined, the contact angle was recorded at  $73.6^\circ$ , a value that closely corresponds to that of the

unmodified styrene–acrylic polymer coating. This suggests that at low TiO<sub>2</sub> content, the nanoparticle loading is insufficient to significantly alter the surface energy or topography of the composite film.

As the TiO<sub>2</sub> content increases and approaches approximately 80 wt%, the contact angle reaches a maximum of 149.3°, which is indicative of a transition toward superhydrophobic behavior. This significant increase is primarily attributed to the enhanced surface roughness induced by the uniform distribution of TiO<sub>2</sub> nanoparticles, which act as topographical features that reduce the solid–liquid contact area. The observed wetting behavior aligns well with the Cassie–Baxter model [97], which describes the apparent contact angle on rough surfaces as a function of both the intrinsic hydrophobicity of the material and the air-trapping microstructure formed on the surface.

However, when the TiO<sub>2</sub> concentration is further increased beyond the optimal point, a gradual decline in the contact angle is observed. This decrease can be explained by the overaccumulation of TiO<sub>2</sub> particles, which may lead to excessive exposure of surface hydroxyl groups. These groups are highly hydrophilic and capable of forming hydrogen bonds with water molecules, thereby increasing the overall surface energy and promoting wetting. Additionally, the formation of densely packed TiO<sub>2</sub> agglomerates at high concentrations may reduce the uniformity of surface roughness, thus diminishing the hydrophobic effect initially achieved (Table 5.1.).

Table 5.1 - Contact angle of TiO<sub>2</sub> filled coatings

| %  | WCA of<br>TiO <sub>2</sub> |
|----|----------------------------|
| 20 | 73,8                       |
| 40 | 120                        |
| 60 | 135,3                      |
| 80 | 149,3                      |

|    |      |
|----|------|
| 85 | 72,3 |
| 90 | 76   |
| 95 | 71,2 |

Figure 5.3 displays a high-resolution micrograph illustrating the micromorphology of the SiO<sub>2</sub>-based coating. The surface of the nanocomposite film modified with SiO<sub>2</sub> particles is characterized by a pronounced smoothness and a uniform texture. The microstructure reveals a densely packed arrangement of nearly monodisperse spherical particles, which are distributed across the surface with high regularity.

Notably, the SiO<sub>2</sub> particles exhibit minimal signs of agglomeration, suggesting effective dispersion within the polymer matrix. The absence of large clusters or irregular aggregates implies strong interfacial compatibility between the silica nanoparticles and the organic phase, potentially enhanced by favorable interactions during film formation. The particles have an estimated diameter in the range of approximately 5 to 30 nanometers, contributing to the formation of a nanostructured surface with fine-scale textural uniformity.

This type of morphology is advantageous for applications requiring stable surface properties, as the smoothness and homogeneity minimize variability in interfacial interactions. Furthermore, the consistent particle size distribution ensures that the surface energy landscape remains predictable, which can have a direct impact on wettability, optical clarity, and other functional characteristics of the coating.

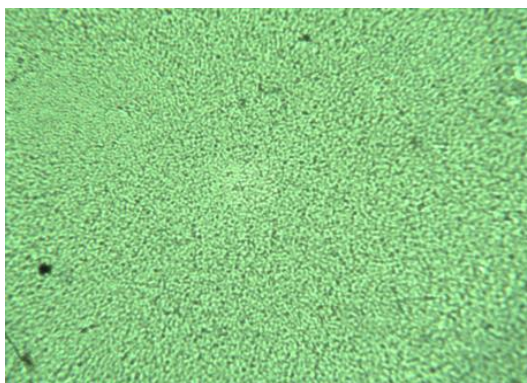


Figure. 5.3 Morphology of SiO<sub>2</sub> filled coating

As shown in Figure 5.4, the variation in the mass fraction of SiO<sub>2</sub> within the coating formulation significantly influences the wettability characteristics of the glass surface. Specifically, the measured water contact angle exhibits a non-monotonic trend: it initially increases with rising SiO<sub>2</sub> content, reaching a peak value, and subsequently decreases when the silica loading becomes excessive. This behavior indicates that a moderate concentration of SiO<sub>2</sub> particles enhances hydrophobicity, likely due to optimized surface roughness and low surface energy regions created by the well-dispersed nanoparticles.

However, at a mass fraction of approximately 40%, distinct physical defects such as surface cracking and peeling are observed in the coating. These structural anomalies may be attributed to the overloading of the polymer matrix with silica nanoparticles. At such high concentrations, the polymeric phase likely becomes insufficient to uniformly encapsulate and bind all the particles, leading to poor interfacial adhesion and mechanical instability upon drying.

Moreover, the excessive presence of rigid inorganic particles may introduce internal stresses during solvent evaporation and thermal curing, further contributing to film delamination and crack formation. These morphological defects compromise both the visual appearance and functional performance of the coating and highlight the importance of balancing nanoparticle content to maintain structural coherence while optimizing surface properties.

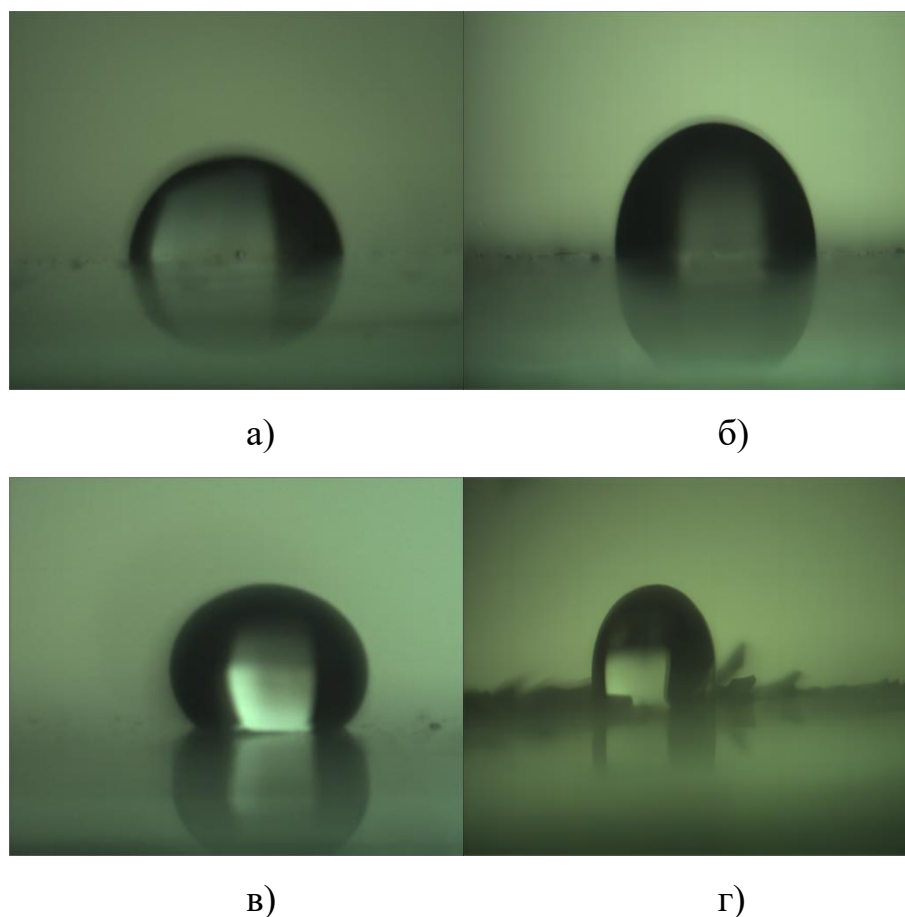


Figure 5.4 Static water contact angles of SiO<sub>2</sub>-modified coatings at different filler loadings: (a) 3 wt%; (b) 15 wt%; (c) 30 wt%; (d) 40 wt%.

Table 5.2 summarizes the measured water contact angles for coatings modified with varying mass fractions of SiO<sub>2</sub>. At low silica concentrations, specifically below 9 wt%, the changes in contact angle are minimal and fall within the range of experimental uncertainty. This suggests that the addition of small amounts of SiO<sub>2</sub> does not significantly alter the surface morphology or energy of the coating.

As the SiO<sub>2</sub> content increases to between 9 wt% and 30 wt%, a clear upward trend in the contact angle is observed. This indicates a progressive enhancement in hydrophobic behavior, which can be attributed to the development of micro- and nanoscale surface textures resulting from well-dispersed silica nanoparticles. These

topographical features reduce the effective contact area between water droplets and the surface, in accordance with the Cassie–Baxter wetting model.

The contact angle reaches its maximum value of 125.5° at a SiO<sub>2</sub> loading of 30 wt%, reflecting a substantial increase in surface hydrophobicity. This level of wettability is indicative of a partially water-repellent surface, although it does not reach the superhydrophobic regime. Beyond this optimal concentration, however, further increases in SiO<sub>2</sub> content lead to a gradual decline in the contact angle. This decline may be attributed to the onset of particle aggregation, surface cracking, or disruption in the continuity of the polymer matrix, all of which negatively impact the surface's ability to repel water.

Table 5.2 – Water contact angle of organo-mineral composites filled with SiO<sub>2</sub>

| %  | WCA, ° |
|----|--------|
| 0  | 73,8   |
| 3  | 74,3   |
| 6  | 74     |
| 9  | 78,5   |
| 15 | 77,1   |
| 20 | 96,8   |
| 25 | 88     |
| 30 | 125,5  |
| 40 | 109    |

Figure 5.5 presents the micromorphological characteristics of the nanocomposite film containing zinc oxide (ZnO) as the functional filler. Surface analysis reveals that the coating exhibits a relatively smooth overall texture; however, localized agglomeration of ZnO nanoparticles is also evident. This phenomenon is commonly associated with the intrinsic surface energy of ZnO, which promotes particle–particle interactions and the formation of aggregates during the film formation process.

These small-scale agglomerates are believed to form primarily during solvent evaporation, a stage at which the mobility of nanoparticles decreases and capillary forces drive them into densely packed clusters. As a result, isolated accumulations of ZnO can be observed on the coating surface. The estimated diameter of these agglomerates ranges from approximately 500 to 1000 nanometers, which is significantly larger than the individual particle size and indicative of partial instability in nanoparticle dispersion within the polymer matrix.

Although the ZnO-filled film retains a degree of surface smoothness, the presence of such agglomerates may locally disrupt uniformity and alter surface functionality. This behavior highlights the challenges of achieving stable dispersion of metal oxide nanoparticles in organic matrices without the aid of surface modification or dispersing agents. Understanding and controlling such aggregation phenomena is crucial for tailoring the final surface properties of ZnO-based nanocomposite coatings.

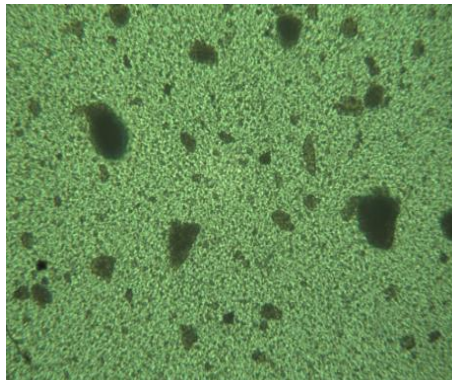
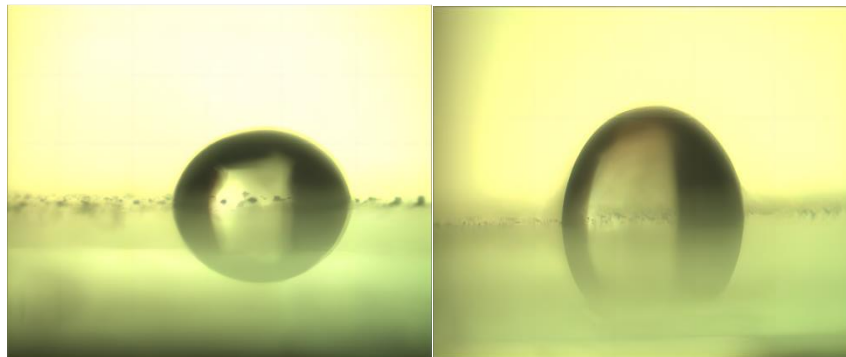


Fig. 5.5 Morphology of ZnO filled coating

Figure 5.6 shows the variation in static water contact angles for ZnO-modified coatings at four different mass fractions: 20%, 40%, 60%, and 80%. The procedures used for sample preparation and measurement were consistent with those employed in the previous experiments to ensure comparability of results across different nanoparticle systems.

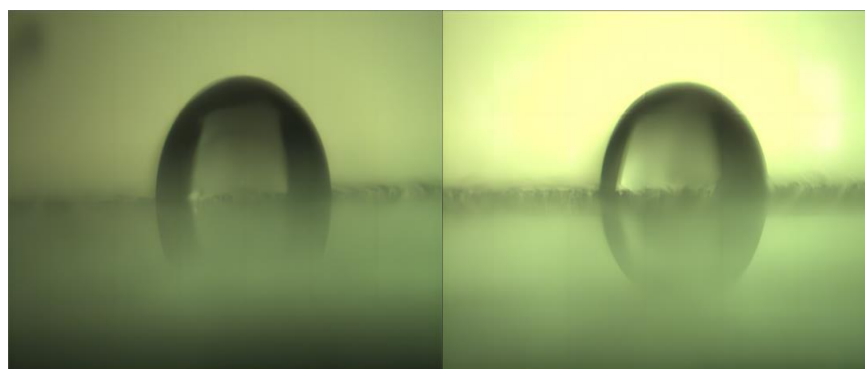
The contact angle data indicate a weakly nonlinear trend with respect to ZnO content. Specifically, as the concentration of ZnO increases, the water contact angle initially rises, reaching a modest peak, and then gradually decreases. However, the overall amplitude of variation in contact angle across the full composition range is relatively small, suggesting that the addition of ZnO does not lead to substantial changes in the surface wettability of the coating.

This subtle behavior may be explained by the limited influence of ZnO particles on both surface roughness and chemical composition at the water–solid interface. Unlike  $\text{TiO}_2$  or  $\text{SiO}_2$ , ZnO nanoparticles may not contribute significantly to nanoscale surface texturing, particularly if they tend to form larger agglomerates, as previously observed. Furthermore, the surface energy of ZnO may not differ markedly from that of the polymer matrix, leading to a more muted effect on hydrophobicity or hydrophilicity as a function of filler loading.



a)

b)



B)

Г)

Figure 5.6 - Static water contact angles of ZnO-based coatings at various filler loadings: (a) 20 wt%; (b) 40 wt%; (c) 60 wt%; (d) 80 wt%.

Table 5.3 presents the experimentally measured water contact angles for ZnO-modified coatings as a function of filler mass fraction. The highest contact angle, recorded at 74.8°, was observed when the ZnO content reached 60 wt%. Despite this peak, the overall variation in contact angle remains relatively small across the entire composition range, and the observed values are only marginally different from those of the unmodified B880 polymer matrix.

This suggests that the incorporation of ZnO nanoparticles has no significant effect on the hydrophobic properties of the base coating. In particular, the slight increase in contact angle does not indicate a meaningful enhancement in water-repellent behavior. A plausible explanation for this limited impact lies in the fact that ZnO addition does not appreciably alter the surface roughness of the coating, which is a key factor influencing wettability.

According to the literature [98], meaningful changes in hydrophobicity typically require either substantial modifications in surface energy or the introduction of hierarchical surface textures at the micro- and nanoscale. In the case of ZnO, the tendency to form localized agglomerates without generating a uniform rough surface may prevent such effects from manifesting. Therefore, while ZnO contributes certain functional benefits in other contexts, its influence on surface wettability in this particular formulation appears minimal.

Table 5.3 – Water contact angle of organo-mineral composites filled with ZnO

| %  | WCA, ° |
|----|--------|
| 20 | 69     |
| 40 | 71,8   |

|    |      |
|----|------|
| 60 | 74,8 |
| 80 | 71,3 |

Figure 5.7 depicts the micromorphological structure of the ZnO–SiO<sub>2</sub>-based composite coating. The surface analysis reveals the presence of well-defined agglomerates consisting of ZnO–SiO<sub>2</sub> hybrid particles. These agglomerates are of moderate size, and the overall particle dispersion is relatively uniform across the examined area. Unlike coatings with excessive aggregation or poor distribution, the surface of the ZnO–SiO<sub>2</sub>-modified film appears comparatively well-organized and structurally coherent.

The presence of ZnO in the composite system is a key factor influencing the resulting morphology. Compared to coatings modified with pure SiO<sub>2</sub>, the addition of ZnO alters the interparticle interactions and surface energetics, promoting partial aggregation. This phenomenon is commonly observed in metal oxide systems with elevated surface energy. In particular, ZnO tends to increase the likelihood of particle agglomeration due to its strong polar surface characteristics and high affinity for forming interfacial bonds.

The observed structural organization suggests a balance between dispersion and clustering, likely governed by the competition between van der Waals forces and steric hindrance from the surrounding polymer matrix. According to prior studies [99], such moderate aggregation can be expected in mixed-oxide systems where differential surface charges and interaction potentials result in partial phase self-association. As a result, the ZnO–SiO<sub>2</sub> coating achieves a surface morphology that is more ordered than that of ZnO alone, while still distinct from the highly uniform particle layout observed in pure SiO<sub>2</sub>-based films.

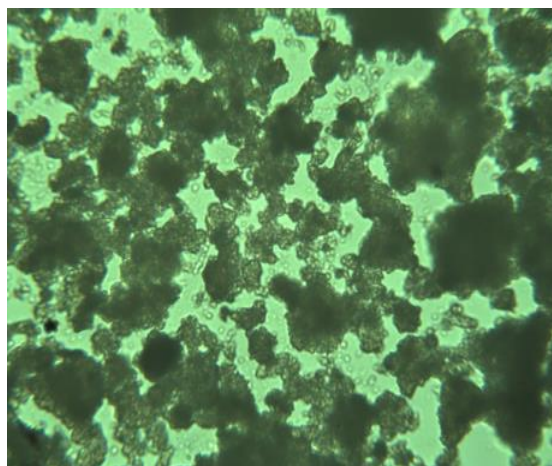
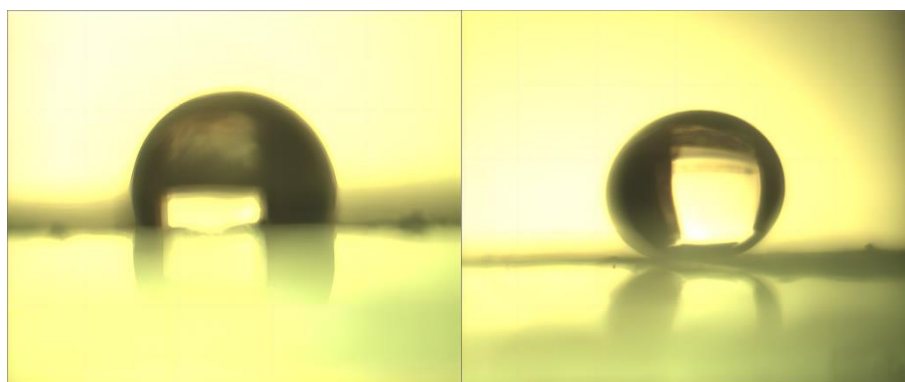


Figure 5.7 Surface morphology of the composite coating containing ZnO–SiO<sub>2</sub> hybrid nanoparticles.

Figure 5.8 illustrates the variation in water contact angle measurements for ZnO–SiO<sub>2</sub>-modified coatings at different filler concentrations: 20%, 60%, 70%, and 80% by weight. These images provide visual confirmation of the changes in surface wettability as a function of increasing hybrid nanoparticle loading.

According to the data presented in Table 5.4, the contact angle of water on the ZnO–SiO<sub>2</sub>-modified coatings exhibits a non-monotonic dependence on the mass fraction of the hybrid filler. As the ZnO–SiO<sub>2</sub> content increases, the contact angle initially rises, reaching a maximum value at an intermediate composition, and then gradually declines at higher loadings.



a)

b)

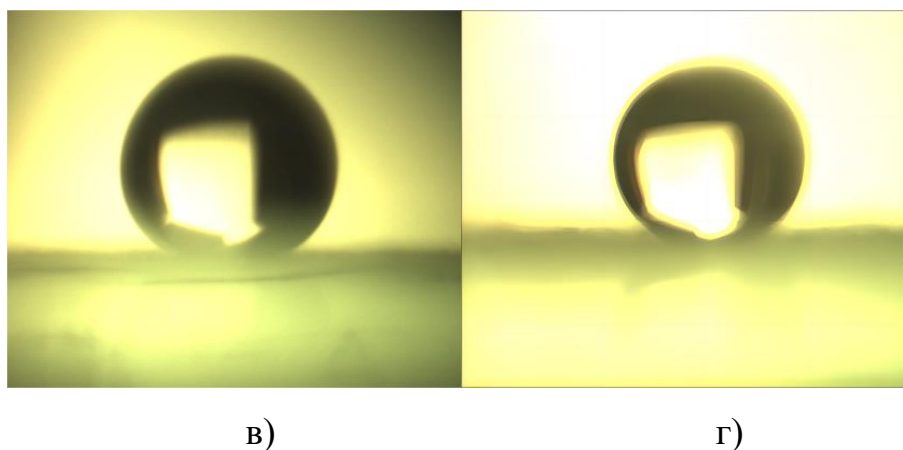


Figure 5.8 Static water contact angles of ZnO–SiO<sub>2</sub>-based coatings at varying mass fractions: (a) 20 wt%; (b) 60 wt%; (c) 70 wt%; (d) 80 wt%.

Notably, the highest contact angle-152.5°-is achieved at a filler concentration of 60 wt%. This value exceeds the conventional threshold of 150° used to classify surfaces as superhydrophobic. Such behavior indicates that, at this specific composition, the coating surface combines both optimal roughness and low surface energy, resulting in minimized interaction with water droplets. The Cassie–Baxter wetting regime is likely dominant in this case, as air pockets formed within the surface texture reduce the contact area between water and solid.

The subsequent decrease in contact angle at higher filler contents may be attributed to excessive particle aggregation or disruption of the micro-/nanostructured surface, which can compromise the superhydrophobic effect. These findings highlight the critical role of particle loading in fine-tuning the wettability of hybrid nanocomposite surfaces and demonstrate that ZnO–SiO<sub>2</sub> systems offer promising potential for the fabrication of superhydrophobic coatings.

Table 5.4 – Water contact angle of organo-mineral composites filled with **ZnO-SiO<sub>2</sub>**

| %  | WCA, ° |
|----|--------|
| 20 | 119,5  |
| 40 | 135,2  |

|    |       |
|----|-------|
| 60 | 152,5 |
| 65 | 144,8 |
| 70 | 139,6 |
| 75 | 139,8 |
| 80 | 133,5 |

Figure 9 presents a comparative histogram illustrating the measured water contact angles for coatings modified with four different types of nanoparticles:  $\text{TiO}_2$ ,  $\text{SiO}_2$ ,  $\text{ZnO}$ , and  $\text{ZnO-SiO}_2$ . This visualization enables a direct assessment of the relative hydrophobic performance of each composite system.

Among all tested formulations, the  $\text{ZnO-SiO}_2$ -based coating exhibits the highest degree of hydrophobicity, achieving a contact angle exceeding  $150^\circ$ , which qualifies it as superhydrophobic according to widely accepted classification criteria. This superior performance is attributed to the synergistic interaction between the  $\text{ZnO}$  and  $\text{SiO}_2$  components, which promotes the formation of a hierarchical surface structure favorable for water repellency.

The  $\text{TiO}_2$ -modified coating, at a filler concentration of 80 wt%, also demonstrates a high contact angle that closely approaches the superhydrophobic threshold, indicating strong water-repellent behavior under optimized conditions. In contrast, coatings incorporating only  $\text{ZnO}$  or  $\text{SiO}_2$  show considerably lower contact angles and thus exhibit less pronounced hydrophobic characteristics.

Overall, the data confirm that hybridization of oxide fillers—specifically the combination of  $\text{ZnO}$  and  $\text{SiO}_2$ —results in enhanced surface properties that outperform those achieved by using the individual components alone. These findings underline the potential of  $\text{ZnO-SiO}_2$  systems for engineering advanced functional surfaces with exceptional wetting control.

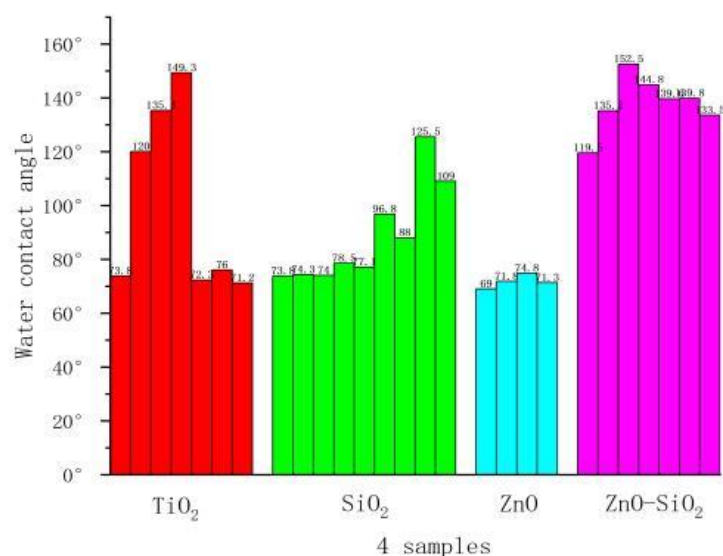


Figure 5.9 Comparison of water contact angles for composite coatings containing different nanoparticle fillers: TiO<sub>2</sub>, SiO<sub>2</sub>, ZnO, and ZnO–SiO<sub>2</sub>.

In summary, ZnO and ZnO–SiO<sub>2</sub> nanoparticles were successfully synthesized via a simple one-step chemical precipitation method performed under ambient conditions. These synthesized particles, along with commercially available TiO<sub>2</sub> and SiO<sub>2</sub>, were subsequently incorporated into styrene–butyl methacrylate (SBMA) polymer matrices to fabricate a series of composite coatings. Each formulation was evaluated in terms of its surface morphology and wettability behavior.

The contact angle measured for the unmodified SBMA polymer coating was 73.6°, which reflects the inherently low hydrophilicity of the butyl ester group in the SBMA structure. The presence of this functional group reduces the surface energy of the film, resulting in moderate hydrophobicity [100]. This value served as the baseline for comparison with nanoparticle-enhanced coatings.

Optical microscopy revealed that the addition of all four types of nanoparticles led to the formation of localized agglomerates on the surface of the coatings. These aggregates contributed to an increase in surface roughness, which plays a critical role in modulating the wetting behavior. Notably, for all particle systems except ZnO, increasing the filler content led to a significant rise in the water contact angle, indicating a transition toward more hydrophobic surfaces. This enhancement can be

attributed to the synergistic effect of increased surface roughness and the inherently low surface energy introduced by the nanoparticulate additives.

Collectively, the results demonstrate that the wetting properties of SBMA-based nanocomposite coatings can be effectively tuned through careful selection and optimization of filler type and concentration. The ZnO–SiO<sub>2</sub> hybrid system, in particular, shows great promise for applications requiring superhydrophobic or water-repellent surfaces.

The next stage of the study involved comparing the effectiveness of the particles synthesized in Chapter 4—specifically, zinc oxide doped with titanium dioxide (the most promising variant) and zinc oxide doped with silicon dioxide—on the water-repellent properties of systems based on sodium styrene-butyl methacrylate copolymers.

As shown in Figure 5.9, the relationship between the particle content in the thin coatings and the water contact angle (WCA) exhibits a similar trend across all investigated materials. Specifically, in the range from pure polymer films up to a particle loading of approximately 40–60 wt.%, the measured WCA values remain relatively constant and fall within the experimental error margins. This suggests that, within this concentration interval, the incorporation of particles does not significantly influence the surface wettability of the coatings.

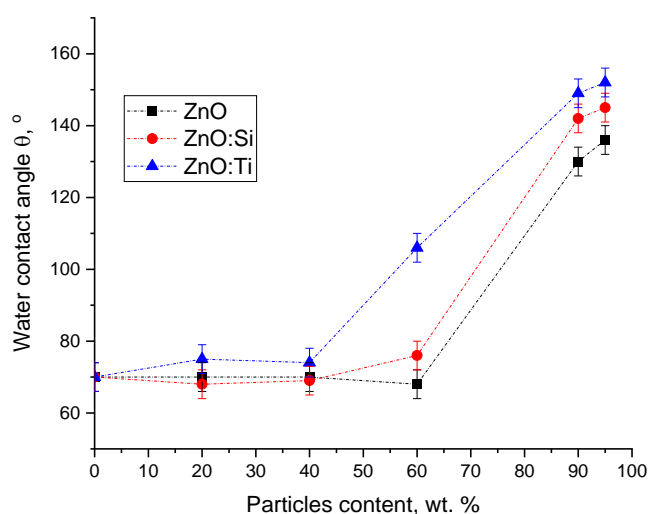


Figure 5.9 Wetting of particles-polymer thin layer coatings

Beyond the previously mentioned particle concentration threshold, a rapid increase in water contact angle (WCA) is observed, reaching maximum values of  $136^\circ$  for the ZnO–polymer system,  $143^\circ$  for ZnO:Si, and  $153^\circ$  for ZnO:Ti composites. This sharp rise in WCA can be attributed to the onset of polymer deficiency in the system—where the polymer matrix is only sufficient to partially coat the surface of the filler particles, primarily covering their outermost surfaces. At higher particle loadings, this limitation in binder availability leads to the development of a surface texture favorable for the Cassie–Baxter wetting regime, in which air pockets are trapped beneath water droplets, significantly enhancing surface hydrophobicity.

As illustrated schematically in Figure 5.10, at low pigment concentrations, the polymer film is abundant enough to completely coat the surfaces and the tops of all embedded particles, resulting in a smooth, continuous, and relatively flat surface (Figure 5.10a). In this configuration, no apparent wetting anomaly is present, and the surface exhibits typical polymer-like hydrophobic behavior.

However, as the particle concentration increases and the polymer becomes insufficient to fully envelop all surface features, the surface roughness begins to rise. This increase in roughness—defined as the ratio between the actual three-dimensional surface area and its two-dimensional projected area—creates conditions conducive to the transition into a composite wetting state (Figure 5.10b). Ultimately, at even higher filler content, the polymer is only sufficient to coat individual particles, without filling the interstitial voids between them (Figure 5.10c). In such a binder-deficient system, provided that the thin polymer coating still effectively covers the polar surface of the particles, the surface achieves maximum possible roughness while maintaining a non-polar outer layer—ideal for inducing strong hydrophobic or even superhydrophobic behavior.

It is also important to note that the native surface of the synthesized oxide particles is highly polar [101], in contrast to the relatively non-polar nature of the polymer binders used in the coating formulations. Consequently, if the polymer content is reduced beyond a critical threshold, its continuous film may rupture or thin to the point where patches of the polar oxide surface are exposed. This partial exposure results in localized

increases in surface energy, ultimately leading to a loss of hydrophobicity and a reversion to hydrophilic behavior in the affected regions.

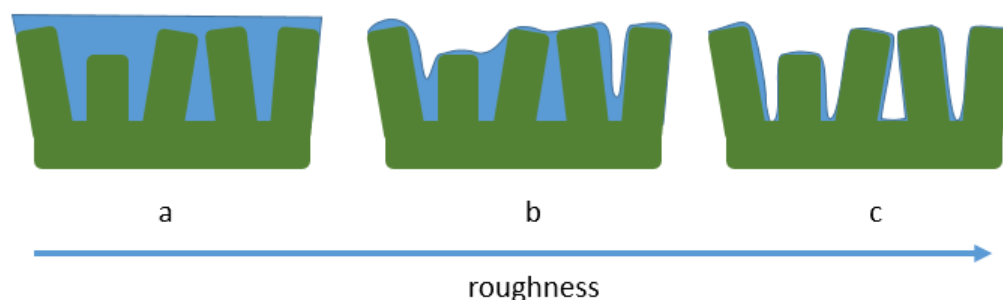


Figure 5.10 Schematic diagram of the composite surface with different particles-binder ratio

A water contact angle (WCA) of  $150^\circ$ , which qualifies as *superhydrophobic* according to standard definitions [102], was achieved exclusively in the ZnO:Ti composite system. This result is particularly noteworthy considering that the intrinsic WCA of the base polymer used is only  $70^\circ$ , which is significantly below the conventional hydrophobic threshold of  $90^\circ$ . The substantial enhancement in surface hydrophobicity suggests that further optimization is possible - particularly by replacing the current polymer matrix with a less polar alternative. Potential candidates include siloxane-based polymers, polyolefins, or fluorinated polymers, all of which exhibit inherently lower surface energies and could further elevate the WCA and enhance the stability of the Cassie–Baxter wetting regime.

Moreover, hydrophobization of particle surfaces is not strictly limited to polymer encapsulation. Non-polymeric surface modification strategies may also be employed to functionalize the particles and improve water repellency. For example, surface treatment using silane or fluorinated silane coupling agents can create a covalently bonded, low-energy outer layer on the particles [103]. Alternatively, more environmentally benign methods, such as functionalization with long-chain carboxylic acids or their esters, have demonstrated effectiveness in imparting hydrophobic character while maintaining ecological safety [104].

Conversely, employing highly polar polymeric or inorganic binders—such as polyvinyl alcohol (PVA), polyurethanes, or silica-based systems—can drive the wettability in the opposite direction, promoting strong hydrophilic behavior. This tunable wetting effect, controlled by the choice of binder and particle surface chemistry, offers valuable opportunities for designing functional surfaces tailored to specific applications.

Such versatility is particularly relevant in areas like microfluidics, anti-icing surfaces, self-cleaning coatings, and water-repellent barriers. Importantly, the ability to cast these functional coatings from polymer solutions provides a scalable and industrially viable approach to fabricating advanced wetting surfaces with tailored performance characteristics.

## 5.2 Wetting transition of particulate filled textured coatings

It is well established that coatings formulated with organic binders—such as butyl methacrylate—are susceptible to photodegradation when exposed to ultraviolet (UV) radiation. This degradation process leads to the breakdown of polymer chains and chemical structure alterations at the surface, which, in turn, result in a gradual transition toward increased hydrophilicity. As a consequence, the surface wetting behavior of the coating shifts over time, potentially compromising its original functionality, particularly in applications requiring long-term hydrophobic or superhydrophobic performance.

In realistic service environments, coatings are not only exposed to UV radiation but also to elevated humidity and water contact. The presence of moisture introduces an additional variable that can synergistically accelerate the degradation process. Water can facilitate hydrolysis of the polymer matrix and enhance the mobility of photogenerated reactive species, further promoting surface oxidation and the formation of hydrophilic groups.

As shown in Chapter 4, the synthesized texture-forming particles - such as ZnO and TiO<sub>2</sub> - exhibit measurable photoactivity under UV illumination. While this

property can be advantageous in photocatalytic applications, it raises concerns regarding the long-term stability of coatings in which these particles are embedded. Their intrinsic photoactivity may catalyze the degradation of the surrounding organic binder, leading to a more rapid deterioration of surface properties than would occur in particle-free systems.

Therefore, it becomes critically important to assess the stability of such composite coatings under prolonged exposure to oxidative stress conditions, particularly UV radiation, which is a dominant environmental factor influencing the aging of outdoor-exposed surfaces. Comprehensive durability testing under controlled UV and moisture exposure is essential for evaluating the practical applicability of these materials and for optimizing formulations to balance performance with longevity.

The hydrophilicity of a material is related to the hydroxyl group, and the formation of hydroxyl groups is related to the photocatalytic mechanism [105].

The photocatalytic principle is based on the excitation of a semiconductor by light (ultraviolet or visible light). Under the influence of photons, the catalyst (or semiconductor) can produce highly oxidising free radicals. These hydroxyl radicals can easily break down pollutants attached to the catalyst surface, and the pollutants can be broken down into  $H_2O$ ,  $CO_2$ , etc. The semiconductor ZnO converts photon energy into chemical energy through redox reactions, which excites the active sites of ZnO and degrades the molecules of the compound. The degradation process is initiated by a series of oxidation processes involving a strong oxidant ( $\cdot OH$ ).  $\cdot OH$  is produced by photolysis of water molecules adsorbed on the active sites of ZnO. Organic pollutants adsorbed on the catalyst are then degraded through a series of radical reactions. When ZnO is exposed to light at 380 nm or lower, valence band electrons will move to the CB. At the same time, holes will be generated, and the number of holes will be the same as the number of electrons that have jumped to the CB.

The band gap ( $E_g$ ) of a semiconductor is generally less than 3 eV. When the energy ( $h\nu$ ) of the incident light is greater than the band gap ( $E_g$ ) of the semiconductor, electrons and holes are generated in the semiconductor under the action of  $h\nu$ . The

holes react with water to generate hydroxyl radicals ( $\cdot\text{OH}$ ) and hydrogen ions, and the holes can also react with hydroxide ions to also generate hydroxyl radicals. The electrons can react with  $\text{O}_2$  to form  $\cdot\text{O}_2^-$ , which can also react with hydrogen ions to form  $\cdot\text{OOH}$  radicals, and finally  $\text{H}_2\text{O}_2$  is formed. The reaction of  $\text{H}_2\text{O}_2$  with  $\cdot\text{O}_2^-$  radicals also ultimately produces hydroxyl radicals ( $\cdot\text{OH}$ ).

The band gap of  $\text{TiO}_2$  is 3.2 eV, while that of  $\text{ZnO}$  is 3.23 eV. Their band gaps are similar, and the energy levels are staggered. The energy level difference between  $\text{ZnO}$  and  $\text{TiO}_2$  is used to effectively separate photo-generated electrons and holes, which prolongs the time it takes for them to recombine and improves the hydrophilicity of  $\text{ZnO-TiO}_2$ . After doping with  $\text{SiO}_2$ , there is no significant change in the band gap compared to  $\text{ZnO}$ , and the contact angle is also similar to that of  $\text{ZnO}$ .

Figure 5.11 presents the water contact angle (WCA) data for  $\text{ZnO}$ ,  $\text{ZnO-SiO}_2$ , and  $\text{ZnO-TiO}_2$  films following different durations of light exposure. The results clearly demonstrate that prolonged illumination significantly influences the wettability of the coating surfaces. After 240 minutes of continuous light exposure, the WCA of the  $\text{ZnO}$  film shows a moderate decrease but does not fall below the hydrophilicity threshold ( $\text{WCA} < 90^\circ$ ), indicating that the surface remains weakly hydrophobic. In contrast, the  $\text{ZnO-SiO}_2$  coating displays a more pronounced decrease in WCA, reaching  $81^\circ$ , thereby meeting the conventional criterion for a hydrophilic surface.

The most significant change is observed in the  $\text{ZnO-TiO}_2$  system. Initially exhibiting a superhydrophobic WCA of  $152.8^\circ$ , the surface transitions to a near-superhydrophilic state with a final contact angle of just  $32.7^\circ$  after UV irradiation. This drastic reduction signifies a substantial enhancement in surface hydrophilicity, suggesting a stronger photoinduced response in the  $\text{ZnO-TiO}_2$  composite compared to the other systems.

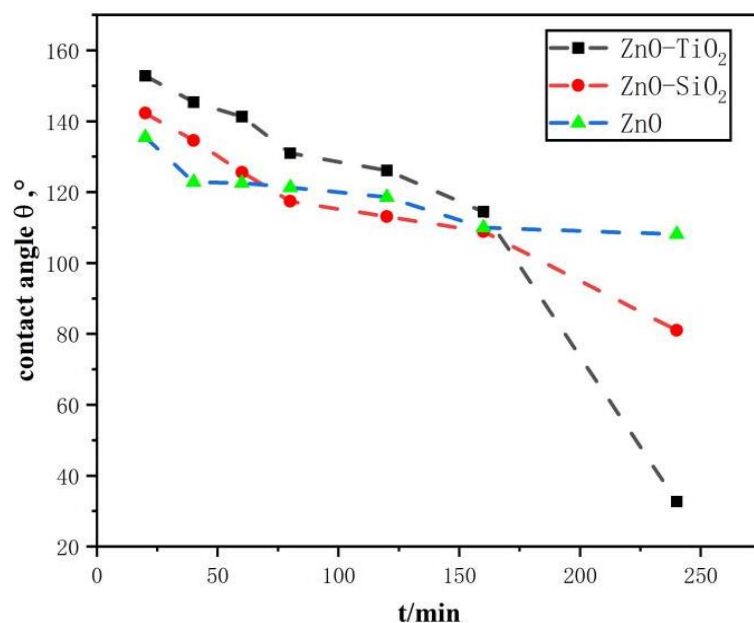


Figure 5.11 Wetting transition from superhydrophobic to hydrophilic state under the exposition to UV light

These transformations in surface wettability can be attributed to the generation of hydroxyl radicals ( $\cdot\text{OH}$ ) upon UV illumination. When exposed to ultraviolet light, the ZnO, ZnO-SiO<sub>2</sub>, and ZnO-TiO<sub>2</sub> films generate photogenerated electron-hole ( $e^-/h^+$ ) pairs. The photogenerated holes ( $h^+$ ) can interact with lattice oxygen, resulting in the formation of oxygen vacancies on the surface. These vacancies act as reactive adsorption sites for various species. While both oxygen and water molecules may adsorb at these sites, the kinetics favor the adsorption of hydroxyl radicals derived from water, especially under UV-induced oxidative conditions. The resulting  $\cdot\text{OH}$  groups enhance surface polarity and contribute to increased hydrophilicity.

Furthermore, the hierarchical micro/nanostructure of the film surfaces plays a critical role in amplifying the wetting behavior. The combination of surface chemistry changes (due to  $\cdot\text{OH}$  adsorption) and increased surface roughness—arising from the textured morphology—leads to the transition from hydrophobic or superhydrophobic states to hydrophilic or even superhydrophilic regimes.

It is also important to highlight that ultraviolet light, due to its short wavelength and high energy, possesses strong oxidative potential and molecular dissociation capability. It can ionize atmospheric oxygen, leading to the formation of reactive oxygen species such as atomic oxygen and ozone. These species further react to produce hydroxyl radicals, thereby accelerating the surface transition. The cumulative effect of UV-induced lattice activation, radical formation, and surface restructuring results in the rapid evolution of surface wettability, particularly in photoactive systems like ZnO–TiO<sub>2</sub>.

## Conclusions to Chapter 5

In this chapter, a series of organo-mineral nanocomposite coatings were successfully developed using styrene–butyl methacrylate as a polymeric matrix and four types of inorganic fillers: TiO<sub>2</sub>, SiO<sub>2</sub>, ZnO, and ZnO–SiO<sub>2</sub>. The synthesized ZnO and ZnO–SiO<sub>2</sub> nanoparticles, obtained via a simple one-step chemical precipitation method, demonstrated sufficient stability and functional integration within the polymer matrix. Morphological characterization revealed that TiO<sub>2</sub> and ZnO particles tend to form agglomerates due to their high surface energy, while SiO<sub>2</sub> and hybrid ZnO–SiO<sub>2</sub> particles exhibited better dispersion, contributing to distinct surface textures.

The wettability of the coatings was found to be strongly dependent on the type and concentration of the filler particles. For TiO<sub>2</sub> and SiO<sub>2</sub> systems, a pronounced increase in water contact angle (WCA) was observed at intermediate filler concentrations, indicating a transition toward superhydrophobicity. In contrast, ZnO-filled coatings showed minimal variation in WCA, suggesting limited influence on surface roughness and surface energy. The hybrid ZnO–SiO<sub>2</sub> system achieved the highest contact angle (152.5°), confirming its superior ability to induce

superhydrophobic behavior through combined effects of hierarchical surface structuring and reduced surface energy.

The experimental results confirmed that tuning the particle-to-polymer ratio plays a critical role in controlling surface wettability. Below 40–60 wt.% filler content, the coatings exhibited polymer-dominated smooth surfaces with limited hydrophobicity. Beyond this threshold, the onset of polymer deficiency led to the formation of a partially exposed particle-rich surface, promoting the Cassie–Baxter wetting regime. Notably, ZnO:TiO<sub>2</sub> coatings exhibited the highest WCA of 153°, highlighting the importance of surface composition and topography in optimizing water-repellent properties.

Photoinduced wettability changes under UV irradiation revealed the dynamic nature of the coatings. While ZnO and ZnO–SiO<sub>2</sub> coatings demonstrated moderate hydrophilic transitions, the ZnO–TiO<sub>2</sub> system underwent a complete transition from superhydrophobic to highly hydrophilic state (WCA reduced from 152.8° to 32.7°). This effect is attributed to the generation of hydroxyl radicals and surface oxidation driven by photocatalytic activity. These findings suggest that the long-term performance of such coatings must be carefully evaluated under environmental stressors, particularly UV exposure, and may be further improved through surface chemical modification or the use of more stable binder systems.

**The results of this chapter were published in:**

1. Че, Л.; Білоусова, А.; Миронюк, О. Establishing the type of texture forming particles on hydrophobic properties of coatings. Herald of Khmelnytskyi National University Technical Sciences 2024, 333 (2), 155–161. 10.31891/2307-5732-2024-333-2-25. ISSN 2307-5732
2. Myronyuk, O., Che, L., Bilousova, A., & Pitak, Y. (2024). Zinc Oxide Based Particles with Hierarchical Structure for Surface Wetting Modification (pp. 1–4). 10.1109/khpiweek61434.2024.10878067

3. Wang, M.; Li, C.; Liu, B.; Qin, W.; Xie, Y. Facile synthesis of Nano-Flower B-Bi<sub>2</sub>O<sub>3</sub>/TiO<sub>2</sub> heterojunction as photocatalyst for degradation RHB. *Molecules* 2023, 28 (2), 882. 10.3390/molecules28020882. ISSN 1420-3049

## CHAPTER 6. Thin organic coatings on mineral surfaces

In the broader context of hybrid organo-mineral surface engineering, the combination of inorganic micro- or nanoparticles with polymeric matrices enables the formation of functional coatings with tailored physicochemical properties. Such systems are typically designed to modulate surface energy, wetting behavior, or barrier performance. However, an alternative and complementary approach to surface modification involves the direct structuring of substrates through laser ablation. This method produces hierarchical micro- and nanoscale topographies that, when coupled with low-surface-energy modifiers, can emulate or even surpass the functionalities of particle–polymer coatings. Despite the difference in fabrication pathways, both approaches converge on the formation of organic–inorganic interfacial architectures with controlled wettability and surface functionality. In this section, we examine laser-textured aluminum surfaces subsequently modified with hydrophobizing agents, establishing their relevance within the same conceptual framework as the previously discussed composite coatings.

Textured surfaces are increasingly being used to control wetting processes or the contact between a solid and a liquid. The history of the development of such materials is based on the features of surfaces that can be found in nature. For example, superhydrophobicity is a characteristic property of lotus leaves [106], the body and limbs of some insect species [107], etc. The increased ability to self-clean is characteristic of the inner surface of the flytrap flower, which provides ultra-low rolling angles. This effect has been studied and used to create a number of SLIPS surfaces [108 and 109].

In addition to repelling liquids, texture also provides the opposite effect – complete adhesion. For example, superhydrophilic surfaces can be used to avoid fogging of glass, as water vapour does not form a lens of light-scattering droplets during condensation, but a continuous transparent water film. Developed affinity surfaces can also form a sufficiently strong mechanical contact, which allows geckos

with a small body weight to literally "run on the walls" and has become the basis for the research and development of similar materials [110].

The decisive factors that ensure either repulsion or contact of such surfaces with liquid or other surfaces are their affinity.

A well-known way to produce condensed water is to use air moisture. This method works even for desert regions of the planet where the required air humidity is achieved only at certain times of the day. The essence of the method is the presence of a certain surface - a condenser, often with a temperature below the ambient temperature, on which a captured layer of water is formed. In some studies, purely hydrophilic or hydrophobic surfaces or combinations of these are used as condenser materials [111]. In most studies, the materials being compared are heterogeneous and it is not possible to clearly establish the effect of the surface character on condensation processes. Therefore, in order to establish the effect of surface polarity on condensation processes, it is an urgent task to conduct such a study to compare condensation volumes using texturally identical surfaces with hydrophobic and hydrophilic properties.

The aim of this work is to determine the effect of hydrophobic metal surfaces on the processes of water collection from steam.

The tasks corresponding to the goal are to apply surface texture to samples by a method that allows obtaining highly regular repeatable patterns; to perform hydrophilic and hydrophobic treatment of identical surfaces; to determine the effect of surface treatment and orientation of anisotropic textures on water collection performance.

In this work, we used femtosecond laser-textured aluminium 7500 surfaces of 12.6x12.6 cm in size and 1 mm thick.

The surface texture was selected from the several variants with different characteristic values of the texture (Fig. 6.1, Table 6.1):

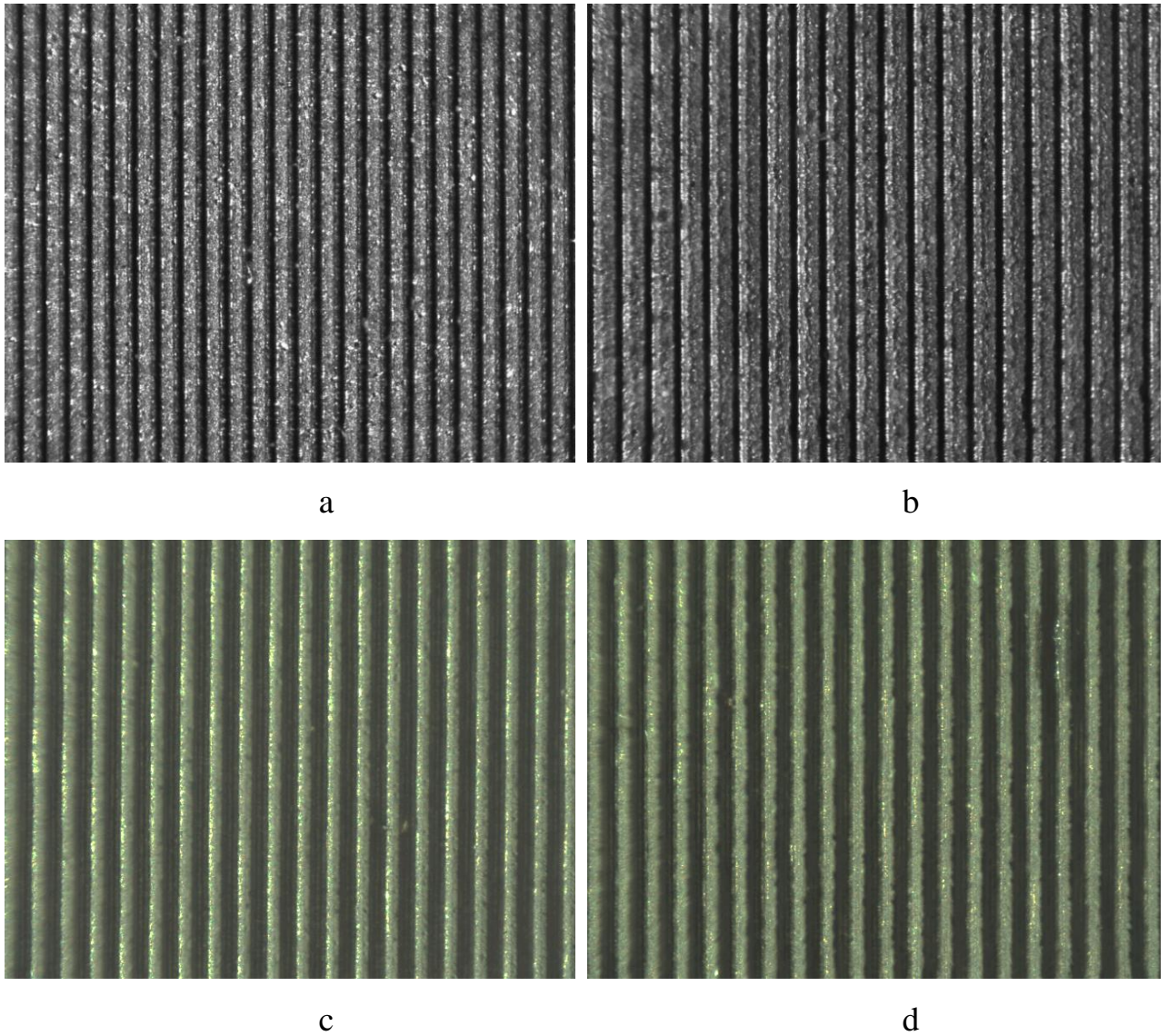


Figure 6.1 Surface morphology of aluminum 7500 alloy samples after laser texturing, observed at 100× magnification

The initial water contact angle measured on polished aluminum surfaces after exposure to ambient atmospheric conditions was found to be approximately  $78^\circ$ . This value indicates moderate hydrophobic behavior and reflects the influence of natural surface aging processes, including adsorption of airborne organic species. Notably, the freshly prepared, clean aluminum oxide surface is known to exhibit intrinsically hydrophilic properties, with a typical contact angle of around  $50^\circ$ , as reported in [112].

The discrepancy between the hydrophilic nature of the pristine oxide layer and the higher observed contact angle on aged surfaces can be attributed to the spontaneous accumulation of low-surface-energy contaminants from the environment. These

adsorbates alter the surface chemistry and reduce its affinity for water. Consequently, even when the underlying micro- or nano-scale topography exhibits fractal characteristics, the wetting behavior is governed predominantly by surface energy modifications rather than texture alone. This explains the relatively modest contact angle values observed on fractally textured aluminum oxide surfaces.

Table 6.1 – Aluminium surface texture parameters

| Texture    | Presence of LIPSS | Period, mkm | Trench width, mkm | Water contact angle, ° |
|------------|-------------------|-------------|-------------------|------------------------|
| Fig. 6.1 a | +                 | 45          | 20                | 126                    |
| Fig. 6.1 b | +                 | 57          | 20                | 130                    |
| Fig. 6.1 c | +                 | 60          | 45                | 148                    |
| Fig. 6.1 d | -                 | 60          | 45                | 159                    |

Femtosecond-laser-textured aluminum samples of the 7500 series, processed under both microstructuring and fractal-like nanostructuring regimes, exhibit a remarkable ability to undergo spontaneous hydrophobization. In the absence of any chemical modification, these laser-induced surface structures are capable of achieving a superhydrophobic state, with water contact angles reaching up to 159°. Notably, surfaces featuring only microscale textures (without the additional fractal nanostructure layer) demonstrated the most effective water-repellent performance. This observation may be attributed to a reduction in the coordination activity of aluminum as the thickness of the native oxide layer increases, thereby limiting interactions with polar water molecules.

In contrast, when surface hydrophobization is achieved through deliberate chemical modification, the presence of a hierarchical (micro/nano) surface structure becomes significantly more advantageous. Under such conditions, the use of

alkoxysilanes or fluorinated silane derivatives as hydrophobizing agents results in contact angles exceeding  $160^\circ$ , thereby establishing an enhanced superhydrophobic character. In these chemically treated systems, the fractal surface morphology outperforms purely microtextured structures by up to  $10^\circ$ , highlighting the synergistic role of hierarchical roughness and low surface energy chemistry in maximizing water repellency.

The sample 6.1 d, therefore, has shown the best water repellent performance and was used in further study of water collection.

Schematically the textures on sample's surfaces with uniaxially oriented profiles, which in cross-section had the shape of a trapezoid with the geometric parameters are shown in Fig. 6.2.

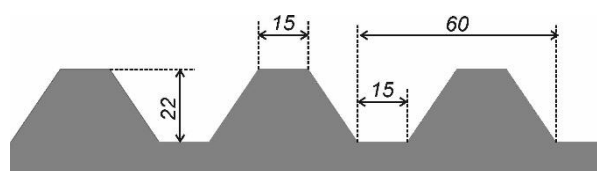


Figure 6.2 Anisotropic texture cross-section, sizes are noted in  $\mu\text{m}$ .

It is known that after laser ablation, the surface textures on metal substrates are initially hydrophilic, but over time they become hydrophobic due to the gradual adsorption of organic contaminants from the air, which leads to increased water repellency. This effect is reversible, as the organic layer can be removed both by treatment at high temperatures (up to  $400^\circ\text{C}$ ) and by UV irradiation, as shown in [113].

Along with spontaneous hydrophobisation, stearic acid was used as a surface modifier in this work. Samples of textured aluminium were placed in a muffle furnace at  $380^\circ\text{C}$  for 30 min, after which they were gradually cooled to room temperature. They were immersed in 100 ml of a 5 wt. % solution of stearic acid in isopropanol, removed from the solution and the residue was drained from the surface. After that, the samples were placed in an oven and dried at  $120^\circ\text{C}$ , then washed with isopropanol again and dried again. These samples are referred to as *t-St*.

To obtain samples that spontaneously hydrophobized (herein further noted as *SH*), the substrates were kept in a laboratory atmosphere for 2 months after texturing, which led to an increase in their hydrophobicity - reaching wetting angles above 150°. After the condensation tests, the samples were dried and placed in a 380°C oven for 30 minutes, after which they were gradually cooled to room temperature. Such samples (hereinafter referred to as hydrophilic samples) exhibited high hydrophilicity and, accordingly, were completely wetted with water, without the possibility of contact angle determination. Such samples are further noted as *Anneal*.

The determination of the condensation capacity of surfaces was carried out in a self-designed installation, which was a closed chamber with a volume of 18 litres, in which a sample was suspended, with a condensate receiver installed below it. The source of water mist was an ultrasonic mist generator Y09-010 (Sugold, China), which was used to maintain 100% humidity in the volume. Steam generation and condensation was carried out for 10-15 minutes, the time was measured to the nearest 1 second. The condensate was collected after running off the condensation plate into the collector vessel. Its weight was determined by the gravimetric method on an Axis 110S balance with an accuracy of 0.35 g per minute.

The geometry of the textured samples was determined by scanning electron microscopy using a MIRA3 TESCAN microscope in the secondary electron analysis mode. Since metal substrates were studied, no additional sputtering of the metal conductor layer was required.

Water contact angles were determined using the sessile drop technique with optical microscope Konus Accademy and goniometric set. Photos of the setting water droplet on the substrate were made in ScopePhoto application and contact angle value measured directly by the application tool. The femtosecond laser treatment of the aluminium surface produces a highly regular texture pattern in the form of grooves with a period of 60 µm. As can be seen from Fig. 6.3, the protrusions of the structure are encrusted with crystal-like formations, which may be the result of oxidation of a part of the material that was removed from the surface during processing. The bottom of the structure have a clearly distinguishable trace of the laser beam with periodically

located pinholes corresponding to the places of maximum energy concentration. It can be said that the texture obtained at the previous stages of LIPSS, due to a significant tendency to form aluminium oxide crystals as a result of oxidation of fresh portions of metal in contact with air, remains indistinguishable.

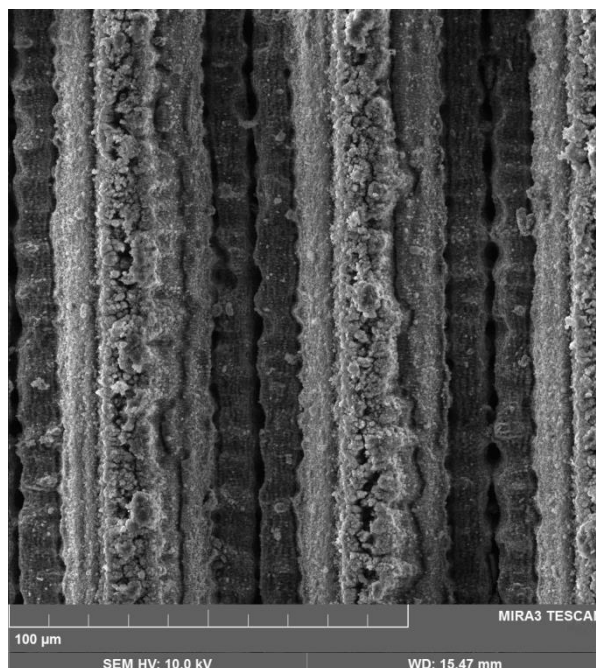


Figure 6.3. Surface texture of sample after laser ablation

The resulting aluminium surfaces have a combination of micro- and nanoscale texture levels, which gives them an increased ability to repel water after hydrophobisation, or, conversely, increased wettability with water in the case of fresh surfaces.

The type of hydrophobic agent determines the final values of the wetting angle, but for most functional modifiers, sufficiently high wetting angles are achievable, which do not increase significantly when switching, for example, from paraffin waxes to fluorinated paraffin waxes, which can be explained by the proximity of the contact angle of these materials and can be predicted using the classical Cassie equation. This is confirmed by the values of the contact angles of the samples treated with stearic acid, after spontaneous hydrophobisation and after annealing in a muffle furnace (Table 6.1).

Table 6.1 - Water wettability of surfaces

| Substrate treatment | Water contact angle of the textured surface, ° | Contact angle of the respective flat surface, ° |
|---------------------|--|---|
| <i>t-St</i>         | $154 \pm 3$                                    | $70 \pm 3$                                      |
| <i>SH</i>           | $148 \pm 3$                                    | $48 \pm 3$                                      |
| <i>Anneal</i>       | $10 \pm 3$                                     | $25 \pm 3$                                      |

On flat surfaces that have been treated with stearic acid or kept in a laboratory atmosphere without treatment, the state of hydrophobicity is not achieved, as their wetting angle is below 90°. However, the textured ones achieved a state of superhydrophobicity, for example, when treated with stearic acid. This can be explained, in addition to the increased specific surface value, by the much higher orientation of the hydrophobic agent molecules on substrates with nanoroughness.

The ability of the samples to act as condensation surfaces was characterised by the amount of liquid collected in the receiver at the same performance of the mist generator per unit time (Table 6.2). The values shown in the table represent the condensation capacity excluding the capacity of the sample mounting system and the receiver itself, which is 10,04 g/min.

Table 6.2 - Water vapour condensation capacity (g/min)

| Texture    | Treatment     | Condensation, g/min |
|------------|---------------|---------------------|
| vertical   | <i>t-St</i>   | 6,4                 |
| vertical   | <i>SH</i>     | 6,5                 |
| vertical   | <i>Anneal</i> | 8,2                 |
| horizontal | <i>t-St</i>   | 3,9                 |
| horizontal | <i>SH</i>     | 4,1                 |
| horizontal | <i>Anneal</i> | 5,4                 |
| none       | <i>t-St</i>   | 3,2                 |

|      |               |     |
|------|---------------|-----|
| none | <i>SH</i>     | 3,6 |
| none | <i>Anneal</i> | 3,9 |

All the samples studied show a pattern of increasing condensate flow with increasing surface hydrophilicity, which coincides with the results of [114]. Thus, the hydrophilic surface obtained after firing increases the efficiency of water collection by 28 % when the structure is vertically oriented and by 38 % when it is horizontally oriented. The stearic acid-treated and self-hydrophobised surfaces, which are relatively close in terms of contact angles, exhibit identical condensation performance within the measurement error.

Another significant factor is the presence of texture on the sample surface, which increases its activity compared to a flat surface. For anisotropic textures, such as the one used in this study, the orientation of the channels is an important factor: the vertical orientation increases liquid removal by 64 % compared to the horizontal orientation.

During the experiment, it was observed that at the beginning of condensate collection, surfaces with high hydrophobicity are wetted segmentally, and only after 10-15 minutes of exposure to the fog environment, a visually uniform wetting of the sample with water is achieved, which corresponds to the transition from the initial Cassie state to the stable Wenzel state.

The electric conductivity of the condensate, obtained in the experiment is 180  $\mu\text{S}/\text{cm}$ , that is close to the values of the rain and dew water. The condensation plates are, therefore, the perspective and low energy consuming way for the development of water deficiency problem solutions.

It has been shown that hydrophilisation of surfaces for water vapour condensation increases the water collection efficiency up to 38 % of the performance of hydrophobic surfaces.

The texture obtained during the femtosecond laser treatment is in the form of channels, the cross-section of which has the shape of a truncated trapezoid with an upper base of 15  $\mu\text{m}$ , a lower base of 45  $\mu\text{m}$  and a height of 22  $\mu\text{m}$ . It is shown that on the surface of this microtexture, an artefact structure is formed such as an inlay of

aluminium oxide crystals with primary dimensions of 30-60  $\mu\text{m}$ , which are formed as a result of metal oxidation during interaction with a high-temperature laser beam.

It has been demonstrated that after prolonged exposure of the textured surfaces, their hydrophobisation to sufficiently high levels of water repellency occurs spontaneously. The wetting angles reach  $148^\circ$ , which is close to the efficiency of chemical post-treatment with stearic acid - $154^\circ$ , respectively. When fired at  $380^\circ\text{C}$ , the hydrophobic layers of modifiers on the surfaces are destroyed, which leads to complete hydrophilisation of the textures.

It was shown that textured hydrophilised surfaces are the most effective for condensate collection. Compared to them, hydrophobisation reduces the process efficiency by up to 28%. The orientation of the microtexture is also an important factor. For the sample studied in this work, vertical orientation compared to horizontal orientation allowed to increase the condensate collection performance by 34 %.

In general, it has been shown that texturing and hydrophilisation of condensing surfaces is a promising way to increase the productivity of liquid water extraction from steam, which can be the basis for improving existing solutions and those that are being designed.

## Conclusions to Chapter 6

Laser texturing enables the formation of micro- and nanostructured aluminum surfaces that can exhibit either superhydrophobic or superhydrophilic properties depending on subsequent surface treatment. Spontaneous hydrophobization occurs over time due to environmental exposure, while stearic acid treatment enhances water repellency up to  $154^\circ$ , comparable to spontaneous effects ( $\sim 148^\circ$ ).

Surface polarity significantly affects water vapor condensation efficiency. Hydrophilic textures obtained via high-temperature annealing collect up to 38% more condensate than their hydrophobic counterparts, demonstrating the critical role of wettability in passive water harvesting applications.

The orientation of anisotropic textures strongly influences condensate removal. Vertically aligned channels enhance water collection by up to 64% compared to horizontally oriented ones, indicating that structural directionality must be considered in condenser design.

Textured hydrophilic surfaces outperform hydrophobic ones in condensate yield, despite lower contact angles. This highlights the importance of optimizing both surface chemistry and texture geometry to maximize efficiency in atmospheric water collection systems.

**The results of this chapter were published in:**

Myronyuk, O.; Li, C. Use of textured surfaces for condensation of water vapour and mist. *Water And Water Purification Technologies Scientific And Technical News* 2024, 37 (3), 50–56. 10.20535/2218-930032023301987. ISSN 2521-151X

## CONCLUSIONS

It has been established that the water-repellent performance of organo-mineral surfaces is largely governed by the structural characteristics of these coatings. Specifically, at a certain ratio between the matrix polymer and the texture-forming particles, a state is achieved in which the amount of organic matrix is minimally sufficient to form a continuous composite film. This structural configuration enables the development of composites with the most pronounced surface texture. The critical ratio between the organic and mineral components is determined by the size and shape of the filler particles. Moreover, when transitioning from microscale to nanoscale particles, a greater quantity of polymer matrix is required to achieve the same level of structural continuity.

It has been shown that in organo-mineral systems based on dispersed particles - using red mud as an example - the water-repellent properties are governed by a combination of key factors: the ability of the particles to form a textured coating surface, which in turn depends on the ratio between the particles and the polymer matrix; the surface inertness of the filler particles, with higher inertness leading to more stable water-repellent surfaces; and the particle size, as smaller particles contribute to higher contact angles and thus improved water-repellent performance.

Using an integrated approach based on hydrothermal synthesis, Zn-O-based particles with tunable morphology were obtained. By adjusting parameters such as temperature, catalyst type, reaction medium acidity, and the presence of doping agents (e.g., titanium dioxide and silicon dioxide), it is possible to control the particle size within a range of several tens to hundreds of nanometers, introduce hierarchical surface structures, and tailor the shape of the primary crystals, including plate-like, elongated, or irregular particles with complex architectures.

It has been shown that the use of hierarchical zinc oxide-based particles, particularly those doped with titanium dioxide, leads to a significant enhancement in water-repellent performance compared to undoped or structurally simple particles. The

observed increase in contact angle is approximately  $20^\circ$ , enabling the creation of truly superhydrophobic surfaces based on these hierarchical structures.

It has also been demonstrated that superhydrophobic surfaces can be achieved over a broader range of nanoparticle concentrations (20-60 wt. %) when the particles possess a hierarchical surface structure. Unlike those lacking a distinct dual-level hierarchy, such particles enable stable water repellency even as the filler concentration varies.

The studied materials with high specific surface area have shown strong potential for use in atmospheric water harvesting from fog. It was found that hydrophobic surfaces enable condensation of up to 7 grams of water per minute. In contrast, hydrophilic surfaces-achieved either by using unmodified mineral particles or by annealing-can collect up to 8.5 grams of atmospheric moisture per minute.

## References list

1. Zeng, Q., Zhou, H., Huang, J., & Guo, Z. (2021d). Review on the recent development of durable superhydrophobic materials for practical applications. *Nanoscale*, 13(27), 11734–11764. <https://doi.org/10.1039/d1nr01936h>
2. Barthlott, W., & Neinhuis, C. (1997b). Purity of the sacred lotus, or escape from contamination in biological surfaces. *Planta*, 202(1), 1–8. <https://doi.org/10.1007/s004250050096>
3. Neinhuis, C. (1997b). Characterization and distribution of water-repellent, self-cleaning plant surfaces. *Annals of Botany*, 79(6), 667–677. <https://doi.org/10.1006/anbo.1997.0400>
4. Samaha, M. A., Tafreshi, H. V., & Gad-El-Hak, M. (2011b). Superhydrophobic surfaces: From the lotus leaf to the submarine. *Comptes Rendus Mécanique*, 340(1–2), 18–34. <https://doi.org/10.1016/j.crme.2011.11.002>
5. Latthe, S., Terashima, C., Nakata, K., & Fujishima, A. (2014b). Superhydrophobic surfaces developed by mimicking hierarchical surface morphology of Lotus leaf. *Molecules*, 19(4), 4256–4283. <https://doi.org/10.3390/molecules19044256>
6. Barthlott, W., Mail, M., & Neinhuis, C. (2016). Superhydrophobic hierarchically structured surfaces in biology: evolution, structural principles and biomimetic applications. *Philosophical Transactions of the Royal Society a Mathematical Physical and Engineering Sciences*, 374(2073), 20160191. <https://doi.org/10.1098/rsta.2016.0191>
7. Drelich, J., Chibowski, E., Meng, D. D., & Terpilowski, K. (2011b). Hydrophilic and superhydrophilic surfaces and materials. *Soft Matter*, 7(21), 9804. <https://doi.org/10.1039/c1sm05849e>
8. Matin, A., Baig, U., Gondal, M., Akhtar, S., & Zubair, S. (2017). Facile fabrication of superhydrophobic/superoleophilic microporous membranes by spray-coating ytterbium oxide particles for efficient oil-water separation. *Journal*

- of Membrane Science, 548, 390–397.  
<https://doi.org/10.1016/j.memsci.2017.11.045>
9. Parvate, S., Dixit, P., & Chattopadhyay, S. (2020b). Superhydrophobic Surfaces: Insights from Theory and Experiment. *The Journal of Physical Chemistry B*, 124(8), 1323–1360. <https://doi.org/10.1021/acs.jpcc.9b08567>
  10. Liu, Y., Wu, M., Guo, C., Zhou, D., Wu, Y., Wu, Z., Lu, H., Zhang, H., & Zhang, Z. (2022). A review on preparation of superhydrophobic and superoleophobic surface by laser micromachining and its hybrid methods. *Crystals*, 13(1), 20. <https://doi.org/10.3390/cryst13010020>
  11. Bayer, I. (2017b). On the Durability and Wear Resistance of Transparent Superhydrophobic Coatings. *Coatings*, 7(1), 12. <https://doi.org/10.3390/coatings7010012>
  12. Li, G., Li, X., Wang, H., Yang, Z., Yao, J., & Ding, G. (2012). Fabrication and characterization of superhydrophobic surface by electroplating regular rough micro-structures of metal nickel. *Microelectronic Engineering*, 95, 130–134. <https://doi.org/10.1016/j.mee.2011.12.012>
  13. Wang, Y., Zhang, L., Wu, J., Hedhili, M. N., & Wang, P. (2015b). A facile strategy for the fabrication of a bioinspired hydrophilic–superhydrophobic patterned surface for highly efficient fog-harvesting. *Journal of Materials Chemistry A*, 3(37), 18963–18969. <https://doi.org/10.1039/c5ta04930j>
  14. Zahner, D., Abagat, J., Svec, F., Fréchet, J. M. J., & Levkin, P. A. (2011). A facile approach to Superhydrophilic–Superhydrophobic patterns in porous polymer films. *Advanced Materials*, 23(27), 3030–3034. <https://doi.org/10.1002/adma.201101203>
  15. Lian, Z., Zhou, J., Ren, W., Chen, F., Xu, J., Tian, Y., & Yu, H. (2023b). Recent progress in bio-inspired macrostructure array materials with special wettability—from surface engineering to functional applications. *International Journal of Extreme Manufacturing*, 6(1), 012008. <https://doi.org/10.1088/2631-7990/ad0471>

- 16.Ahmed, G., Tash, O. A., Cook, J., Trybala, A., & Starov, V. (2017). Biological applications of kinetics of wetting and spreading. *Advances in Colloid and Interface Science*, 249, 17–36. <https://doi.org/10.1016/j.cis.2017.08.004>
- 17.De Gennes, P. G. (1985b). Wetting: statics and dynamics. *Reviews of Modern Physics*, 57(3), 827–863. <https://doi.org/10.1103/revmodphys.57.827>
- 18.Ivanova, N., Obaeed, G. L. O., Sulkarnaev, F., Buchkina, N., Gubin, A., & Yurtaev, A. (2023b). Effect of biochar aging in agricultural soil on its wetting properties and surface structure. *Biochar*, 5(1). <https://doi.org/10.1007/s42773-023-00272-4>
- 19.Meyer-Veltrup, L., Brischke, C., Alfredsen, G., Humar, M., Flæte, P., Isaksson, T., Brelid, P. L., Westin, M., & Jermer, J. (2017b). The combined effect of wetting ability and durability on outdoor performance of wood: development and verification of a new prediction approach. *Wood Science and Technology*, 51(3), 615–637. <https://doi.org/10.1007/s00226-017-0893-x>
- 20.Ahmad, D., Van Den Boogaert, I., Miller, J., Presswell, R., & Jouhara, H. (2018). Hydrophilic and hydrophobic materials and their applications. *Energy Sources Part a Recovery Utilization and Environmental Effects*, 40(22), 2686–2725. <https://doi.org/10.1080/15567036.2018.1511642>
- 21.Tsibouklis, J., Graham, P., Eaton, P. J., Smith, J. R., Nevell, T. G., Smart, J. D., & Ewen, R. J. (2000b). Poly(perfluoroalkyl methacrylate) Film Structures: Surface Organization Phenomena, Surface Energy Determinations, and Force of Adhesion Measurements. *Macromolecules*, 33(22), 8460–8465. <https://doi.org/10.1021/ma0008185>
- 22.Chaudhuri, R. G., & Paria, S. (2009). Dynamic contact angles on PTFE surface by aqueous surfactant solution in the absence and presence of electrolytes. *Journal of Colloid and Interface Science*, 337(2), 555–562. <https://doi.org/10.1016/j.jcis.2009.05.033>
- 23.Yin, S., Wu, D., Yang, J., Lei, S., Kuang, T., & Zhu, B. (2011b). Fabrication and surface characterization of biomimic superhydrophobic copper surface by

- solution-immersion and self-assembly. *Applied Surface Science*, 257(20), 8481–8485. <https://doi.org/10.1016/j.apsusc.2011.04.137>
24. Bharathidasan, T., Kumar, S. V., Bobji, Chakradhar, R., & Basu, B. J. (2014). Effect of wettability and surface roughness on ice-adhesion strength of hydrophilic, hydrophobic and superhydrophobic surfaces. *Applied Surface Science*, 314, 241–250. <https://doi.org/10.1016/j.apsusc.2014.06.101>
  25. Young, T. (1805b). III. An essay on the cohesion of fluids. *Philosophical Transactions of the Royal Society of London*, 95, 65–87. <https://doi.org/10.1098/rstl.1805.0005>
  26. Nishino, T., Meguro, M., Nakamae, K., Matsushita, M., & Ueda, Y. (1999). The lowest surface free energy based on  $-CF_3$  alignment. *Langmuir*, 15(13), 4321–4323. <https://doi.org/10.1021/la981727s>
  27. Wenzel, R. N. (1936b). RESISTANCE OF SOLID SURFACES TO WETTING BY WATER. *Industrial & Engineering Chemistry*, 28(8), 988–994. <https://doi.org/10.1021/ie50320a024>
  28. Miwa, M., Nakajima, A., Fujishima, A., Hashimoto, K., & Watanabe, T. (2000). Effects of the surface roughness on sliding angles of water droplets on superhydrophobic surfaces. *Langmuir*, 16(13), 5754–5760. <https://doi.org/10.1021/la991660o>
  29. Cassie, A. B. D., & Baxter, S. (1944b). Wettability of porous surfaces. *Transactions of the Faraday Society*, 40, 546. <https://doi.org/10.1039/tf9444000546>
  30. Feng, L., Li, S., Li, Y., Li, H., Zhang, L., Zhai, J., Song, Y., Liu, B., Jiang, L., & Zhu, D. (2002). Super-Hydrophobic surfaces: from natural to artificial. *Advanced Materials*, 14(24), 1857–1860. <https://doi.org/10.1002/adma.200290020>
  31. Lan, L., Wang, H., Zhu, L., Di, Y., Kang, J., & Qiu, J. (2021b). Preparation and wetting mechanism of Laser-Etched composite Self-Assembled 1H,1H,2H,2H-Perfluorodecyltriethoxysilane superhydrophobic surface coating. *Physica Status Solidi (A)*, 219(3). <https://doi.org/10.1002/pssa.202100568>

- 32.Chen, X., Chen, Y., Jin, T., He, L., Zeng, Y., Ma, Q., & Li, N. (2018). Fabrication of superhydrophobic coating from non-fluorine siloxanes via a one-pot sol–gel method. *Journal of Materials Science*, 53(16), 11253–11264. <https://doi.org/10.1007/s10853-018-2348-7>
- 33.Zheng, H., Liu, L., Meng, F., Cui, Y., Li, Z., Oguzie, E. E., & Wang, F. (2021b). Multifunctional superhydrophobic coatings fabricated from basalt scales on a fluorocarbon coating base. *Journal of Material Science and Technology*, 84, 86–96. <https://doi.org/10.1016/j.jmst.2020.12.022>
- 34.Huang, X., Sun, M., Shi, X., Shao, J., Jin, M., Liu, W., Zhang, R., Huang, S., & Ye, Y. (2022b). Chemical vapor deposition of transparent superhydrophobic anti-Icing coatings with tailored polymer nanoarray architecture. *Chemical Engineering Journal*, 454, 139981. <https://doi.org/10.1016/j.cej.2022.139981>
- 35.Simpson, J. T., Hunter, S. R., & Aytug, T. (2015b). Superhydrophobic materials and coatings: a review. *Reports on Progress in Physics*, 78(8), 086501. <https://doi.org/10.1088/0034-4885/78/8/086501>
- 36.Hao, X., Cheng, Z., Zhang, Y., Xie, J., Zheng, H., Yue, C., & Sheng, W. (2024). Wettability study of an acidified Nano-TiO<sub>2</sub> superhydrophobic surface. *ACS Omega*, 9(4), 4447–4454. <https://doi.org/10.1021/acsomega.3c07011>
- 37.Mardosaitė, R., Jurkevičiūtė, A., & Račkauskas, S. (2021c). Superhydrophobic ZnO nanowires: Wettability mechanisms and functional Applications. *Crystal Growth & Design*, 21(8), 4765–4779. <https://doi.org/10.1021/acs.cgd.1c00449>
- 38.Xing, L., Xia, T., & Zhang, Q. (2022). Effect of hydrophobic Nano-SiO<sub>2</sub> particle concentration on wetting properties of superhydrophobic surfaces. *Nanomaterials*, 12(19), 3370. <https://doi.org/10.3390/nano12193370>
- 39.Sudha, P. N., Sangeetha, K., Vijayalakshmi, K., & Barhoum, A. (2018b). Nanomaterials history, classification, unique properties, production and market. In *Elsevier eBooks* (pp. 341–384). <https://doi.org/10.1016/b978-0-323-51254-1.00012-9>

40. Ajayan, P. M., Charlier, J., & Rinzler, A. G. (1999). Carbon nanotubes: From macromolecules to nanotechnology. *Proceedings of the National Academy of Sciences*, 96(25), 14199–14200. <https://doi.org/10.1073/pnas.96.25.14199>
41. Myint, M. T. Z., Kitsomboonloha, R., Baruah, S., & Dutta, J. (2010b). Superhydrophobic surfaces using selected zinc oxide microrod growth on ink-jetted patterns. *Journal of Colloid and Interface Science*, 354(2), 810–815. <https://doi.org/10.1016/j.jcis.2010.11.004>
42. Guo, M., Diao, P., & Cai, S. (2007). Highly hydrophilic and superhydrophobic ZnO nanorod array films. *Thin Solid Films*, 515(18), 7162–7166. <https://doi.org/10.1016/j.tsf.2007.03.038>
43. Theerthagiri, J., Salla, S., Senthil, R. A., Nithyadharseni, P., Madankumar, A., Arunachalam, P., Maiyalagan, T., & Kim, H. (2019b). A review on ZnO nanostructured materials: energy, environmental and biological applications. *Nanotechnology*, 30(39), 392001. <https://doi.org/10.1088/1361-6528/ab268a>
44. Li, X., Zhang, F., Ma, C., Deng, Y., Wang, Z., Elingarami, S., & He, N. (2012). Controllable Synthesis of ZnO with Various Morphologies by Hydrothermal Method. *Journal of Nanoscience and Nanotechnology*, 12(3), 2028–2036. <https://doi.org/10.1166/jnn.2012.5177>
45. Srećković, T., Bernik, S., Čeh, M., & Vojisavljević, K. (2008b). Microstructural characterization of mechanically activated ZnO powders. *Journal of Microscopy*, 232(3), 639–642. <https://doi.org/10.1111/j.1365-2818.2008.02131.x>
46. Gan, Y. X., Jayatissa, A. H., Yu, Z., Chen, X., & Li, M. (2020). Hydrothermal synthesis of nanomaterials. *Journal of Nanomaterials*, 2020, 1–3. <https://doi.org/10.1155/2020/8917013>
47. Baruah, S., & Dutta, J. (2009b). Hydrothermal growth of ZnO nanostructures. *Science and Technology of Advanced Materials*, 10(1), 013001. <https://doi.org/10.1088/1468-6996/10/1/013001>
48. Alfarisa, S., Toruan, P. L., Atina, Dwandaru, W. S. B., & Safitri, R. N. (2018). Morphological and structural studies of ZNO Micro-Nanorod structures

- synthesized using a Low-Cost hydrothermal method. *Makara Journal of Science*, 22(2). <https://doi.org/10.7454/mss.v22i2.8243>
49. Saleh, S. M., Soliman, A. M., Sharaf, M. A., Kale, V., & Gadgil, B. (2017b). Influence of solvent in the synthesis of nano-structured ZnO by hydrothermal method and their application in solar-still. *Journal of Environmental Chemical Engineering*, 5(1), 1219–1226. <https://doi.org/10.1016/j.jece.2017.02.004>
  50. Yu, Y., Hao, W., Du, Y., Wang, C., & Wang, T. (2009b). Growth mechanism for ZNO nanorod array in a metastable supersaturation solution. *Journal of Nanoscience and Nanotechnology*, 9(2), 909–913. <https://doi.org/10.1166/jnn.2009.c052>
  51. Yu, Y., Hao, W., Du, Y., Wang, C., & Wang, T. (2009c). Growth mechanism for ZNO nanorod array in a metastable supersaturation solution. *Journal of Nanoscience and Nanotechnology*, 9(2), 909–913. <https://doi.org/10.1166/jnn.2009.c052>
  52. Hayat, K., Gondal, M., Khaled, M. M., Ahmed, S., & Shemsi, A. M. (2010). Nano ZnO synthesis by modified sol gel method and its application in heterogeneous photocatalytic removal of phenol from water. *Applied Catalysis a General*, 393(1–2), 122–129. <https://doi.org/10.1016/j.apcata.2010.11.032>
  53. Yıldırım, Ö. A., & Durucan, C. (2010b). Synthesis of zinc oxide nanoparticles elaborated by microemulsion method. *Journal of Alloys and Compounds*, 506(2), 944–949. <https://doi.org/10.1016/j.jallcom.2010.07.125>
  54. Jimenez-Cadena, G., Comini, E., Ferroni, M., Vomiero, A., & Sberveglieri, G. (2010). Synthesis of different ZnO nanostructures by modified PVD process and potential use for dye-sensitized solar cells. *Materials Chemistry and Physics*, 124(1), 694–698. <https://doi.org/10.1016/j.matchemphys.2010.07.035>
  55. Purica, M., Budianu, E., Rusu, E., Danila, M., & Gavrila, R. (2002b). Optical and structural investigation of ZnO thin films prepared by chemical vapor deposition (CVD). *Thin Solid Films*, 403–404, 485–488. [https://doi.org/10.1016/s0040-6090\(01\)01544-9](https://doi.org/10.1016/s0040-6090(01)01544-9)

56. Ergin, B., Ketenci, E., & Atay, F. (2008). Characterization of ZnO films obtained by ultrasonic spray pyrolysis technique. *International Journal of Hydrogen Energy*, 34(12), 5249–5254. <https://doi.org/10.1016/j.ijhydene.2008.09.108>
57. Carcia, P. F., McLean, R. S., Reilly, M. H., & Nunes, G. (2003c). Transparent ZnO thin-film transistor fabricated by rf magnetron sputtering. *Applied Physics Letters*, 82(7), 1117–1119. <https://doi.org/10.1063/1.1553997>
58. Opel, M., Geprägs, S., Althammer, M., Brenninger, T., & Gross, R. (2013). Laser molecular beam epitaxy of ZnO thin films and heterostructures. *Journal of Physics D Applied Physics*, 47(3), 034002. <https://doi.org/10.1088/0022-3727/47/3/034002>
59. Lupan, O., Emelchenko, G., Ursaki, V., Chai, G., Redkin, A., Gruzintsev, A., Tiginyanu, I., Chow, L., Ono, L., Cuenya, B. R., Heinrich, H., & Yakimov, E. (2010b). Synthesis and characterization of ZnO nanowires for nanosensor applications. *Materials Research Bulletin*, 45(8), 1026–1032. <https://doi.org/10.1016/j.materresbull.2010.03.027>
60. Wang, R., Hashimoto, K., Fujishima, A., Chikuni, M., Kojima, E., Kitamura, A., Shimohigoshi, M., & Watanabe, T. (1997). Light-induced amphiphilic surfaces. *Nature*, 388(6641), 431–432. <https://doi.org/10.1038/41233>
61. Chen, X., Gao, J., Song, B., Smet, M., & Zhang, X. (2009b). Stimuli-Responsive wettability of nonplanar substrates: PH-Controlled floatation and supporting force. *Langmuir*, 26(1), 104–108. <https://doi.org/10.1021/la902137b>
62. Sun, T., Wang, G., Feng, L., Liu, B., Ma, Y., Jiang, L., & Zhu, D. (2003). Reversible Switching between Superhydrophilicity and Superhydrophobicity. *Angewandte Chemie International Edition*, 43(3), 357–360. <https://doi.org/10.1002/anie.200352565>
63. Feng, X., Feng, L., Jin, M., Zhai, J., Jiang, L., & Zhu, D. (2003b). Reversible super-hydrophobicity to super-hydrophilicity transition of aligned ZNO nanorod films. *Journal of the American Chemical Society*, 126(1), 62–63. <https://doi.org/10.1021/ja038636o>

64. Myronyuk, O. V., Prydatko, A. V., & Raks, V. A. (2016). Large-Scale solution for superhydrophobic surfaces. In Springer proceedings in physics (pp. 247–259). [https://doi.org/10.1007/978-3-319-30737-4\\_21](https://doi.org/10.1007/978-3-319-30737-4_21)
65. Myronyuk, O., Dudko, V., Baklan, D., & Melnyk, L. (2017b). Study of structure influence on wear resistance of hierarchial superhydrophobic coatings. *Eastern-European Journal of Enterprise Technologies*, 3(12 (87)), 44–49. <https://doi.org/10.15587/1729-4061.2017.103028>
66. Myronyuk, O., Baklan, D., Yong, Z., & Rodin, A. M. (2022b). Complex destruction of textured water-repellent coatings under the influence of UV and water flow. *Materials Today Communications*, 33, 104509. <https://doi.org/10.1016/j.mtcomm.2022.104509>
67. Xu, Y., Jin, J., Li, X., Han, Y., Meng, H., Wang, T., & Zhang, X. (2015b). Simple synthesis of ZnO nanoflowers and its photocatalytic performances toward the photodegradation of metamitron. *Materials Research Bulletin*, 76, 235–239. <https://doi.org/10.1016/j.materresbull.2015.11.062>
68. Erbil, H. Y. (2020). Practical Applications of superhydrophobic Materials and Coatings: Problems and Perspectives. *Langmuir*, 36(10), 2493–2509. <https://doi.org/10.1021/acs.langmuir.9b03908>
69. Sviderskii, V. A., Strashnenko, S. V., & Chernyak, L. P. (2007b). Ceramics from mining by-products and alumina production wastes. *Glass and Ceramics*, 64(1–2), 51–54. <https://doi.org/10.1007/s10717-007-0012-9>
70. Melnyk, L., Myronyuk, O., Ratushnyi, V., & Baklan, D. (2020). The feasibility of using red mud in coatings based on glyptal resins. *French-Ukrainian Journal of Chemistry*, 8(1), 88–94. <https://doi.org/10.17721/fujcv8i1p88-94>
71. Mardosaitė, R., Jurkevičiūtė, A., & Račkauskas, S. (2021d). Superhydrophobic ZNO nanowires: Wettability mechanisms and functional Applications. *Crystal Growth & Design*, 21(8), 4765–4779. <https://doi.org/10.1021/acs.cgd.1c00449>
72. Babisk, M. P., Amaral, L. F., Da Silva Ribeiro, L., Vieira, C. M. F., Prado, U. S. D., Gadioli, M. C. B., Oliveira, M. S., Da Luz, F. S., Monteiro, S. N., & Da Costa Garcia Filho, F. (2019). Evaluation and application of sintered red mud and its

- incorporated clay ceramics as materials for building construction. *Journal of Materials Research and Technology*, 9(2), 2186–2195. <https://doi.org/10.1016/j.jmrt.2019.12.049>
73. Myronyuk, O., Baklan, D., Yong, Z., & Rodin, A. M. (2022c). Complex destruction of textured water-repellent coatings under the influence of UV and water flow. *Materials Today Communications*, 33, 104509. <https://doi.org/10.1016/j.mtcomm.2022.104509>
74. Salazar-Hernández, C., Salazar-Hernández, M., Mendoza-Miranda, J. M., Miranda-Avilés, R., Elorza-Rodríguez, E., Carrera-Rodríguez, R., & Puy-Alquiza, M. J. (2018). Organic modified silica obtained from DBTL polycondensation catalyst for anticorrosive coating. *Journal of Sol-Gel Science and Technology*, 87(2), 299–309. <https://doi.org/10.1007/s10971-018-4732-9>
75. Zhang, B., Zeng, Y., Wang, J., Sun, Y., Zhang, J., & Li, Y. (2020b). Superamphiphobic aluminum alloy with low sliding angles and acid-alkali liquids repellency. *Materials & Design*, 188, 108479. <https://doi.org/10.1016/j.matdes.2020.108479>
76. Hu, J., He, S., Wang, Z., Zhu, J., Wei, L., & Chen, Z. (2018). Stearic acid-coated superhydrophobic Fe<sub>2</sub>O<sub>3</sub>/Fe<sub>3</sub>O<sub>4</sub> composite film on N80 steel for corrosion protection. *Surface and Coatings Technology*, 359, 47–54. <https://doi.org/10.1016/j.surfcoat.2018.12.040>
77. Myronyuk, O., Baklan, D., & Nudchenko, L. (2020b). Evaluation of the surface energy of dispersed aluminium oxide using owens-wendt theory. *Technology Audit and Production Reserves*, 2(1(52)), 25–27. <https://doi.org/10.15587/2312-8372.2020.200756>
78. Zhang, D., Chen, H., Xia, J., Nie, Z., Zhang, R., & Pakostova, E. (2022). Efficient dealkalization of red mud and recovery of valuable metals by a sulfur-oxidizing bacterium. *Frontiers in Microbiology*, 13. <https://doi.org/10.3389/fmicb.2022.973568>
79. Alkan, G., Schier, C., Gronen, L., Stopic, S., & Friedrich, B. (2017b). A Mineralogical Assessment on Residues after Acidic Leaching of Bauxite

- Residue (Red Mud) for Titanium Recovery. *Metals*, 7(11), 458.  
<https://doi.org/10.3390/met7110458>
80. Król, P., & Król, B. (2005). Determination of free surface energy values for ceramic materials and polyurethane surface-modifying aqueous emulsions. *Journal of the European Ceramic Society*, 26(12), 2241–2248.  
<https://doi.org/10.1016/j.jeurceramsoc.2005.04.011>
  81. Nath, H., & Sahoo, A. (2014b). A STUDY ON THE CHARACTERIZATION OF RED MUD. *International Journal on Applied Bio-Engineering*, 8(1), 1–4.  
<https://doi.org/10.18000/ijabeg.10118>
  82. Zhu, J., Liu, B., Li, L., Zeng, Z., Zhao, W., Wang, G., & Guan, X. (2016). Simple and green fabrication of a superhydrophobic surface by One-Step immersion for continuous Oil/Water separation. *The Journal of Physical Chemistry A*, 120(28), 5617–5623. <https://doi.org/10.1021/acs.jpca.6b06146>
  83. Kazak, O., Eker, Y. R., Akin, I., Bingol, H., & Tor, A. (2017b). Green preparation of a novel red mud@carbon composite and its application for adsorption of 2,4-dichlorophenoxyacetic acid from aqueous solution. *Environmental Science and Pollution Research*, 24(29), 23057–23068.  
<https://doi.org/10.1007/s11356-017-9937-x>
  84. Baranov, O. V., Komarova, L. G., & Golubkov, S. S. (2020). Hydrophobic coatings based on triethoxy(octyl)silane. *Russian Chemical Bulletin*, 69(6), 1165–1168. <https://doi.org/10.1007/s11172-020-2884-6>
  85. Semeshko, O., Pasichnyk, M., Hyrlya, L., Vasylenko, V., & Kucher, E. (2019b). Studying the influence of uv adsorbers on optical characteristics of light-protective polymer films for textile materials. *Eastern-European Journal of Enterprise Technologies*, 3(6 (99)), 14–21. <https://doi.org/10.15587/1729-4061.2019.167956>
  86. Pal, U., & Santiago, P. (2005). Controlling the morphology of ZNO nanostructures in a Low-Temperature hydrothermal process. *The Journal of Physical Chemistry B*, 109(32), 15317–15321.  
<https://doi.org/10.1021/jp052496i>

- 87.Moezzi, A., Cortie, M., & McDonagh, A. (2011b). Aqueous pathways for the formation of zinc oxide nanoparticles. *Dalton Transactions*, 40(18), 4871. <https://doi.org/10.1039/c0dt01748e>
- 88.Ahmed, N., Majid, A., Khan, M., Rashid, M., Umar, Z., & Baig, M. (2018). Synthesis and characterization of Zn/ZnO microspheres on indented sites of silicon substrate. *Materials Science-Poland*, 36(3), 501–508. <https://doi.org/10.2478/msp-2018-0058>
- 89.Umar, A., Chauhan, Chauhan, S., Kumar, R., Kumar, G., Al-Sayari, S., Hwang, S., & Al-Hajry, A. (2011b). Large-scale synthesis of ZnO balls made of fluffy thin nanosheets by simple solution process: Structural, optical and photocatalytic properties. *Journal of Colloid and Interface Science*, 363(2), 521–528. <https://doi.org/10.1016/j.jcis.2011.07.058>
- 90.Zubair, N., & Akhtar, K. (2020). Morphology controlled synthesis of ZnO nanoparticles for in-vitro evaluation of antibacterial activity. *Transactions of Nonferrous Metals Society of China*, 30(6), 1605–1614. [https://doi.org/10.1016/s1003-6326\(20\)65323-7](https://doi.org/10.1016/s1003-6326(20)65323-7)
- 91.Jiang, L., Li, G., Ji, Q., & Peng, H. (2006b). Morphological control of flower-like ZnO nanostructures. *Materials Letters*, 61(10), 1964–1967. <https://doi.org/10.1016/j.matlet.2006.07.167>
- 92.Ali, E. a. G. E., Matori, K. A., Saion, E., Aziz, S. H. A., Zaid, M. H. M., & Alibe, I. M. (2018). Calcination effect to the physical and optical properties of Zn<sub>2</sub>SiO<sub>4</sub> composite prepared by impregnation of ZnO on SiO<sub>2</sub> amorphous nanoparticles. *IOP Conference Series Materials Science and Engineering*, 440, 012036. <https://doi.org/10.1088/1757-899x/440/1/012036>
- 93.Musić, S., Filipović-Vinceković, N., & Sekovanić, L. (2011b). Precipitation of amorphous SiO<sub>2</sub> particles and their properties. *Brazilian Journal of Chemical Engineering*, 28(1), 89–94. <https://doi.org/10.1590/s0104-66322011000100011>
- 94.Chen, Y., Ding, H., & Sun, S. (2017). Preparation and characterization of ZNO nanoparticles supported on amorphous SIO<sub>2</sub>. *Nanomaterials*, 7(8), 217. <https://doi.org/10.3390/nano7080217>

95. Liqiang, J., Yichun, Q., Baiqi, W., Shudan, L., Baojiang, J., Libin, Y., Wei, F., Honggang, F., & Jiazhong, S. (2006b). Review of photoluminescence performance of nano-sized semiconductor materials and its relationships with photocatalytic activity. *Solar Energy Materials and Solar Cells*, 90(12), 1773–1787. <https://doi.org/10.1016/j.solmat.2005.11.007>
96. Bandi, V. R., Raghavan, C. M., Grandhe, B. K., Kim, S. S., Jang, K., Shin, D., Yi, S., & Jeong, J. (2013). Synthesis, structural and optical properties of pure and rare-earth ion doped TiO<sub>2</sub> nanowire arrays by a facile hydrothermal technique. *Thin Solid Films*, 547, 207–211. <https://doi.org/10.1016/j.tsf.2013.03.039>
97. Darmanin, T., & Guittard, F. (2014b). Recent advances in the potential applications of bioinspired superhydrophobic materials. *Journal of Materials Chemistry A*, 2(39), 16319–16359. <https://doi.org/10.1039/c4ta02071e>
98. Eita, M., Wågberg, L., & Muhammed, M. (2012). Spin-Assisted Multilayers of Poly(methyl methacrylate) and Zinc Oxide Quantum Dots for Ultraviolet-Blocking Applications. *ACS Applied Materials & Interfaces*, 4(6), 2920–2925. <https://doi.org/10.1021/am300243u>
99. Srivastava, V., Gusain, D., & Sharma, Y. C. (2013b). Synthesis, characterization and application of zinc oxide nanoparticles (n-ZnO). *Ceramics International*, 39(8), 9803–9808. <https://doi.org/10.1016/j.ceramint.2013.04.110>
100. Zhang, L., Somasundaran, P., Singh, S. K., Felse, A. P., & Gross, R. (2004). Synthesis and interfacial properties of sophorolipid derivatives. *Colloids and Surfaces a Physicochemical and Engineering Aspects*, 240(1–3), 75–82. <https://doi.org/10.1016/j.colsurfa.2004.02.016>
101. Rodwihok, C., Charoensri, K., Wongratanaphisan, D., Choi, W. M., Hur, S. H., Park, H. J., & Chung, J. S. (2020b). Improved photocatalytic activity of surface charge functionalized ZnO nanoparticles using aniline. *Journal of Material Science and Technology*, 76, 1–10. <https://doi.org/10.1016/j.jmst.2020.09.041>

102. Chu, H., Liu, Z., Ji, T., Yang, C., & Xu, N. (2024). Recent advances in the preparation of superhydrophobic coatings based on low-surface-energy modifiers: Diversified properties and potential applications. *Applied Thermal Engineering*, 251, 123591. <https://doi.org/10.1016/j.applthermaleng.2024.123591>
103. Wei, J., Nian, P., Wang, Y., Wang, X., Wang, Y., Xu, N., & Wei, Y. (2022b). Preparation of superhydrophobic-superoleophilic ZnO nanoflower@SiC composite ceramic membranes for water-in-oil emulsion separation. *Separation and Purification Technology*, 292, 121002. <https://doi.org/10.1016/j.seppur.2022.121002>
104. Sahasrabudhe, G., DeIuliis, G., & Galvin, K. (2021). Hydrophobization of minerals by sorbitan mono oleate (Span® 80): Selectivity of a novel agglomeration process. *Colloids and Surfaces a Physicochemical and Engineering Aspects*, 630, 127460. <https://doi.org/10.1016/j.colsurfa.2021.127460>
105. Schneider, J., Matsuoka, M., Takeuchi, M., Zhang, J., Horiuchi, Y., Anpo, M., & Bahnemann, D. W. (2014b). Understanding TiO<sub>2</sub> Photocatalysis: Mechanisms and materials. *Chemical Reviews*, 114(19), 9919–9986. <https://doi.org/10.1021/cr5001892>
106. Li, Z., Long, Z., Bai, H., Cheng, M., Zhao, T., Wang, X., Tian, Y., & Cao, M. (2024). Adjusting droplet adhesion of superhydrophobic coating via surface embedding of microparticles with mixed shapes. *Chemical Engineering Journal*, 492, 152227. <https://doi.org/10.1016/j.cej.2024.152227>
107. Wang, X., Wei, H., Luo, N., Luo, H., Zhou, X., Qin, B., Mei, Y., & Zhang, Y. (2024b). Smart materials and Micro/Nano architectonics for water harvesting: From fundamental mechanism to advanced application. *Composites Part a Applied Science and Manufacturing*, 184, 108241. <https://doi.org/10.1016/j.compositesa.2024.108241>
108. Ma, L., Zhang, Z., Gao, L., Liu, Y., & Hu, H. (2020). An exploratory study on using Slippery-Liquid-Infused-Porous-Surface (SLIPS) for wind turbine

- icing mitigation. *Renewable Energy*, 162, 2344–2360.  
<https://doi.org/10.1016/j.renene.2020.10.013>
109. Villegas, M., Zhang, Y., Jarad, N. A., Soleymani, L., & Didar, T. F. (2019b). Liquid-Infused Surfaces: A review of theory, design, and applications. *ACS Nano*, 13(8), 8517–8536. <https://doi.org/10.1021/acsnano.9b04129>
  110. Russell, A. P., Stark, A. Y., & Higham, T. E. (2019). The Integrative Biology of Gecko Adhesion: Historical review, current understanding, and Grand Challenges. *Integrative and Comparative Biology*, 59(1), 101–116. <https://doi.org/10.1093/icb/icz032>
  111. LaPotin, A., Kim, H., Rao, S. R., & Wang, E. N. (2019b). Adsorption-Based Atmospheric Water Harvesting: Impact of material and component properties on System-Level performance. *Accounts of Chemical Research*, 52(6), 1588–1597. <https://doi.org/10.1021/acs.accounts.9b00062>
  112. Wang, Y., Liu, X. W., Zhang, H. F., & Zhou, Z. P. (2015). Fabrication of self-healing super-hydrophobic surfaces on aluminium alloy substrates. *AIP Advances*, 5(4). <https://doi.org/10.1063/1.4905741>
  113. Myronyuk, O., Baklan, D., & Rodin, A. M. (2023b). UV resistance of Super-Hydrophobic stainless steel surfaces textured by femtosecond laser pulses. *Photonics*, 10(9), 1005. <https://doi.org/10.3390/photonics10091005>
  114. Pinheiro, R. A., Silva, A. A., Trava-Airoldi, V. J., & Corat, E. J. (2018b). Water vapor condensation and collection by super-hydrophilic and super-hydrophobic VACNTs. *Diamond and Related Materials*, 87, 43–49. <https://doi.org/10.1016/j.diamond.2018.05.009>